DEVELOPMENT OF A DISPLACEMENT SENSOR TOWARDS DETECTING

QUANTUM FLUCTUATIONS IN NANOELECTROMECHANICAL SYSTEMS

by

ANIL GÜNAY

Submitted to the Graduate School of Engineering and Natural Sciences

in partial fulfillment of

the requirements for the degree of

Master of Science

Sabancı University

Spring 2008

DEVELOPMENT OF A DISPLACEMENT SENSOR TOWARDS DETECTING

QUANTUM FLUCTUATIONS IN NANOELECTROMECHANICAL SYSTEMS

APPROVED BY:

Assoc. Prof. Dr. İsmet İ. Kaya   ………………………….

(Dissertation Supervisor)

Prof. Dr. Cihan Saçlıoğlu   ………………………….

Prof. Dr. Ahmet Oral   ………………………….

Assoc. Prof. Dr. Zafer Gedik   ………………………….

Assoc. Prof. Dr. Cem Öztürk   ………………………….

DATE OF APPROVAL: ………………………….

DEVELOPMENT OF A DISPLACEMENT SENSOR TOWARDS DETECTING QUANTUM FLUCTUATIONS IN NANOELECTROMECHANICAL SYSTEMS

Anıl Günay

FENS M.Sc. Thesis, 2008

Thesis Supervisor: Assoc. Prof. Dr. İsmet İ. Kaya

ABSTRACT

In condensed matter physics, it has been a long-standing goal to detect quantum mechanical behavior in macroscopic systems. Theoretically, a macroscopic system reveals its quantum dynamics when the mechanical quanta ($\hbar\omega$) are not obscured by thermal fluctuations ($k_B T$). The mechanical quanta will be observable if a mechanical resonator vibrates at GHz frequencies while kept at sub-Kelvin temperatures. Such a resonator's displacement fluctuations will be approximately a few femto-meters. Therefore, an ultra-sensitive and ultra-fast displacement sensor is desired to monitor the resonator's motion. Several research groups have been working at the edge of nanotechnology to develop such a high-performance resonator-sensor system. Despite the great effort, it has not been experimentally realized yet. In this thesis, we propose a new experimental methodology that has a major potential to approach the quantum limit. The method comprises of fabrication of a high frequency resonator with a built-in tunneling junction. Theoretical analyses reveal the clear advantage of a tunneling sensor over the presently applied capacitance based sensors. However, apparent complexities have detained their application to this problem. Here, we have developed and tested a new fabrication method that can overcome the major obstacles leading to application of this measurement scheme.

NANOELEKTROMEKANİK SİSTEMLERDE KUANTUM DALGALANMALARINI ÖLÇMEYE YÖNELİK BİR YER DEĞİŞTİRME ALGILAYICISININ GELİŞTİRİLMESİ

Anıl Günay

MDBF Yüksek Lisans Tezi, 2008

Tez Danışmanı: Doç. Dr. İsmet İ. Kaya

Anahtar Kelimeler: Kuantum Ölçümü, Nanofabrikasyon, Nanoelektromekanik Sistemler, Tünelleme, Yer değiştirme Algılayıcısı, Vakum Tünelleme Eklemi

ÖZET

Deneysel yoğun madde fiziğinde son yıllarda dikkatle izlenen konulardan birisi de makroskopik sistemlerde kuantum mekaniksel davranışlar gözlemlemeye yönelik yapılan araştırmalardır. Makroskopik bir sistemin mekanik kuantumu ($\hbar\omega$), ısıl titreşimlerden ($k_B T$) daha büyük olduğu zaman, sistemin kuantum özelliklerini gözlemlemek kuramsal olarak mümkünken deneysel olarak hala gösterilememiştir. Kuramsal olarak, yüksek frekans (GHz) ve düşük sıcaklık (<1 K) koşulları sağlandığında, bir rezonatörün mekanik kuantumu ölçülebilir. Bu koşullarda rezonatörün yer değiştirme miktarı femto-metre mertebesinde olacaktır. Dolayısıyla bu hareketi gözlemlemek için son derece hassas ve hızlı bir yer değiştirme algılayıcısına ihtiyaç duyulacaktır. Dünyada pekçok araştırma grubu, üstün performanslı rezonatör-algılayıcı sistemleri geliştirerek kuantum limitinde ölçüm hassasiyetine erişebilmek için nanoteknolojinin sınırlarında çalışmalarını sürdürmektedir. Bu tezde, istenilen ölçüm hassasiyetine ulaşma potansiyeli yüksek yeni bir deneysel metot önerilmektedir. Önerilen metot, yüksek frekanslı mekanik bir rezonatör ile ona entegre edilmiş bir tünelleme ekleminden oluşmaktadır. Tünelleme algılayıcısının, halen uygulanan kapasitif algılayıcılara olan üstünlüğü kuramsal analizler sonucu ortaya konmuş olsa da, gerçeklenmesindeki teknik karmaşıklar yüzünden geri planda kalmış ve deneysel olarak uygulanamamıştır. Bu projede, belirtilen deneyin uygulanabilmesi için yeni bir üretim metodu ve ölçüm düzeneği önerilmektedir.

ACKNOWLEDGEMENTS

First and foremost, I would like to thank my advisor, Dr. İsmet İ. Kaya, for his constant support, encouragement and guidance throughout this work. I am much indebted to him for his valuable academic and personal advices that he shared with me generously.

I am also grateful to Münir Dede and Dr. Ahmet Oral for their technical support during the fabrication of devices in Bilkent University Advanced Research Laboratory's clean room.

I want to express my gratitude to Utku Kemiktarak and Dr. Kamil Ekinci for their hospitality during my stay at Boston University. I also want to acknowledge that this research visit was supported by I2CAM.

My special thanks go to my parents Fethi and Safiye Günay, and my little sister Ezgi Günay for always being there for me. I have always felt their love and faith in me.

Finally, I would like to thank Ahmet Şamil Demirkol for his persistent love, support and confidence.

TABLE OF CONTENTS

LIST OF FIGURES

CHAPTER 1

INTRODUCTION

1.1 Context and Motivation

Tiny objects in nature like electrons behave according to the rules of quantum mechanics and obey the quantum principles such as the uncertainty principle. On the other hand, macroscopic objects are ordinarily governed by classical mechanics. Nonetheless, it is believed that the quantum fluctuations of a macroscopic system can be unveiled under extreme conditions. In this context, the main motivation of this project is to investigate quantum dynamics in a macroscopic system. Theoretically it is possible to isolate the quantum mechanical properties from the classical ones when the mechanical quanta energies ($\hbar\omega$) are not obscured by the thermal fluctuation energies ($k_B T$) [1, 5-8, 12]. Accordingly, a macroscopic resonator with GHz resonance frequency at sub-Kelvin temperature is demanded and such a resonator's displacement will be on the order of few femto-meters. Therefore, an ultra-sensitive and ultra-fast displacement sensor that is capable of detecting femto-meter fluctuations at GHz measurement speed is required to detect the motion of such mechanical resonator. Several research groups have been working at the edge of nanotechnology to develop a high-performance resonator-sensor system and achieve this measurement sensitivity. Realization of such an experiment may lead scientists to answer some of the most fundamental questions of physics, such as why quantum mechanical phenomena are not observed in the macroscopic world; how and under what conditions the transition between the classical mechanics and quantum mechanics occurs.

In this context, the most promising systems are nano-electro-mechanical systems (NEMS). Even though sensitivities close to quantum limit have been reported [4, 40, 42, 48] with NEMS, no quantum signature has been observed experimentally yet. Present displacement sensor technologies utilized in NEMS have either reached their physical limits [44] or their sensitivities are degraded by some fundamental physical phenomena such as back-action of the sensor on the resonator [24, 25, 38]. Consequently, there is a constant search for new sensor technologies that will accomplish quantum limited displacement measurement. One of the proposed sensor technologies is the vacuum tunneling transducer, which detects the motion of a resonator by measuring the fluctuations in the tunneling current flowing between the resonator and a stable metal tip [54]. Theoretical calculations of vacuum tunneling transducer promise displacement sensitivity at the ultimate quantum limit [13, 14, 23, 54-61], yet its experimental application has been obstructed due to severe technological problems. In this thesis, we developed and tested a new method for the controlled fabrication of vacuum tunnel junctions between two stable suspended metal tips. This application can be extended to the built-in fabrication of the tunnel junction between a vibrating mechanical resonator and a metal tip.

1.2 Structure of the Thesis

Chapter 2 represents the basic theoretical information, concepts and analyses about the quantum-limited observation of a harmonic oscillator's motion. It starts with the discussion of under what conditions a normally classical macroscopic system starts to display quantum mechanical behavior. Then, the ultimate intrinsic quantum limit of a harmonic oscillator is calculated using Heisenberg's uncertainty principle. Afterwards, the discussion on the harmonic oscillator is extended to the discussion of a system consist of a harmonic oscillator, a displacement sensor and a thermal bath. The system is described with a fully-quantum mechanical approach and the maximum sensitivity of the displacement sensor set by quantum mechanics is calculated. The properties of a quantum-ideal displacement sensor are provided point by point.

In Chapter 3, nano-electro-mechanical systems (NEMS), which are the most suitable systems for the quantum measurement experiments, are introduced. First, the basic working principle of NEMS regarding the motion detection of a mechanical resonator is described. Secondly, the mechanical properties of the nano-mechanical resonators are provided focusing on their unique features concerning the detection of mechanical quanta. Finally, the concept of motion detection with ultra-fast and ultra-sensitive displacement sensors in NEMS is introduced and two different outstanding techniques widely experienced in literature, single electron transistor and optical interferometer, are discussed with their drawbacks.

Chapter 4 presents a displacement detector called as Vacuum Tunneling Transducer that was first proposed two decades ago but has not been experimentally realized yet. The chapter starts with an introduction to the vacuum tunneling and follows with an in-depth and complete discussion on the sensitivity limits and noise properties of a vacuum tunneling displacement sensor. In the final section, the technical obstacles in front of the realization of tunneling sensor are identified and possible solutions are proposed.

In Chapter 5, a new methodology is developed and tested for the fabrication of vacuum tunnel junctions in a highly controlled manner. First, present junction fabrication techniques in literature are discussed and the reasons why they are not applicable to the desired resonator-tunnel sensor system are pointed out. The advantage of the proposed fabrication technique over the present ones is clarified. Afterwards, the details of each fabrication step and experiment apparatus are provided. Finally, the rest of the section is devoted to the results and discussion of the experiment.

Chapter 6 is the conclusion of the thesis, which suggests technical improvements and provides the future aspects.

CHAPTER 2

QUANTUM MEASUREMENT ON MACROSCOPIC BODIES

The long-standing goal of detecting signatures of quantum mechanics in macroscopic bodies that demands performing measurements at the quantum limit. The first attempt was to detect very weak gravitational waves with gravitational wave antennas. A gravitational wave detector can be thought of as a quantum harmonic oscillator acted upon by a weak force and the sensitivity of the force detection is ultimately limited by the quantum mechanics. Therefore, quantum limits of the measurement of a quantum oscillator's motion have been examined intensively by the gravitational wave community starting with 1970s [1]. A second wave of interest on quantum-limited displacement measurement arose with the development of nano-electro-mechanical systems (NEMS). NEMS consist of a nano-resonator and a nano-sensor that is coupled to the resonator. The nano-resonator can be modeled as a harmonic oscillator and the sensor converts its mechanical motion to electrical signal. In the beginning, the main motivation of NEMS community was performing ultra-sensitive measurements of nano-structures' mechanical properties such as mass detection [2], motion detection [3], strain detection [4] etc. In time, as the device sizes decrease and the measurement sensitivities increase, the NEMS have approached closer and closer to the quantum realm. As a result, the motivation for performing ultra-sensitive measurement using NEMS, eventually turned into an effort to detect the intrinsic quantum mechanical properties of the nano-structure [5, 6].

Even though both communities involved in theoretical and experimental research to understand the limits set by the quantum mechanics to the displacement measurement of a harmonic oscillator, there are two major differences between them in terms of their sources of motivation. First of all, in gravitational wave detection, the aim is to determine the minimum force detectable by a quantum oscillator. On the other hand, the biggest motivation of NEMS community is to observe the quantum mechanical features of the oscillator itself like mechanical quanta, or zero-point fluctuations. In the second place, low "*thermal occupation number, n_{th}*" [7] is desired in order to be able to approach the quantum realm and this criterion is met by the nano-mechanical resonators rather than the gravitational wave antennas. Since the motivation of this thesis is to detect the intrinsic quantum mechanical behavior of a macroscopic body using displacement detection, mainly the approach of NEMS community will be followed. In NEMS, the macroscopic object under test is generally a nano-resonator that can effectively be modeled as a harmonic oscillator. Therefore, throughout this chapter, the analyses that are specific to harmonic oscillators will be presented. The discussion starts with the basic criterion to be met by a harmonic oscillator to enter the quantum realm, which is low thermal occupation number. Then, the minimum uncertainty for the two consecutive measurements of a harmonic oscillator's displacement will be examined which is called as *standard quantum limit* or *zero point fluctuations*. Finally, the criteria that a sensor/detector must fulfill in order to be able to perform continuous measurements at ultimate quantum limit will be introduced using a fully quantum dynamical approach.

2.1   Quantum-Classical Transition: Thermal Criterion

The basic criterion to be met by a harmonic oscillator for entering the quantum realm is to get rid of the thermal fluctuations that obscure the quantum dynamics of the oscillator. If the temperature of the oscillator is not low enough, thermal fluctuations will overcome the very-weak quantum signals to be detected. A quantity called "*thermal occupation number, n_{th}*" is introduced to give an idea about how low the temperature should be [7]. Thermal occupation number of a harmonic oscillator is given by the Bose-Einstein distribution function

$$\langle n_{th}\rangle = \frac{1}{2} + \left(e^{\hbar\omega/k_B T} - 1\right)^{-1},\qquad\qquad(2.1)$$

where $\hbar$ is the Planck's constant, k_B is the Boltzman's constant, $\omega/2\pi$ is the oscillator's frequency and T is the equilibrium temperature of the resonator and its environment [7].

Thermal occupation number can be thought as the number of mesoscopic phonons in the oscillator for the given particular state. Each phonon has an energy of $\varepsilon = \hbar\omega$, which is called as "*mechanical quantum*" [8]. Consequently, the total energy of the quantum oscillator can be expressed as $E = \langle n_{th}\rangle\varepsilon$. It is obvious that the 1/2 term in Equation 2.1 is included in order to take into account the ground state energy of the harmonic oscillator. As mentioned before, the most basic criterion to enter the quantum realm is to eliminate the classical fluctuations. In accordance, to reveal the quantum dynamical properties of the oscillator, the mechanical quanta $\hbar\omega$ should be larger than or at least comparable to the classical thermal fluctuations $k_B T$. In other words, in a quantum measurement, high $\hbar\omega/k_B T$ ratio is desired which yields to a low thermal occupation number. In Figure 2.1, the thermal occupation number is plotted as a function of resonator's frequency for different temperatures ranging from sub milli-Kelvin to room temperature. This graph clearly shows that small n_{th} is achieved for very-low temperatures and ultra-high resonance frequencies.

Low n_{th} can be achieved in NEMS contrary to the gravitational wave resonators and antennas. Because, low temperatures and high resonance frequencies are easily accessible for nano-resonators as opposed to the bulky gravitational wave antennas. A nano-mechanical beam with 1 GHz resonant frequency has recently been reported [9] and milli-Kelvin temperatures are routinely achieved which corresponds to a thermal occupation number around unity. This is a significant feature of NEMS, since a resonator with low thermal occupation number monitored with an ultra-sensitive detector, promises the possibility of detecting quantum mechanical behavior in macroscopic systems.
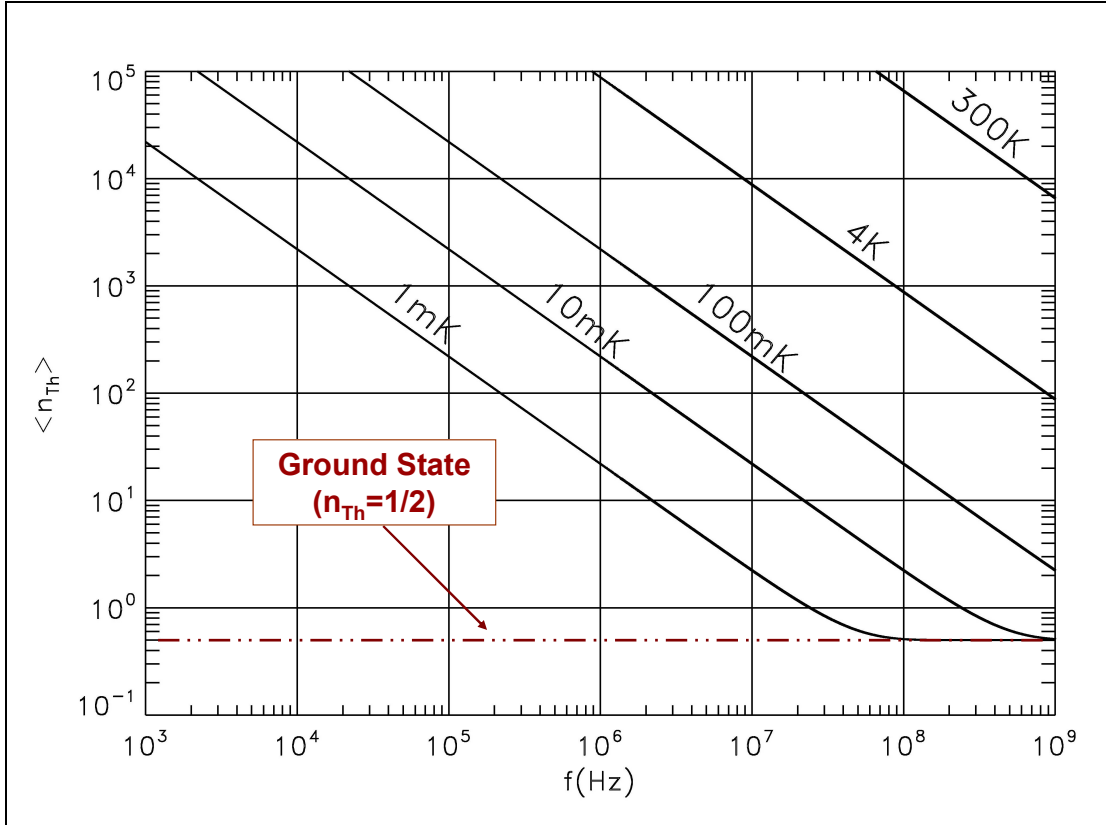
Figure 2.1: Thermal occupation number of a harmonic oscillator is given as a function of oscillator's resonance frequency for a wide range of temperatures from 1mK to 300 K. Ground state energy accounts for the ½ term. Considering the experimentally achievable resonance frequencies (<GHz), a thermal occupation number of ½ can be obtained for temperatures below 10 mK.

2.2 Uncertainty Principle for a Quantum Harmonic Oscillator

In classical mechanics, one can measure an objects position and momentum with arbitrary precision. On contrary, quantum mechanics entails an ultimate limit to the knowledge of an oscillator's position and momentum. This limit is rooted directly in the Heisenberg Uncertainty Principle [10]

$$\Delta x \Delta p \geq \frac{\hbar}{2}.$$ (2.2)

Uncertainty principle implies that a quantum object cannot have precisely defined values of position and momentum simultaneously. It results from the fact that, in quantum mechanics observables have probability distributions rather than exact values. Here, Δx and Δp are the root-mean-square deviations of position and momentum from their mean values

$$\Delta x = \sqrt{\left\langle x^2 \right\rangle - \left\langle x \right\rangle^2} \, , \tag{2.3}$$

$$\Delta p = \sqrt{\left\langle p^2 \right\rangle - \left\langle p \right\rangle^2} \, . \tag{2.4}$$

Even though uncertainty relation is a fundamental property of a quantum object's physical state, it can also be used to define the uncertainty in the measurement of observables such as position and momentum

$$\Delta x_{measurement} \Delta p_{perturbation} \geq \frac{\hbar}{2} \, . \tag{2.5}$$

In this equation, position uncertainty $\Delta x_{measurement}$, is the error in the measurement of the position, and the momentum uncertainty $\Delta p_{perturbation}$, is the perturbation on the oscillator caused by the measurement process [8]. Overall, one can think of the Uncertainty Principle either as an intrinsic property of a quantum object due to the statistical nature of quantum mechanics or as an observer effect on the quantum object.

The same approach applies when one attempts to determine the quantum limit to the sensitivity of a quantum oscillator's displacement measurement. As mentioned before, it is vital to obtain low thermal occupation numbers ($k_B T \leq \hbar\omega$) in order to detect mechanical quanta of a mechanical resonator. Even though the answer is not clear to the question of how low the temperature has to be, the starting point will be the limit where temperature approaches 0° K. This extremum is named as the "ground state" or "freeze-out" of the oscillator and it is the minimum-energy state for a harmonic oscillator.

In this section, the Uncertainty Principle will be applied to a harmonic oscillator in ground state, using the two different interpretations of the principle as given above [8]. The first interpretation uses the probabilistic nature of position and momentum states of the oscillator to determine the fluctuation in the position of the oscillator in its ground state, which is called the *"Zero Point Fluctuation"*. The second interpretation uses the uncertainty for a measurement process to determine the possible minimum error for two consecutive measurements of the position for a quantum oscillator in its ground state, which is called the *"Standard Quantum Limit"*. As might be expected these two different approaches will give the same result.

2.2.1 Zero-Point Fluctuations

Zero-point fluctuation is defined as the variation in the oscillator's position at $0°$ K in ground state [8]. The ground state is the minimum energy-state of the oscillator. Therefore, the derivation given here consists of writing the energy of the oscillator as a function of oscillator's displacement and finding the displacement that minimizes this energy. To begin with, the average energy of a harmonic oscillator is

$$\langle E \rangle = \frac{\langle p^2 \rangle}{2m} + \frac{K \langle x^2 \rangle}{2}, \tag{2.6}$$

where m is the mass of the oscillator, and $K = m\omega^2$ is the spring constant. As mentioned before in the definition of Heisenberg's Uncertainty Principle, $\langle x^2 \rangle$ and $\langle p^2 \rangle$ are given by the equations

$$\langle x^2 \rangle = \langle x \rangle^2 + (\Delta x)^2, \tag{2.7}$$

$$\langle p^2 \rangle = \langle p \rangle^2 + (\Delta p)^2. \tag{2.8}$$

Since the aim is to calculate the minimum energy, the mean values of the position and the momentum is taken to be zero which means $\langle x \rangle = \langle p \rangle = 0$. In this case, Equation 2.6 becomes

$$\langle E \rangle = \frac{(\Delta p)^2}{2m} + \frac{K(\Delta x)^2}{2}. \tag{2.9}$$

Using the equality condition of uncertainty principle, one can substitute $\Delta p \approx \hbar/2\Delta x$ in order to express the energy equation as a function of the position fluctuations only

$$\langle E \rangle = \frac{\hbar^2}{8m(\Delta x)^2} + \frac{m\omega^2(\Delta x)^2}{2}. \tag{2.10}$$

Finally, the value of Δx that minimizes the total energy of the oscillator can be found by taking the derivative of energy equation with respect to Δx and equating it to zero

$$\left. \frac{d\langle E \rangle}{d(\Delta x)} \right|_{\Delta x = \Delta x_{zp}} = 0. \tag{2.11}$$

$$\Delta x_{zp} = \sqrt{\frac{\hbar}{2m\omega}}, \tag{2.12}$$

Equation 2.12 gives the displacement fluctuation that minimizes the total energy and it is called as the *"zero-point fluctuations"* of the oscillator in its ground state [8]. The corresponding zero-point momentum fluctuations and the minimum energy of the oscillator are given by

$$\Delta p_{zp} = \sqrt{\frac{\hbar m\omega}{2}}, \tag{2.13}$$

$$\langle E \rangle_{min} = \frac{\hbar\omega}{2}. \tag{2.14}$$

These zero-point fluctuations in position and momentum imply that even when the resonator is frozen-out, there are some residual fluctuations in the oscillator's position, and momentum. This is an intrinsic fundamental property of the resonator's quantum state.

2.2.2 Standard Quantum Limit (SQL)

The same result that is found for the zero-point fluctuation can be calculated from the measurement point of view. For one single instant measurement, one can measure the position arbitrarily accurately. However, for two or more successive measurements the precision is limited due to the back action of the momentum uncertainty on the succeeding position measurement. In Heisenberg representation, the equations of motion for the position and momentum of an oscillator are given by [11]

$$x(t) = x(0)\cos \omega t + \frac{p(0)}{m\omega}\sin \omega t, \tag{2.15}$$

$$p(t) = -m\omega x(0)\sin \omega t + p(0)\cos \omega t. \tag{2.16}$$

The expectation values of $x(t)$ and $p(t)$ will oscillate in time with the given corresponding variances [1]

$$(\Delta x(t))^2 = (\Delta x(0))^2 \cos^2 \omega t + \left(\frac{\Delta p(0)}{m\omega}\right)^2 \sin^2 \omega t, \tag{2.17}$$

$$(\Delta p(t))^2 = (-m\omega\Delta x(0))^2 \sin^2 \omega t + (\Delta p(0))^2 \cos^2 \omega t, \tag{2.18}$$

The Equation 2.17 implies that an initial position measurement is performed with a measurement error of $\Delta x(0)$ and then it is followed by a second measurement for which one must take into account the effect of the momentum perturbation coming from the first measurement. The momentum perturbation as a result of the first measurement is given by the Uncertainty Principle $\Delta p(0) \geq \hbar/2\Delta x(0)$. This inequality is inserted into Equation 2.17 to find $\Delta x(t)$ as a function of the $\Delta x(0)$ only

$$(\Delta x(t))^2 \geq (\Delta x(0))^2 \cos^2 \omega t + \left(\frac{\hbar}{2m\omega\Delta x(0)}\right)^2 \sin^2 \omega t, \tag{2.19}$$

From Equation 2.19, the initial position measurement error $\Delta x(0)$ that minimizes the position uncertainty in $x(t)$

$$\Delta x(0)_{min} = \sqrt{\frac{\hbar}{2m\omega}} \equiv \Delta x_{SQL} . \qquad (2.20)$$

This is called the "Standard Quantum Limit" [8]. The preceding calculations imply that in order to minimize the error for two consecutive quick measurement of position, the error in the first measurement should be chosen such that it projects the oscillator into a minimum uncertainty state. Therefore, for two sequential measurements, one must perform the first measurement with a measurement error equal to Δx_{SQL} in order to minimize the imprecision of the second measurement.

"*Standard Quantum Limit*" or "*Zero-Point Fluctuations*" give the ultimate limit for the sensitivity for the position measurement of a quantum harmonic oscillator. This is the physical fundamental limit determined by the quantum mechanics intrinsic to oscillator. In other words, the aim of quantum measurements can be stated as to detect the position of an oscillator with a sensitivity that is close to the SQL of the oscillator. In this context, the sensitivity of a sensor is generally expressed as multiples of resonator's SQL. The Equations 2.12 and 2.20 show that, the zero-point fluctuations or the SQL increases with decreasing $m\omega$. This product is much smaller for the nano-resonators than for the gravitational wave-antennas. Therefore, the SQL of a nano-resonator is much larger than the SQL of a gravitational antenna which indicates that nano-resonators should reveal their quantum properties at a much larger length scale. For a quick comparison, a typical nano-resonator with a mass of 10^{-16} kg and resonance frequency of 100 MHz [6] will result in a SQL of 3×10^{-14} m. On the other hand, a typical gravitational wave detector will have a mass of 10^3 kg and resonance frequency of 1 kHz [1], which yields a SQL of 3×10^{-21} m. The SQL of nano-resonator is order of magnitudes larger than the SQL of the wave-antenna and hence the quantum dynamics should be detectable at much larger length scales in NEMS. Altogether, these calculations simply show that it is much easier to approach the SQL using NEMS and NEMS are promising systems for detecting quantum behavior in a macroscopic body.

2.3   Displacement Detection in Quantum Mechanics

In the previous part, the minimum uncertainty in the knowledge of an oscillator's position is calculated just for two consecutive, instant measurements but not for a continuous measurement. Also, only the uncertainty that is coming from the oscillator itself is taken into account. However, there is an unavoidable noise contribution from the sensor which monitors the position of the resonator [12]. In this section, the effects of the sensor on the measurement sensitivity will be discussed in detail. The minimum noise contribution of the sensor allowed by quantum mechanics and the criteria to be met by the sensor in order to operate at this ultimate quantum limit will be elaborated. Throughout this discussion, a quantum mechanical approach will be employed [13-15] rather than the classical/semi-classical ones [1] due to the fact that the former directly addresses the questions regarding the quantum limit to the continuous position detection in nano-systems. These recent theoretical studies [13-15], have provided a fully quantum-mechanical description for a quantum ideal amplifier and calculated the minimum noise contribution to the measurement sensitivity by such an amplifier. In the first part, as an essential base, a short introduction on the formalization of a quantum harmonic oscillator coupled to a lossy and noisy environment is provided. In the second part, the quantum description for a quantum mechanically ideal displacement sensor is conveyed.

2.3.1 Dissipation and Noise

In this part, both the classical and quantum mechanical formalisms for the oscillator-environment systems either in equilibrium or out-of equilibrium are discussed. The main emphasis will be on the noise and dissipation properties of the systems and the differences between the classical and quantum approaches will be underlined. This part aims to provide basic background information necessary for the next section through which the quantum limit of the position detection in a resonator-sensor-thermal bath system will be discussed.

CLASSICAL DISSIPATION AND NOISE:

In classical mechanics, the equation of motion for a damped simple harmonic oscillator in a thermal bath is given by the Langevin equation [16]

$$m\frac{d^2x}{dt^2} + m\omega_0^2 x = -m\gamma\frac{dx}{dt} + F(t),$$ (2.21)

where m is the mass, ω_0 is the frequency, and $x(t)$ is the position of the oscillator. The right hand side of the equation corresponds to the environmental force acting on the oscillator. The first term is the dissipation (loss) term characterized by a dissipative constant γ, and the second term is the noisy random force $F(t)$ that is exerted on the oscillator by the environment. In other words, these terms represent the friction and the noise respectively. In general, the dissipative constant γ is defined such that, the random force fluctuates around zero [17]

$$\langle F(t) \rangle = 0.$$ (2.22)

In thermal equilibrium, $F(t)$ must result in equipartition: $\langle v^2/2 \rangle = k_B T/m$. Therefore, it should satisfy the following autocorrelation function, assuming that random force is time-uncorrelated [16]

$$R_{FF}(s) = \langle F(t)F(t+s) \rangle = 2mk_B T_{bath}\gamma\delta(s).$$ (2.23)

Equation 2.23 gives the classical fluctuation-dissipation relation for the harmonic oscillator.

The power spectral density of a random force in frequency domain gives us the power of the noise as a function of the frequency and it is defined as the Fourier transform of the autocorrelation function [18]

$$S_F(\omega) = \int_{-\infty}^{\infty} R_{FF}(s) e^{-i\omega s} ds = 2m\gamma k_B T_{bath}. \tag{2.24}$$

Equation 2.24 indicates that for this particular system, power spectral density of the random force is independent of the frequency. This result is valid only for oscillator-environment systems that are in thermal equilibrium and the equation of motion can be described with a stationary Gaussian noise, which has a probability density function of the Gaussian distribution and a constant dissipation term.

On the other hand, the equations and assumptions given above are realistic as long as the time scale of the oscillator is much larger than the time scale of molecular motion in its environment. However, for some systems the time scale of the oscillator is comparable with the time scale of the environment. This is also true for the resonator-sensor systems analyzed in this thesis and in these systems, while describing the motion of the oscillator the sensor is modeled as a part of the environment. Since the time scales of nano-resonator and sensor are comparable, the equations given above cannot be used to describe the effect of the sensor on the resonator. In this case, the assumptions of frequency independent dissipation constant, white noise and time-uncorrelated random force are not applicable. When these assumptions are abandoned, and a time-dependent dissipation is introduced, it gives the more realistic Generalized Langevin equation [19]

$$m\ddot{x} + m\omega_0^2 x = -\int m\gamma(t - t')\dot{x} dt' + F(t). \tag{2.25}$$

In this equation $\gamma(t)$ represents the retarded effect of the friction force and is known as the damping kernel [15]. Parallel to the formalism of Langevin equation, the power spectral density of the fluctuating force can be written as

$$S_F(\omega) = 2m\gamma(\omega) k_B T_{bath}, \tag{2.26}$$

where $\gamma(\omega)$ is the Fourier transform of the damping kernel. It can be easily noticed that, the noise is no longer a white noise but has a frequency dependence via $\gamma(\omega)$.

The equations given above are purely classical descriptions of a harmonic oscillator that is in thermal equilibrium with its environment. For the oscillator-thermal bath systems where the molecular motion in the bath is much faster than the internal dynamics of the oscillator, the classical Langevin equation with time-independent dissipation constant and noise spectrum can safely be used. On the other hand, while describing the effect of the sensor on the oscillator a generalized Langevin description with time-dependent dissipation and noise spectrum is needed.

QUANTUM DISSIPATION AND NOISE:

In the quantum approach, the quantum oscillator is coupled to some other quantum systems that act as a bath. The Hamiltonian of this quantum oscillator is given by [15]

$$\hat{H} = \frac{\hat{p}^2}{2m} + \frac{1}{2}m\omega^2\hat{x}^2 + \hat{H}_{bath} - \hat{x}\cdot\hat{F}, \qquad (2.27)$$

where $\hat{p}$ and $\hat{x}$ are the momentum and position operators of the oscillator and $\hat{F}$ is the operator in the Heisenberg's representation that represents the noisy force exerted on the oscillator by the bath which is also called as the *back-action force*. The quantum spectral density of the back-action force at zero coupling is given by the Fourier transform of the correlator

$$S_F(\omega) = \int_{-\infty}^{\infty}\left\langle\hat{F}(t)\hat{F}(0)\right\rangle e^{i\omega t}dt. \qquad (2.28)$$

This quantum noise is different from its classical counterpart in three important ways [15]. First of all, as a result of its quantum nature it has zero-point fluctuations and hence does not vanish as the temperature approaches zero. Secondly, the minimum value of quantum noise is strictly determined by Heisenberg uncertainty principle. Last but not least, contrary to the classical mechanics, in quantum approach the spectral densities of positive and negative frequencies are not equal to each other, meaning $S_F(\omega) \neq S_F(-\omega)$. The physical interpretation of this property can be understood by writing the spectral density in terms of the exact eigenstates of the bath [15]

$$S_F(\omega) = 2\pi \sum_{f,i} \rho_{ii} \left| \left\langle f \left| \hat{F} \right| i \right\rangle \right|^2 \delta(E_f - E_i + \hbar\omega), \qquad (2.29)$$

where ρ_{ii} is the diagonal element in the density matrix (number of states per unit energy), f and i are bath's energy eigenstates with eigenvalues of E_f and E_i, respectively. The only non-zero value of Dirac delta function is obtained when $E_f - E_i + \hbar\omega = 0$. So if the bath transits from a lower energy state to a higher one ($E_f > E_i$) by adsorbing energy from the oscillator, then the frequency should be negative ($\omega < 0$). On contrary, if the bath falls from a higher energy state to a lower one ($E_f < E_i$) by giving energy to the oscillator, then the frequency should be negative ($\omega < 0$). In brief, negative frequencies give the emission spectrum of the oscillator and the positive frequencies give the adsorption spectrum. We can conclude that in quantum mechanics, there can also be an energy transfer from bath to the oscillator, which facilitates positive damping which is unlikely in classical mechanics. The ratio of the positive and negative spectral densities is given by ratios of the transition rates between the bath's energy states [21]

$$\frac{S_F(\omega)}{S_F(-\omega)} = \frac{\Gamma_{E+\hbar\omega \to E}}{\Gamma_{E \to E+\hbar\omega}}, \qquad (2.30)$$

where $\Gamma_{E+\hbar\omega \to E}$ is the transition rate for the bath to go from the higher energy state to the lower energy state by transferring energy to the oscillator and $\Gamma_{E \to E+\hbar\omega}$ is the transition rate for the bath to go from the lower energy state to the higher one by adsorbing energy from the oscillator. At equilibrium, this ratio is set by the equilibrium temperature [22]

$$\frac{S_F(\omega)}{S_F(-\omega)} = e^{-\hbar\omega/k_B T}. \qquad (2.31)$$

Therefore, the asymmetry between the adsorption and emission rates is determined by the temperature at equilibrium.

17

On the other hand, in many quantum nano-systems, the oscillator and its environment is not in thermal equilibrium. For instance, almost all of the sensor-resonator systems are out-of equilibrium. However, most of these non-equilibrium systems can be modeled as an effective equilibrium system with the effective temperature T_{eff} [23-25]. In this modeling, the ratio given in equation 2.31 is used to define the effective temperature of the effective bath [15]

$$T_{eff}(\omega) = \frac{\hbar\omega}{k_B}\left(\ln\left(S_F(\omega)\Big/S_F(-\omega)\right)\right)^{-1}.$$

(2.32)

This effective temperature is neither a physical temperature nor a noise temperature. It is a measure of the asymmetry between the emission and adsorption in a non-equilibrium bath and it is frequency-dependency is a consequence of being out-of-equilibrium. Using Equation 2.32, one can understand how a non-equilibrium system acts as an effective equilibrium bath with the knowledge of the quantum noise spectrums of $S_F(\omega)$ and $S_F(-\omega)$.

Despite the mentioned differences between classical and quantum noises for a harmonic oscillator, the symmetric and asymmetric parts of the quantum noise imitate some classical quantities. It has been calculated that [15], the symmetric part of the quantum noise $\bar{S}_F(\omega)$, acts like the noise spectrum of the classical fluctuating force in the Langevin equation $F_{classical}(t)$. Additionally, the asymmetric part of the quantum noise gives us the classical kernel damping. Therefore, using these expressions it is possible to write a classical looking Generalized Langevin equation to describe a quantum harmonic oscillator

$$m\ddot{x} + m\omega_0^2 x = -\int m\gamma(t-t')\dot{x}dt' + F(t),$$

where

$$\gamma = \frac{1}{2m\hbar\omega}[S_F(\omega) - S_F(-\omega)],$$

(2.33)

$$S_{F,classical}(\omega) = \bar{S}_F(\omega) = \frac{S_F(\omega) + S_F(-\omega)}{2}.$$

(2.34)

As a last comment, recall that in classical mechanics, the noise spectrum of random force is given by the equation $S_{F,classical}(\omega) = 2m\gamma k_B T_{bath}$ at thermal equilibrium. A similar expression is presented for the quantum harmonic oscillator by the Caldeira-Leggett model [20]. In this model, the quantum environment is thought as a set of harmonic oscillators linearly interacting with the quantum oscillator at equilibrium. In this case, the thermal fluctuation energy of $k_B T_{bath}$ in the classical noise spectrum expression is replaced by the energy of the set of harmonic oscillators, which is $(1/2)\hbar\omega\coth(\hbar\omega/2k_B T_{bath})$ [20]. Consequently, at equilibrium the quantum power-noise spectra for the fluctuating force becomes

$$\overline{S}_F(\omega) = m\gamma\hbar\omega\coth(\frac{\hbar\omega}{2k_B T_{bath}}). \qquad (2.35)$$

2.3.2 Quantum-Ideal Position Sensor

After stating the basic properties of quantum noise and establishing a simple quantum mechanical description for quantum nano-systems in the previous section, we would like to turn back to the question of what is ultimate limit set by the quantum mechanics to the sensitivity of a sensor for continuous position measurement. For this purpose, we will discuss the Aashish Clerk's paper on the position detection for a quantum harmonic oscillator weakly coupled to a linear amplifier [13]. A generic system is shown in Figure 2.2.

To begin with, consider a quantum harmonic oscillator coupled both to a thermal bath in equilibrium and to a detector that is not in equilibrium. The Hamiltonian of the system can be written as

$$\hat{H} = \hat{H}_{oscillator} + \hat{H}_{bath} + \hat{H}_{interaction}. \qquad (2.36)$$

In this equation, the first term is the Hamiltonian of a free simple harmonic oscillator, which is $\hat{H}_{oscillator} = \hat{p}^2/2m + (1/2)m\omega^2\hat{x}^2$. The second term represents the Hamiltonian due to the coupling to an equilibrium bath with temperature T_{bath}.
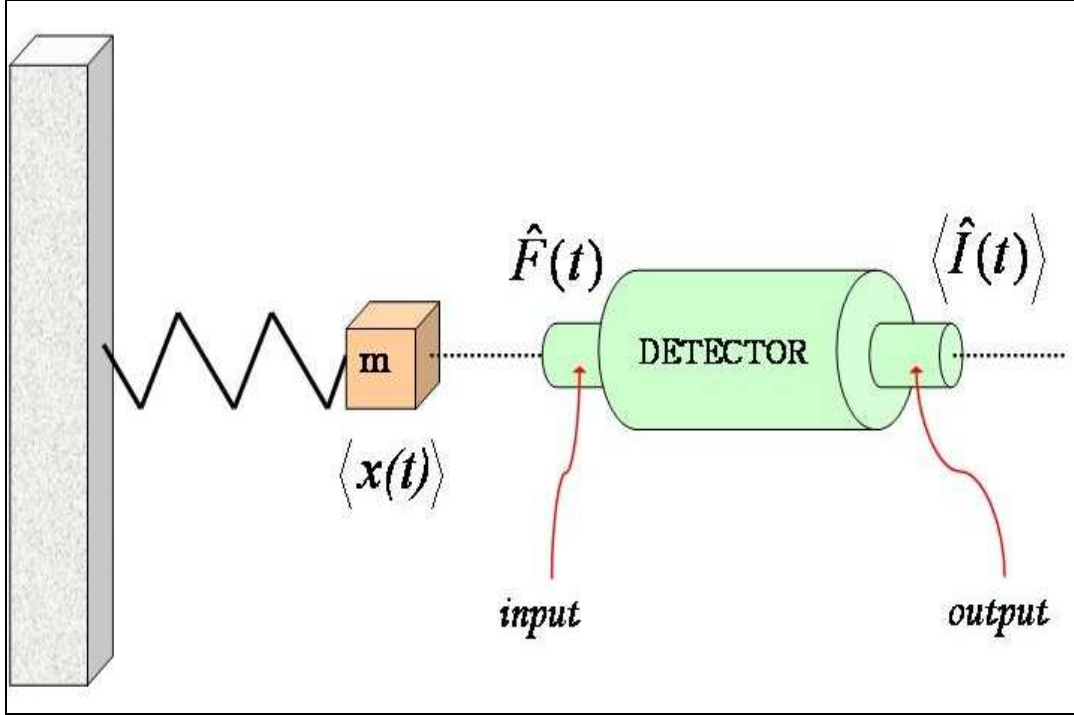
Figure 2.2: The re-illustration of Clerk's generic amplifier [13]. Here the mass m attached to the spring represents the resonator and it is coupled linearly to the detector. $\hat{F}(t)$ and $\hat{I}(t)$ are the input and output operators of the detector, respectively.

The last term in Equation 2.36, stands for the non-equilibrium part of the system that is the interaction between the oscillator and the sensor

$$\hat{H}_{\text{interaction}} = A\hat{F} \cdot \hat{x}, \tag{2.37}$$

where A is the dimensionless coupling strength, and $\hat{F}$ is the back-action of the detector on the resonator. Throughout this discussion, it is assumed that the resonator is weakly coupled to the detector, which is a realistic assumption for the experiments done by NEMS [15]. There are two important consequences of weak-coupling assumption. First of all, as a result of weak coupling, the detector's output current changes linearly with the motion of oscillator [13]

$$\langle I(t) \rangle = A \int_{-\infty}^{\infty} \lambda(t - t') \langle \hat{x}(t') \rangle dt', \tag{2.38}$$

where λ is the gain of the amplifier and it is given by the Kubo formula as [26]

$$\lambda(t-t') = -\frac{i}{\hbar}\theta(t-t')\left\langle\left[\hat{I}(t),\hat{F}(t')\right]\right\rangle. \qquad (2.39)$$

Here $\theta(t)$ is the Heaviside function and is equal to one for positive values of time and zero otherwise. The Equation 2.39 implies that in order to have a non-zero gain, the input and output operators of detector should not commute for all the times. In other words, to have a non-zero gain, detector has to be out-of equilibrium.

The second consequence of weak coupling is that we can describe the quantum dynamics of the oscillator with a classical looking Langevin-like equation [13]

$$m\ddot{x} + m\omega_0^2 x = \left\{-\gamma_0\dot{x} + F_0\right\} + \left\{-A^2\int\gamma(t-t')\dot{x}(t')dt' + A\cdot F(t)\right\}, \qquad (2.40)$$

where m and ω_0 are the renormalized mass and frequency of the oscillator. The first curly bracket on the RHS of the equation is the dissipation and fluctuation coming from the equilibrium bath with a constant damping γ_0 and fluctuating force F_0. The fluctuation-dissipation relation for this equilibrium bath can be written using the Equation 2.35

$$\bar{S}_{F_0}(\omega) = \gamma_0\hbar\omega\coth\left(\frac{\hbar\omega}{2k_B T_{bath}}\right). \qquad (2.41)$$

The second curly bracket term in Equation 2.40 represents the effect of the out-of equilibrium detector on the oscillator. The $A^2\gamma$ term is the damping due to detector and $A\cdot F$ is the fluctuating back-action of the detector on the resonator. The relation between the quantum noise and the damping has already given in the previous section with the Equation 2.33

$$\gamma(\omega) = \frac{1}{2\hbar\omega}\left[S_F(\omega) - S_F(-\omega)\right]. \qquad (2.42)$$

21

Additionally, it has also been mentioned that out-of equilibrium systems, like the detector in the present case, can be modeled as an effective bath with an effective temperature. Therefore, the fluctuation-dissipation theorem for the detector can be written like an equilibrium bath with temperature $T_{\det ector}$

$$\overline{S}_F(\omega) = \gamma(\omega)\hbar\omega\coth\left(\frac{\hbar\omega}{2k_B T_{\det ector}}\right). \tag{2.43}$$

Using the weak-coupling assumption, the role of the equilibrium thermal bath and the non-equilibrium detector is formulized above. At this point, an expression for the detector's output noise can be found. Classically, the fluctuations at the output of the sensor can be written as

$$\delta I_{TOTAL}(\omega) = \delta I_0(\omega) + A\lambda(\omega)\cdot\delta x(\omega), \tag{2.44}$$

where the first term accounts for the detector's intrinsic fluctuations and the second term amplifies the fluctuations coming from the oscillator's motion. The value of $\delta x(\omega)$ is calculated from Equation 2.40 and then the result is inserted in Equation 2.44. After all, the spectral density of 2.44 will give the following expression

$$\begin{aligned} S_{I,TOTAL}(\omega) = S_I(\omega) + |g(\omega)|^2|\lambda(\omega)|^2\left[A^2 S_{F_0}(\omega) + A^4 S_F(\omega)\right] \\ -2A^2\operatorname{Re}[g(\omega)S_{IF}(\omega)] \end{aligned}, \tag{2.45}$$

where S_I, S_F, and S_{IF} are the classical noise correlators for the detector and $g(\omega)$ is the transfer function given by

$$g(\omega) = \left\{m[\omega^2 - \omega_0^2] + i\omega[\gamma_0 + \gamma(\omega)]\right\}^{-1}. \tag{2.46}$$

Clerk states that, to obtain the quantum mechanical version of Equation 2.45, one can simply put the symmetrized quantum noises $\overline{S}_I$, $\overline{S}_F$ and $\overline{S}_{IF}$ instead of the classical noise correlators. In that case, $S_{I,TOTAL}$ will give the total symmetrized quantum noise-power density at the output of the detector. Actually, validity of this statement has been proved for tunnel junctions [14]. The resulting quantum description can be converted into an equivalent displacement noise density as

$$S_{x,TOTAL}(\omega) = S_{x,\det ector}(\omega) + S_{x,bath}(\omega), \tag{2.47}$$

where

$$S_{x,\det ector}(\omega) = \frac{\overline{S}_I}{\left|\lambda(\omega)\right|^2 A^2} + A^2 \left|g(\omega)\right|^2 \overline{S}_F - \frac{2\operatorname{Re}\left[\lambda(\omega)^* g(\omega)^* \overline{S}_{IF}\right]}{\left|\lambda(\omega)\right|^2}, \tag{2.48}$$

$$S_{x,bath}(\omega) = \hbar \coth\left(\frac{\hbar\omega}{2k_B T_{bath}}\right)\left[-\operatorname{Im} g(\omega)\right]. \tag{2.49}$$

A quantum-mechanically ideal amplifier is the amplifier that adds the minimum amount of noise allowed by the quantum mechanics to the displacement measurement. Therefore, the parameters that minimize Equation 2.48, which describes the noise contribution coming from the detector, have to be found out. First of all, the first two terms in Equation 2.48 have opposite dependence on the coupling strength A. Consequently, there has to be an optimum value for the coupling strength for which $S_{x,\det ector}(\omega)$ becomes minimum. This optimum value can be easily found by equating the first and second terms in Equation 2.48

$$A_{optimum}^2 = \sqrt{\frac{\overline{S}_I(\omega)}{\left|\lambda(\omega)g(\omega)\right|^2 \overline{S}_F(\omega)}}. \tag{2.50}$$

The optimization of the coupling strength is not enough to make an amplifier quantum mechanically ideal. In addition, the quantum noise-power densities of the detector have to obey the quantum noise constraint set by the Uncertainty Principle

$$\overline{S}_I(\omega)\overline{S}_F(\omega) \geq \frac{\hbar^2}{4}\left(\mathrm{Re}[\lambda(\omega)]\right)^2 + \left(\mathrm{Re}[\overline{S}_{IF}(\omega)]\right)^2. \qquad (2.51)$$

Finally, Clerk demands that the dimensionless power gain of the detector should be much larger than unity. With this constraint one can assume that $\lambda(\omega)$ and $\overline{S}_{IF}(\omega)$ are pure real [13].

Now in order to minimize the detector noise $S_{x,\det ector}(\omega)$, we insert the $A_{optimum}$ as given in Equation 2.50, place the quantum noise constraint given in Equation 2.51 and finally demand $\lambda(\omega)$ and $\overline{S}_{IF}(\omega)$ to be real. Then the final result becomes [13]

$$S_{x,\det ector}(\omega) \geq 2|g(\omega)|\left[\sqrt{\left(\frac{\hbar}{2}\right)^2 + \left(\frac{\overline{S}_{IF}(\omega)}{\lambda(\omega)}\right)^2} - \frac{\cos[\phi(\omega)]\overline{S}_{IF}(\omega)}{\lambda(\omega)}\right], \qquad (2.52)$$

where $\phi(\omega) = \arg g(\omega)$. In this equation $S_{x,\det ector}(\omega)$ is a function of cross correlator $\overline{S}_{IF}(\omega)$ only and hence can be minimized with respect to it. The cross correlator value that minimizes the $S_{x,\det ector}(\omega)$ and the corresponding minimum value of $S_{x,\det ector}(\omega)$ are given as

$$\left.\frac{\overline{S}_{IF}(\omega)}{\lambda(\omega)}\right|_{optimal} = \frac{\hbar}{2}\cot\phi(\omega), \qquad (2.53)$$

$$\left.S_{x,\det ector}(\omega)\right|_{\min} = \hbar|\mathrm{Im}\, g(\omega)| = \lim_{T_{bath}\to 0} S_{x,bath}(\omega). \qquad (2.54)$$

The Equation 2.54 shows that a quantum-mechanically ideal amplifier creates a noise that is equal to the noise coming from the zero-temperature equilibrium bath which is equal to the one half of the mechanical quanta. The same result was already found by the semi-classical work of Caves in 1982 [12]. However, the advantage of this quantum mechanical approach is that it gives the criteria to reach the quantum limit point by point like a recipe.

To sum up, Clerk demands three requirements from a displacement sensor in order to be able to perform measurement at ultimate quantum limit:

1. The coupling strength between the sensor and resonator should satisfy Equation 2.50.
2. The detector should satisfy the ideal noise condition, which is the equality of Equation 2.51.
3. The cross-correlator $\overline{S}_{IF}(\omega)$ should satisfy Equation 2.53.

Many experimentally outstanding sensors do not satisfy the conditions given above, like single electron transistor in the sequential tunneling regime [13]. On the other hand tunneling junctions, which is the sensor we propose, is an ideal amplifier that satisfies the requirements given above. The noise properties and ideality of the tunnel junction displacement sensors will be discussed in detail in Chapter 4.

CHAPTER 3

NANO-ELECTRO-MECHANICAL SYSTEMS (NEMS)

Nano-electro-mechanical systems (NEMS) consist of a mechanical resonator at nanometer/micrometer scale coupled to an electronic device of comparable dimensions. NEMS have small inertial masses and high operating frequencies. They are capable of performing ultra-fast and ultra-sensitive measurements of many different physical quantities like mass [2], displacement [4], and strain [22]. In addition to their importance in metrology, they also have interesting intrinsic properties in terms of their internal dynamics. Above all, NEMS are promising systems for the detection of quantum mechanical behavior in a macroscopic system. First of all, even though NEMS are nano-scale devices they are still "macroscopic" systems that consist of billions of atoms and have many degrees of freedom. Secondly, as mentioned in the previous chapter sub-mK temperatures and GHz frequencies are achievable for NEMS which provides low enough thermal occupation numbers to enter the quantum realm. Finally, the displacement sensitivities of NEMS can get closer to the zero-point fluctuation of the resonator under test. All in all, NEMS community have been working on the edge of the quantum realm and proved that NEMS are excellent candidates for quantum measurements. Researchers have been demonstrated many state-of-art devices that can operate very fast and have sensitivities very close to the quantum limit. On the other hand, despite this great effort, quantum mechanical behavior in a macroscopic system has not been observed yet.

In this section, consistent with the rest of the thesis, the particular focus will be on the position detection using NEMS. In the first part, the basic working principle of NEMS regarding position detection will be explained. In the following part, the mechanical properties of nano- resonators will be analyzed. Finally, different types of present sensors with an emphasize on their physical limits and the best sensitivities achieved by them will be discussed.

3.1 Working Principle of NEMS

NEMS are basically composed of a nano-mechanical resonator and a sensor that is coupled to the resonator. The basic working principle of NEMS is similar to conventional electro-mechanical systems [27]. The mechanical element is driven and its motion is monitored with the help of transducers. In NEMS, transducers convert electrical signal to mechanical stimuli or vice versa [28]. The transducer, which converts an electrical signal to a physical stimuli acting on the mechanical element, is called the *actuator* and the process is the *actuation*. On the other hand, the transducer, which converts the motion of the mechanical element to an electrical signal, is called the *sensor* and the process is *detection*. This basic working principle of NEMS is illustrated in Figure 3.1.
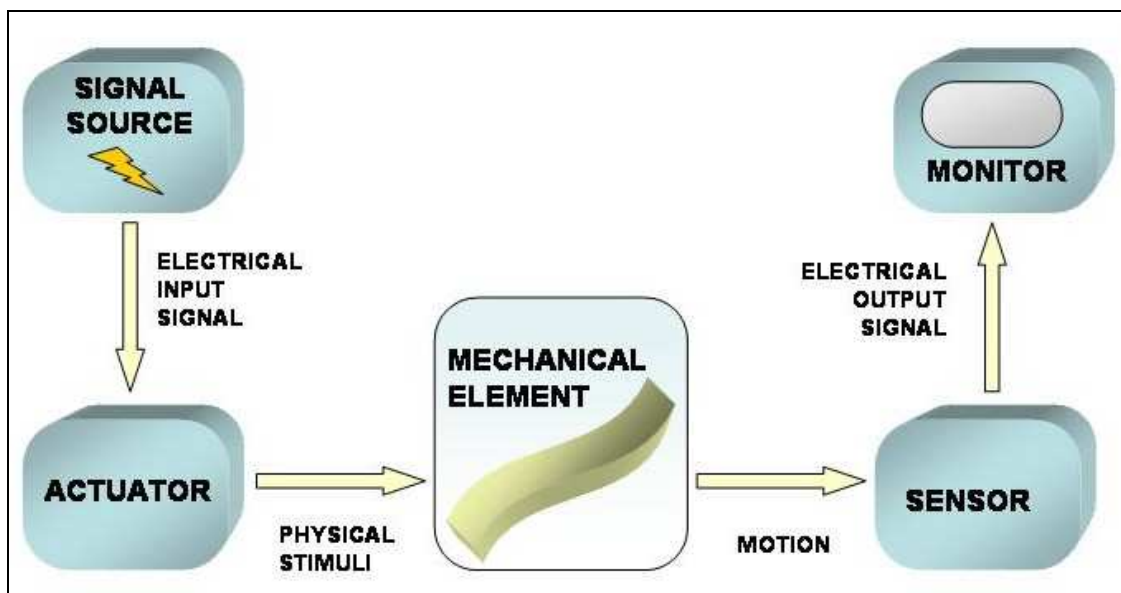

Figure 3.1: The Schematic shows the basic working principle of NEMS. The mechanical element is actuated and its position is monitored with a displacement sensor.

The actuation process in NEMS is quite standardized. On the other hand, the sensor design and detection process is the challenging step of motion detection. We will examine the actuation and detection separately in the following sections.

3.2 Nano-Mechanical Resonator and the Actuation Process

The nano-mechanical resonators used in NEMS are generally suspended flexural beams like doubly clamped beam or cantilever. These flexural beams at nanometer scales have frequencies in the microwaves and quality factors at tens of thousands. Since the most extensively used mechanical resonators are doubly clamped beams, here the calculations are carried out specifically for them.

RESONANCE FREQUENCY OF A DOUBLY CLAMPED BEAM:

A doubly clamped beam can be modeled by using the equations provided by the continuum theory. The resonance frequencies for the fundamental flexural modes of a doubly clamped beam can be calculated using the classical Euler-Bernoulli Beam equation with the following assumptions [29]:

1. The beam is a prismatic, untwisted and straight structure composed of an isotropic, linear elastic material.
2. The length of the beam is much larger than the width and thickness of the beam (1D).
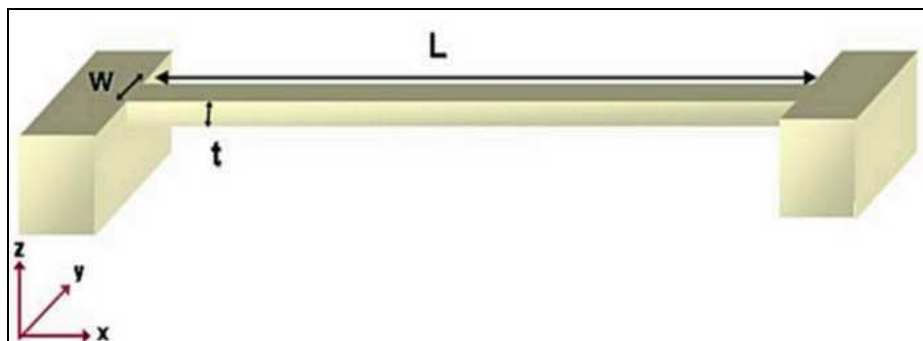3. Displacements from the equilibrium are very small compared to the length of the beam.

Figure 3.2: Schematic of doubly clamped beam, which is the most widely used mechanical resonator in NEMS. L, t and w are the length, thickness and width of the beam, respectively.

If $Y(x,t)$ is the displacement of the resonator's mid-point in the neutral-axis, and L, t and w are the length, thickness and width of the beam respectively, the equation of motion is given by [30]

$$\rho A \frac{\partial^2 Y}{\partial t^2} + EI \frac{\partial^4 Y}{\partial x^4} = 0 .$$ (3.1)

Here ρ is the density, A is the cross section, E is the Young's modulus and I is the second moment of area. For a doubly camped beam, it is given that $I = wt^3/12$. When the Equation 3.1 is solved using the boundary conditions of the doubly clamped beam $Y(0) = Y(L) = \dfrac{\partial Y}{\partial x}\Big|_{x=0} = \dfrac{\partial Y}{\partial x}\Big|_{x=L} = 0$, the equations of the vibrations for normal modes are found as [31]

$$Y(x,t) = a_n (\cos \beta_n x - \cosh \beta_n x) + b_n (\sin \beta_n x - \sinh \beta_n x) .$$ (3.2)

Here for the constants it is given that $a_n \approx b_n$, and they are found by normalizing the maximum displacement of the chosen mode to unity. From Equation 3.2, the normal mode frequencies are found as

$$\omega_n^2 = \frac{EI\beta_n^4}{\rho A} ,$$ (3.3)

where $\beta_n L$ is determined from the eigenvalue equation: $\cos \beta_n L \cosh \beta_n L = 1$. Additionally, when the expressions $I = wt^3/12$ and $A = wt$ are inserted into Equation 3.3 explicitly, the normal mode frequency becomes

$$f_n = \frac{(\beta_n L)^2}{2\pi\sqrt{12}} \sqrt{\frac{E}{\rho}} \frac{t}{L^2} .$$ (3.4)

The first three values of $\beta_n L$ can be found numerically [30] as $\beta_1 L = 4,783$, $\beta_2 L = 7,853$, and $\beta_3 L = 10,996$. The shapes of the corresponding modes are given in Figure 3.3.
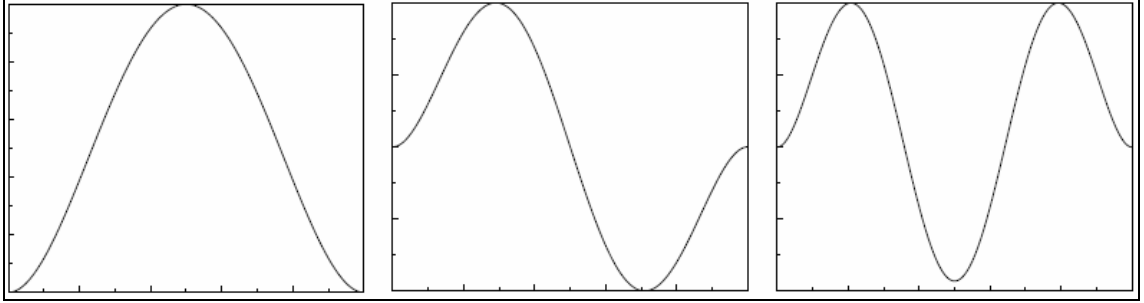

Figure 3.3: The shapes of the first three modes of a doubly clamped beam are shown.

The first normal mode (fundamental mode) has a resonance frequency of

$$f_0 = 1.05 \sqrt{\frac{E}{\rho}} \frac{t}{L^2}. \tag{3.5}$$

According to this formula, a silicon doubly clamped beam with dimensions $L \times w \times t = 2\,\mu m \times 100\,nm \times 200\,nm$ will have a fundamental resonance frequency of 800 MHz. On the other hand, the resonance frequency of a GaAs doubly clamped beam with the same dimensions will be around 400 MHz [32]. This calculation shows that the material type, which determines ρ and E, has also play a crucial role in determining the resonance frequencies. Stiffer materials with high elastic modulus should be preferred to increase the resonance frequency.

The measured resonance frequencies of experimentally demonstrated beams are generally lower than theoretically expected values because of non-idealities. Still, nano-mechanical resonators with a few-hundred MHz frequency are easily achieved and as an extreme, a SiC beam with a GHz fundamental frequency has been reported [9]. Overall, nano-mechanical resonators used in NEMS have fundamental frequencies at microwaves which is one of the two requirements to reach quantum limit along with the sub-mK temperature.
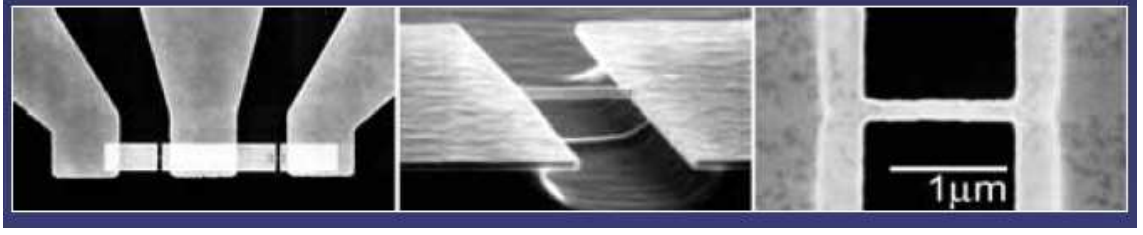
Figure 3.4: The SEM images of SiC beams produced by Huang et. al. at CALTECH are shown. The beam has two fundamental flexural-mode resonant mechanical responses at 1.014 and 1.029 GHz [9].

MECHANICAL QUALITY FACTOR (Q) OF A DOUBLY CLAMPED BEAM:

In addition to very-high resonance frequencies, another important property of nano-mechanical resonators is their high quality factors. The mechanical quality factor (Q) is a measure of the damping for a resonator [33]. In other words, high quality factor means that the resonator has a low internal dissipation (loss) which directly increases the sensitivity of the system. The quality factor of NEMS is in the range of 10^3-10^5, which is very large compared to the conventional electro-mechanical systems [34].

FUNDAMENTAL MODE MODEL FOR A NANO-RESONATOR

A doubly clamped nano-beam that is excited in its fundamental resonant mode can be modeled as a one-dimensional damped harmonic oscillator. The flexural motion of the beam in the vicinity of the fundamental resonance frequency is given in the time domain as [28]

$$M_{eff}\,\ddot{x}(t) + M_{eff}\,\gamma\,\dot{x}(t) + K_{eff}\,x(t) = f(t), \qquad (3.6)$$

where $x(t)$ is displacement of the resonator mid-point, $f(t)$ is the external driving force applied to the resonator, $M_{eff} = 0.735 Ltw\rho$ is the effective mass, $K_{eff} = 32Et^3w/L^3$ is the effective spring constant, and $\gamma = \omega_0/Q$ is the dissipation constant. The solution of the Equation 3.6 in the frequency domain is

$$X(\omega) = \frac{F(\omega)}{M_{eff}\left(\omega_0^2 - \omega^2 + \dfrac{i\omega\omega_0}{Q}\right)}. \qquad (3.7)$$

The application of a driving force on the nano-mechanical resonator is called as *"motion actuation"* [28]. Actuation is usually done by a transducer that converts an electrical signal to a mechanical force. There are many different actuation techniques like capacitive (electrostatic) actuation [35], thermal actuation [36], and piezoelectric actuation [37]. Besides all, the most extensively used technique is the magneto-motive actuation and here only this particular technique will be discussed.

In magneto-motive actuation technique, the Lorentz force is employed as the driving force [28]. When an alternating current at frequency ω is passed through the beam in the presence of a strong magnetic field perpendicular to the beam axis, a Lorentz force of $F(\omega) = LBI(\omega)$ is applied to the beam as shown in Figure 3.5 [6]. Here B is the magnitude of the static magnetic field, L is the length of the beam and $I(\omega)$ is the alternating current passing through the beam.
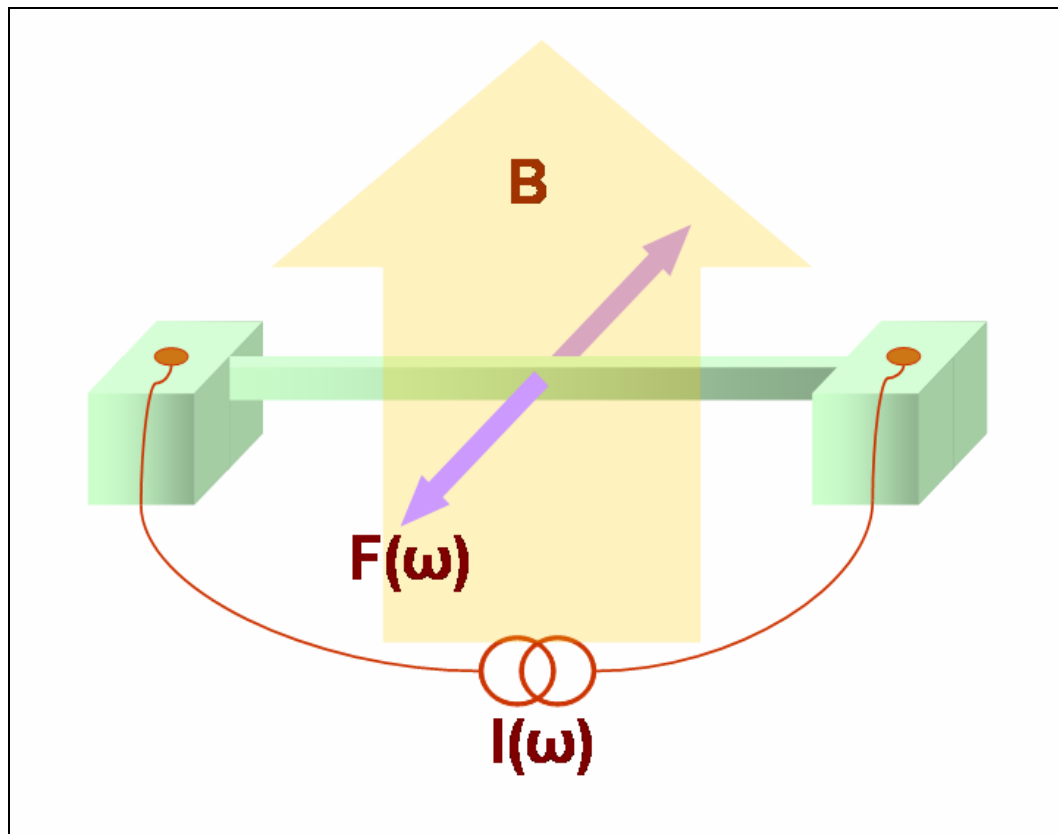

Figure 3.5: The schematic shows the magneto-motive actuation of a doubly clamped beam. In this figure, B is the strength of the static magnetic field and $I(\omega)$ is the alternating current passing through the beam. In accordance with the Lorentz formula, a force of $F(\omega) = LBI(\omega)$ is applied to the beam in the flexural axis.

Actuation is used to determine the frequencies of resonance modes and their quality factors experimentally. The magneto-motive actuation technique is compatible with high frequency applications and magneto-motive actuation at GHz frequencies has been realized experimentally [9].

In summary, nano-mechanical resonators, especially doubly clamped beams have unique mechanical properties such as high resonance frequencies and quality factors, which make them strong candidates for displacement measurements at quantum limit.

3.3 Motion Detection with NEMS

Displacement detection with the motivation of observing the quantum mechanical behavior of a resonator is a very challenging task. The zero-point fluctuation of a typical resonator with $m \approx 10^{-16}$ kg and $f_0 \approx 500$ MHz will be $x_{zp} \approx 30$ fm according to Equation 2.12. This rough calculation shows that the detector used in NEMS should be sensitive enough to detect the displacements on the order of femto-meters. Additionally, since the nano-mechanical resonators have microwave resonance frequencies, the sensor should also be able to operate at such high frequencies which requires a broad transduction bandwidth for the resonator [34]. In addition to these two requirements (sensitivity and speed), there is another important concept as *back-action* [28]. Back-action is the force/perturbation that the sensor applies on the mechanical resonator during motion detection. For a quantum mechanically ideal sensor, the back-action noise should approach to the limit set by the quantum mechanics as already discussed in the previous chapter.

There has been a great effort to realize a sensor that fulfils the severe requirements mentioned above. Many different state of art detection techniques based on different physical principles have been demonstrated by NEMS community [4, 6, 38-46]. Unfortunately, none of them has achieved displacement sensitivity at quantum limit or observed a signature of quantum mechanics. In the following subsections, two of the most outstanding detection techniques will be discussed with a special emphasize on their capabilities and limits.

3.3.1 Single Electron Transistor (SET)

Single electron transistor (SET) is widely used as a capacitive displacement transducer that couples the motion of the nano-resonator to the electronic sensor capacitively [38]. SET is a coulomb-blockade electrometer based on an intrinsically quantum mechanical phenomenon: quantum tunneling through a metal-insulator-metal junction. It consist of two tunnel junctions with an island between them and a gate electrode that is electrostatically coupled to the island as shown in Figure 3.6 [39].

In SET based displacement detection, the nano-resonator is capacitively coupled to the gate electrode of the SET and the capacitance between them is constantly modulated with the motion of the beam. When a constant gate voltage is applied to the beam, a charge of $Q = CV_{gate}$ is formed on the gate. Meanwhile, the amount of drain-source current I_{DS} depends on the potential of the island that is determined by the gate charge. Briefly, the fluctuations in gate charge due to the motion of the beam finally reveal itself in the detected drain-source current and thus the displacement of the beam can be inferred from this monitored current.
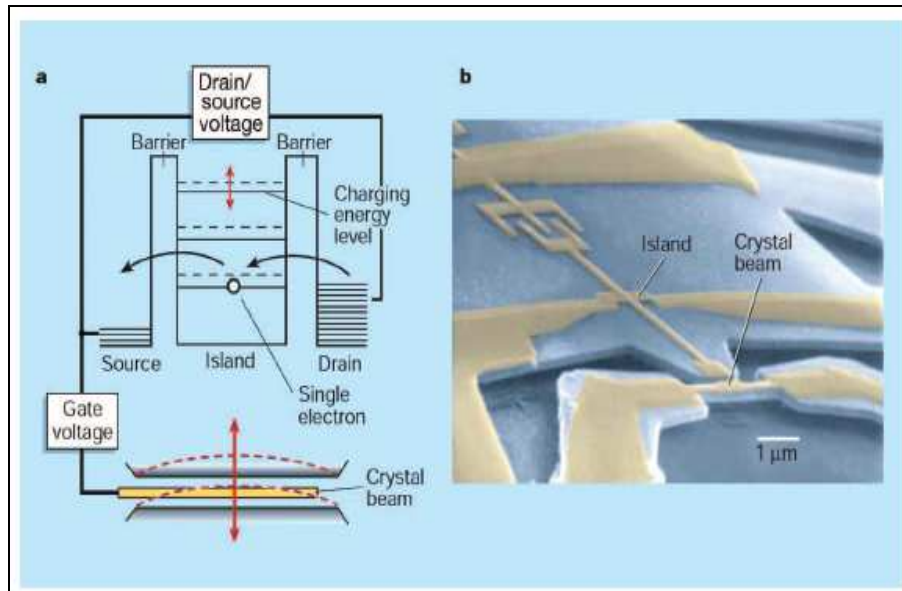
Figure 3.6: The schematic on the left shows the working principle of SET. The metalized nano-beam is coupled to the SET capacitively. The fluctuations in beam's position modulate the potential of the island which ultimately changes the drain-source current. Motion of the mechanical beam can be inferred from the changes in the drain-source current. The SEM image on the right shows the SET displacement sensor fabricated by Cleland's Group [40].

The main problem with the early SET displacement detectors was that they had a very small operation bandwidth due to the parasitic capacitances, which limits the sensor's sensitivity with 1/f noise. This problem has greatly been overcome with the invention of radio frequency SET (RF-SET) electrometer [41]. RF-SET electrometer was reported to have a charge sensitivity of 1.2×10^{-5} eHz$^{-1/2}$ at 1.1 MHz. With this invention, there has been an increase in the sensor speed from kHz frequencies to MHz range. In RF-SET, a method called "reflectometry" is used to increase the operation bandwidth of the sensor as illustrated in Figure 3.7 [41]. In this method, an LC transformer is placed at the output of the SET to transform the high output impedance of the SET to the characteristic impedance of the high frequency coaxial cables (50 Ω). The values of L and C are chosen such that they both match the SET resistance to 50 Ω and also increase the bandwidth of the operation as much as possible. Subsequently, a high frequency read-out circuit system follows the transformer to amplify and transmit the signal detected by the SET.
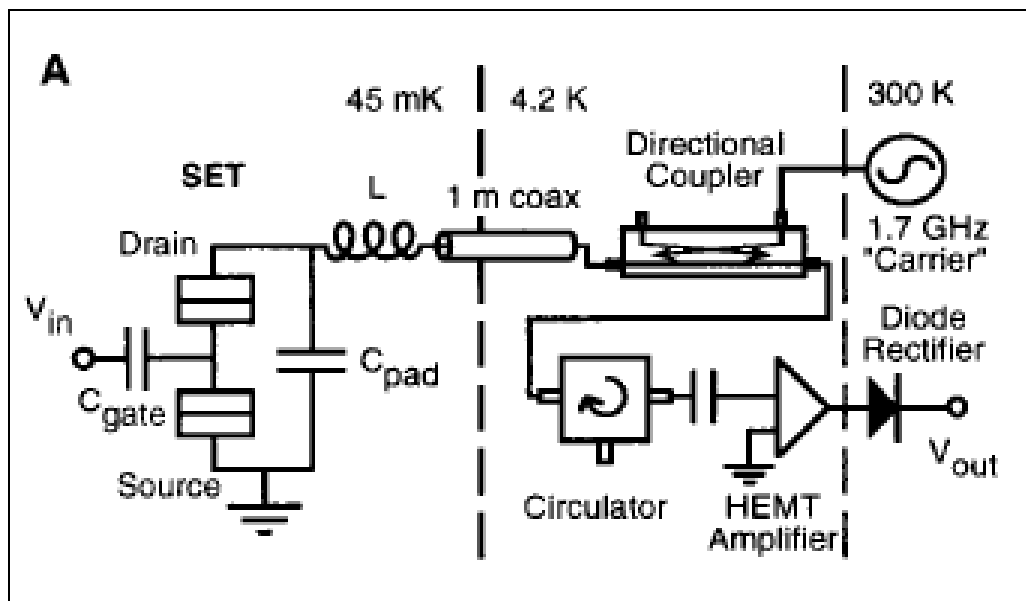

Figure 3.7: The RF-SET reflectometry system was first developed by the Schoelkopf and his group [41]. The LC transformer reduces the intrinsic high output impedance of the SET to the impedance of the coaxial cable. This transformer not only eliminates the 1/f noise by impedance matching but also increases the operation bandwidth of the sensor.

The reflectometry technique has been applied to SET displacement detectors by many different groups to increase the speed of the measurement. The best sensitivity achieved until today was reported by Schwab's group that is 4.3 times the quantum limit [42]. In this work, they measured the displacement of a doubly clamped beam resonating with 19.7 MHz at 56 mK with a sensitivity of $3.8\,\mathrm{fmHz}^{-1/2}$. Even though their sensitivity was very close to the standard quantum limit of the resonator under test, they could not observe any signatures of quantum mechanics. The main reason for that is their high thermal occupation number $N_{th} = 58$. As already discussed in the previous chapter, a thermal occupation number that is close to unity is needed for a resonator to enter the quantum realm. Another important experimental result with a lower thermal occupation number was reported by Cleland's group [40]. They have measured the motion of a doubly clamped with a resonance frequency of 116 MHz at 30 mK corresponding to a thermal occupation number around 30. Their thermal occupation number was lower than the Schwab's. On the other hand, their sensitivity is roughly a hundred times the standard quantum limit and they also could not observe any quantum mechanical behavior.

Despite this outstanding results, good enough displacement sensitivity with low enough thermal occupation number to detect the mechanical quanta of a nano-resonator have not been achieved with SET. Recent theoretical analyses also show that the sensitivity of the SET based motion detection, approaches but cannot reach the quantum limit [38]. The main obstacle for SET reaching the quantum limit is the back-action of the sensor on the beam [38]. As a result of the stochastic nature of the electrons, the voltage on the island fluctuates as the electrons hop on and off the island. These voltage fluctuations exert a force on the resonator, which is called as the back-action. In Reference 38, it is rigorously calculated that the back-action noise of a SET is larger than the minimum allowed by the quantum mechanics and thus theoretically SET cannot operate at ultimate quantum limit.

3.3.2 Optical Interferometry

Motion detection with optical interferometry has widely been used in MEMS and has recently been extended to NEMS [35, 44, 45]. The most common methods are path-stabilized Fabry-Perot interferometry and Michelson interferometry that are depicted in Figure 3.8 [46].
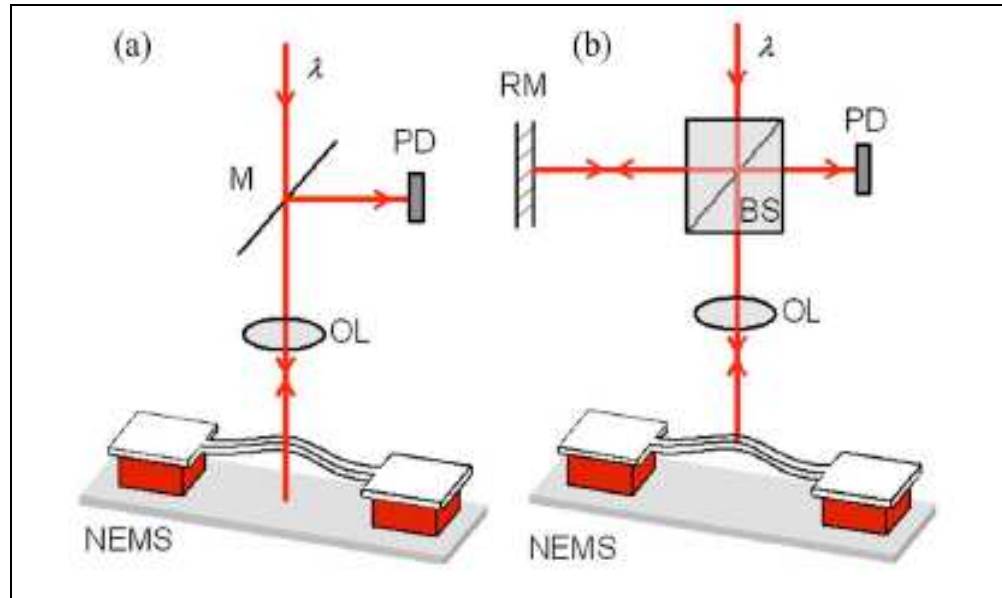

Figure 3.8: The figure on the left shows a Fabry-Perot interferometer and the figure on the right shows a Michelson interferometer both coupled to a nano doubly clamped beam. In both schemes, a light beam with wavelength λ is sent to the mid-point of the mechanical beam with the help of an object lens (OL). The light that is reflected back from the resonator is detected with a photo-detector (PD) [46].

In path stabilized Fabry-Perot interferometer, an optical cavity is formed between the resonator and the sacrificial layer to act as an object lens [28]. This optical cavity aligns the laser beam on the mid-point of the resonator. The reflected optical signal received by a photo-detector is modulates as the resonator moves. In the case of the Michelson interferometer, the laser beam reflected back from the resonator is interfered with a reference beam and sent to the photo-detector. The advantages of these optical techniques are they can work at room temperature; the very-wide operation bandwidth of photo-detectors enables ultra-fast displacement detection; and they are nondestructive [47]. A sensitivity of $1\,\text{pmHz}^{-1/2}$ has been reported for a doubly clamped beam with a resonance frequency of 20 MHz [48].

Even though the back-action caused by the measurement process on the resonator is quantum limited, the displacement sensitivity of optical methods is limited by another physical phenomenon, diffraction [49]. In optical methods, the resolution of the measurement is determined by the spot size of the beam and the spot-size of the tightly focused beam has a lower bound determined by the diffraction. This diffraction effects becomes important when the device size becomes smaller than the wavelength of the optical beam, which is the case in NEMS [34]. All in all, it is impossible to measure the small fluctuations of a nano-resonator with an optical beam whose spot size is larger than the width of the beam. For this reason, despite its advantages, optical methods are not compatible with nano-sized application.
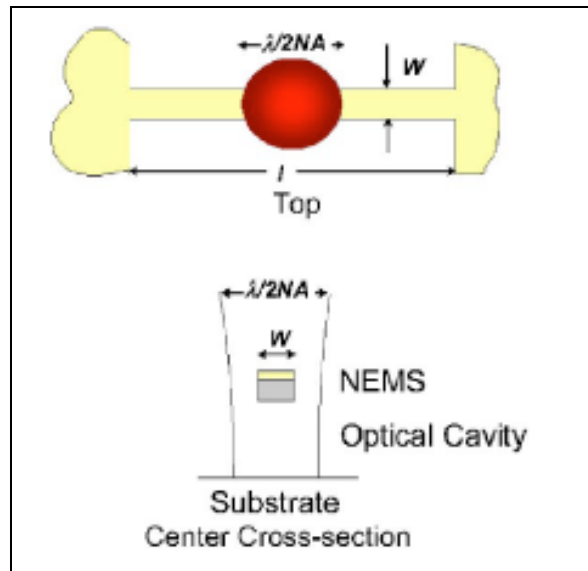

Figure 3.9: The illustrations show the relation between the spot size of the optical beam and the size of the nano-mechanical resonator [34]. The spot size of the optical beam is ultimately limited by diffraction and at nano-scales, the spot size becomes larger than the dimensions of the resonator.

CHAPTER 4

VACUUM TUNNELING DISPLACEMENT SENSOR

As discussed in the previous chapter, many different outstanding detection techniques have been developed to measure the displacement of a nano-mechanical resonator [4, 6, 38-46]. All of them have been fabricated and tested with state of the art technology. Parallel to the experimental developments, there has also been an intensive theoretical investigation on the fundamental limits of these sensors [21, 24, 25, and 38]. Despite this great effort, present sensors approach but do not reach the quantum limit either due to excess back-action or due to other physical limit. In other words, none of them could detect a quantum-mechanical behavior of a nano-mechanical resonator, which is the primary motivation of these experiments. As a consequence, researchers have started to search for new sensors that will be capable of displacement detection at ultimate quantum limit. A displacement sensor based on the detection of the current through a tunnel junction is one of the most promising candidates. It was first proposed by the gravitational wave-antenna community for the detection of very weak gravitational forces that act upon a gravitational wave-antenna [1]. Since the theoretical analyses regarding vacuum tunneling displacement sensor predict a sensitivity at quantum limit, it has taken serious attention of NEMS community recently but it has not been able to be realized due to some challenging engineering problems yet. This chapter starts with an introduction to the tunneling, which is a quantum mechanical phenomenon. It will be followed by a complete discussion on the sensitivity limits and noise properties of a vacuum tunneling displacement sensor. Finally, the difficulties regarding the fabrication of this particular sensor will be addressed with possible solution proposals.

4.1 Introduction to Vacuum Tunneling

Tunneling is a quantum mechanical phenomenon. In classical mechanics, a particle cannot overcome a potential barrier that is larger than its total energy. On the other hand, in quantum mechanics there is a certain probability for the particle to pass through the barrier even though its total energy is smaller than the potential of the barrier [50]. Therefore, quantum mechanically, it is possible for an electron to transport between two metallic electrodes that are separated by a thin, high-potential barrier like an insulating film or vacuum. Likewise, a tunneling current will start to flow when a bias voltage is applied between the electrodes. The amount of this tunneling current depends exponentially on the thickness of the potential barrier, that is to say the distance between the metal electrodes. For low bias voltages, the equation of the current density between two electrodes of the same material is formulated by Simmons as [51]

$$J = \frac{3\sqrt{2m_e\phi}}{2s}\left(\frac{e}{h}\right)^2 V \exp\left(-\frac{4\pi\sqrt{2m\phi}}{h}s\right). \tag{4.1}$$

In this equation m_e is the mass and e is the charge of the electron, h is Planck's constant, ϕ is the work function of the metal, V is the applied voltage and s is the distance between the electrodes. If the fundamental constants are inserted in with practical units, the Equation 4.1 becomes

$$J = 3.16\times10^{10}\sqrt{\phi}\,\frac{V}{s}\exp\left(-1.025\sqrt{\phi}s\right), \tag{4.2}$$

where J is in A/cm^2, ϕ and V are in volts, and s is in Ångstrom. The Equation 4.2 shows that, for constant bias voltages, the current density has an exponential dependence on the thickness of the potential barrier. This implies that the tunneling current varies dramatically with the changes in the tunnel gap. In order to have a deeper insight into the sensitivity of the tunneling current to the fluctuations in the tunnel gap, think of two gold electrodes separated by a vacuum tunnel junction. The work function of gold has experimentally been measured as $\phi \approx 4.8eV$ [52]. Using these values, the tunneling current density versus tunneling gap is obtained as shown in Figure 4.1.
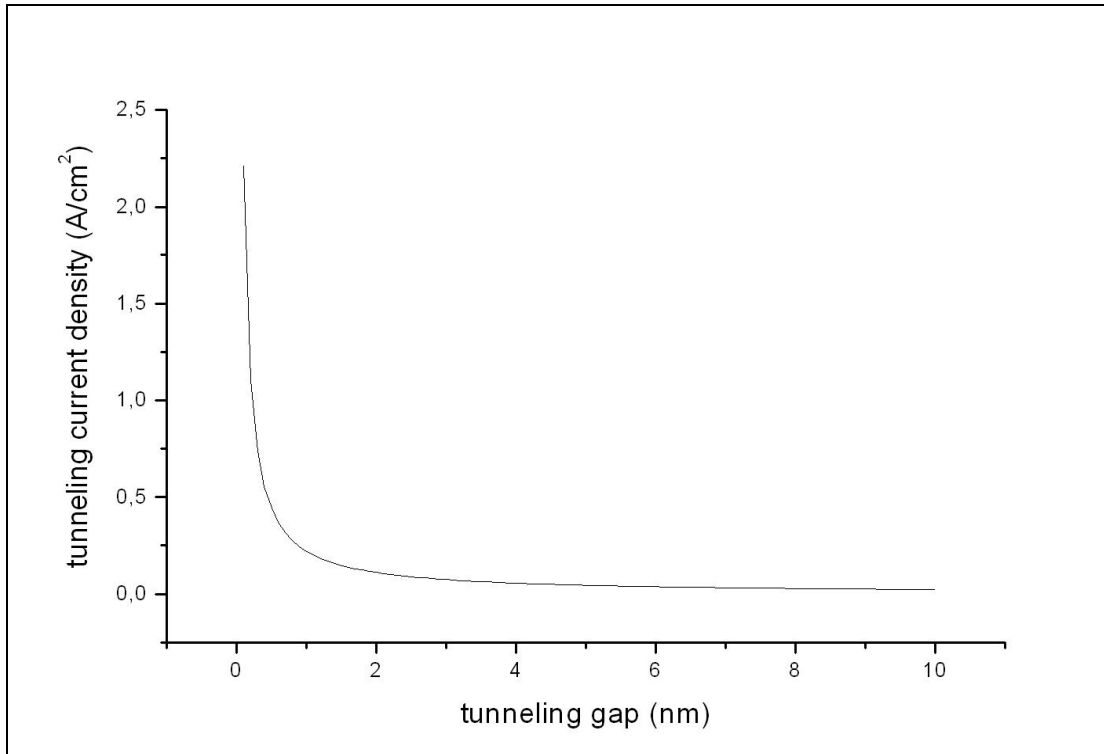
Figure 4.1: Dependence of tunneling current density on the gap distance is given for two gold electrodes under a bias voltage of 100 mV. The responsivity of the tunneling current density to the fluctuations in the tunneling gap is proportional to the steepness of the graph.

In this graph, it is obvious that the tunneling current density changes much faster for smaller values of tunneling gap. Actually, the responsivity of the tunneling current density to the fluctuations in the tunneling gap is proportional to the steepness of the graph. However, the tunneling gap cannot be made arbitrarily small due to the fact that for extremely small values of the gap, the junction leaves the tunneling regime and forms a quantum point contact. Accordingly, there is an optimum value for the tunneling gap that is typically around 1 nm. The amount of the tunneling current can be found by multiplying the current density with the cross-sectional area of the tunnel junction. Taking a typical cross-section around 10^{-10} cm^2, the tunneling current will be around $I_T \approx 1\,\text{nA}$ for $V \approx 100\,\text{mV}$ which indicates an effective tunneling resistance of $10^8\,\Omega$. Additionally, the same equation shows that very small fluctuations in the gap distance such as $\Delta s \approx 10^{-15}\,\text{m}$, results in considerable changes in the tunneling current like $\Delta I_T \approx 10^{-13} - 10^{-14}\,\text{A}$.

The most well known application of quantum tunneling phenomenon in experimental physics is the Scanning Tunneling Microscope (STM). STM was invited by Binnig and Rohrer in 1981 and has been a very powerful tool in surface science because it provides a spatial atomic resolution of the conducting/semiconducting surfaces [53]. STM consists of an atomically sharp tunnel tip that is placed within a few nanometers of the surface of a sample such that a tunnel junction is formed between the tip and the sample. A bias voltage is applied to the tunnel junction to form a tunnel current and meanwhile the tip scans the surface either at constant-height or constant-current mode and determines the topology of the surface at atomic-size sensitivity. The working principle of STM is shown in Figure 4.2.
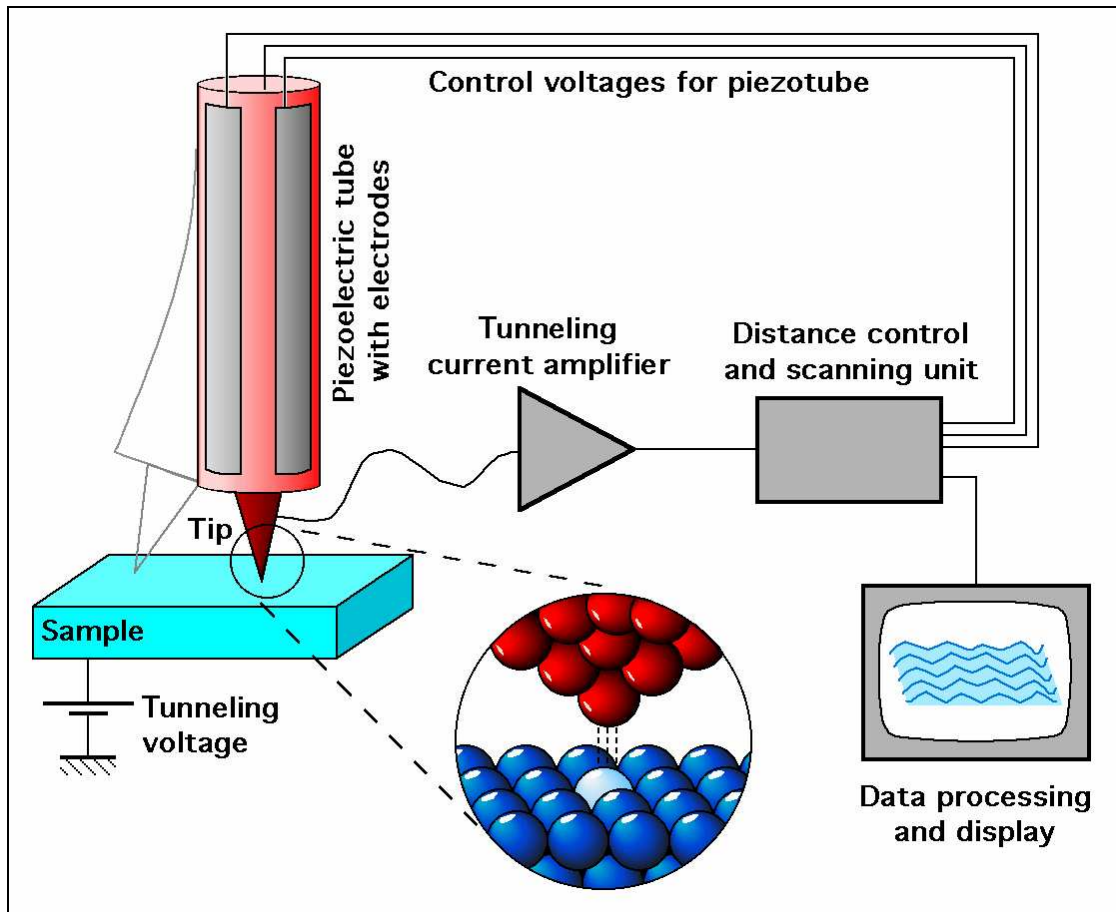

Figure 4.2: The General working principle of STM is shown (graphics by Michael Schmid, TU Wien)

4.2 Theoretical Analyses of Vacuum Tunneling Displacement Sensor

A displacement sensor based on the detection of vacuum tunnel current was first proposed two decades before by the gravitational wave community shortly after the invention of STM [54-59]. As previously mentioned in Chapter 2, the aim of gravitational wave antennas is to detect the very-weak gravitational forces act upon the Earth by distant stars and planets [54]. The gravitational wave antennas are modeled as harmonic oscillators actuated by weak gravitational forces. Therefore, the gravitational field researchers have intensively focused on the discussion of ultra-sensitive measurement of a mechanical resonator's displacement to infer the force applied on it. Taking inspiration from STM, a sensor named *vacuum tunnel transducer* was proposed for displacement detection [54]. In the following years, the proposed displacement sensor, its sensitivity and noise characteristics are analyzed rigorously [55-61].

The vacuum tunnel transducer (displacement sensor) is modeled as a stable metal tip that is coupled to a mechanical resonator via a tunnel junction. If a bias voltage of V_0 is applied across the tip and the resonator, a tunneling current starts to flow [56]

$$I = I_0 \exp(2\kappa x),\tag{4.3}$$

where,

$$\kappa = \sqrt{2m_e \phi}\big/\hbar .\tag{4.4}$$

Here, I_0 is the tunnel current when the gap separation is equal to so-called nominal gap d, and x is the deviation from the nominal gap. In accordance with, the tunnel junction can be modeled as a resistor with a resistance of

$$R = \left(V_0/I\right) = R_0 \exp(-2kx),\tag{4.5}$$

where $R_0 = V_0/I_0$ is the nominal resistance and is generally around $10^8 \Omega$ when $d \approx 1\,\text{nm}$ [58].
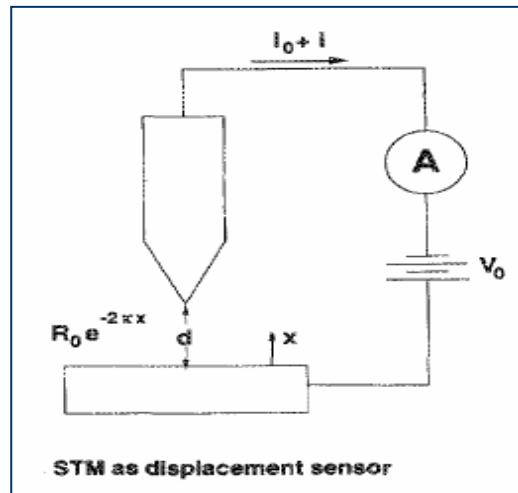
STM as displacement sensor

Figure 4.3: The application of the vacuum tunnel transducer as displacement sensor [56]. The tunnel junction can be modeled as a resistor that depends exponentially on the tunnel gap. The gap distance between the tip and the mechanical resonator fluctuates around its nominal value d as the resonator moves. The fluctuations in the gap are given by the displacement of the resonator x.

For the sensitivity analysis of the vacuum tunnel junction, the electrical equivalent of the transducer and the succeeding amplifier are shown in Figure 4.4 with the accompanying noises [55]. In this electrical model, the parallel connected R and C represent the tunneling resistance and tunnel junction capacitance respectively. The fluctuation in the tunneling gap as a result of the mechanical resonator's motion, which is the apparent motion, is depicted as a voltage noise source connected to the tunneling resistance in series
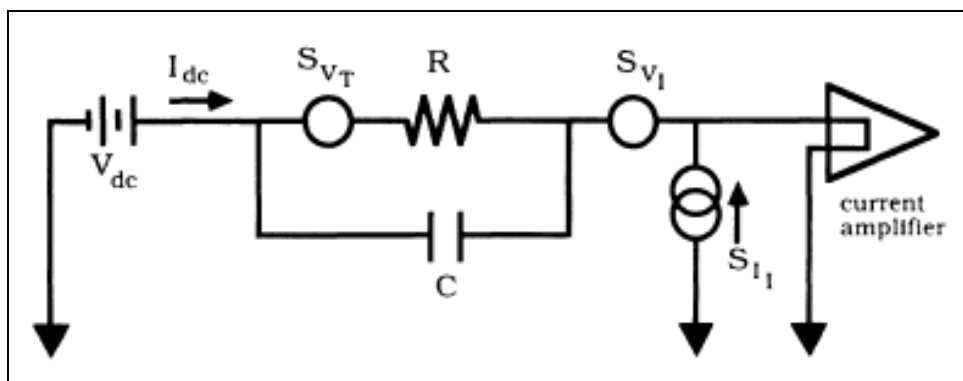
$$S_{V_T} = 2eI_0R^2.$$
(4.6)

Figure 4.4: The electrical modeling of vacuum tunneling transducer and the succeeding current amplifier are shown with the accompanying noise sources [55].

44

The noise contribution from the current amplifier connected to the end of the tunnel junction is included with a serial voltage noise source S_{V_I} and a parallel current noise source S_{I_I}.

There are basically three sources of noise that limits the sensitivity of the tunneling transducer [55]. These are the apparent fluctuations in the tunneling current, the back-action force of the tunneling transducer on the resonator and finally the thermal Brownian motion. To begin with, the noise power spectrum of the fluctuations in the tunneling gap is given by [55]

$$S_{x_{apparent}} = \frac{1}{4\kappa^2 I_0^2}\left(S_{I_I} + \frac{S_{v_I}}{R^2}\left(1 + \omega_0^2 R^2 C^2\right) + \frac{S_{v_T}}{R^2}\right), \qquad (4.7)$$

where ω_0 is the vibration frequency of the mechanical resonator. From Equation 4.7 the actual variances in the position can be calculated using:

$$x_{apparent} = \sqrt{S_{x_{apparent}}\big/\left(\tau_{meas}/2\right)}, \qquad (4.8)$$

where τ_{meas} is the measurement time, which is assumed to be much smaller than the oscillator's relaxation time.

In addition to the apparent displacement fluctuations, there is a second noise contribution called as *back-action* [28]. Every time an electron jumps from the tip to the sample or vice versa, an impulse force is applied on the resonator due to momentum transfer and causes further fluctuations in the position of the resonator. The amount of momentum transfer is stochastic due to the fact that both the amount of charge transfer per unit time and also the amount of the momentum carried by each electron have a probabilistic distribution according to quantum mechanics. In addition to momentum back-action, there is also a capacitive back-action force due to the fluctuations in the amount of the charge on the tunnel capacitance as the mechanical resonator vibrates. The power spectral density of the fluctuating back-action force and the corresponding fluctuations in the displacement are given by [55]

$$S_{F_{BA}} = \left(\frac{p}{e}\right)^2 \left(\frac{S_{V_T} + S_{V_I}}{R^2}\right) + C^2 E^2 S_{V_T} \,, \tag{4.9}$$

$$x_{ba} = \frac{\sqrt{S_{F_{BA}}}}{m\omega_0} \left(\tau_{meas}/2\right)^{1/2} . \tag{4.10}$$

In these equations p is the average momentum carried by each electron, E is the electric field across the tunnel junction, m and ω_0 are the mass and frequency of the oscillator respectively.

Last but not least, there is a noise contribution from the thermal fluctuations of the mechanical resonator, which is called as the *Brownian motion*. The fluctuations in the position of the resonator due to Brownian motion is given by [62]

$$x_{BM} = \sqrt{\frac{k_B T \tau_{meas}}{m\omega_0 Q}} \,, \tag{4.11}$$

where k_B is the Boltzman's constant, T is the temperature in Kelvin, and Q is the quality factor of the mechanical resonator.

The total fluctuations in the displacement can be calculated by adding all three-noise sources given by the equations 4.8, 4.10, and 4.11

$$x_{noise} = x_{apparent} + x_{ba} + x_{BM} . \tag{4.12}$$

The minimum uncertainty in the displacement or in other words maximum sensitivity of the measurement can be found by minimizing the Equation 4.12 with respect to the measurement time, τ_{meas}

$$x_{min} = 2\left\{\left(\sqrt{\frac{kT}{m\omega_0 Q}} + \sqrt{\frac{S_{F_{BA}}}{2m^2\omega_0^2}}\right) \times \sqrt{2S_{x_{apperant}}}\right\}^{1/2} . \tag{4.13}$$

Equation 4.13 gives us the expression for the measurement sensitivity of a vacuum tunnel transducer that monitors the motion of a mechanical resonator. For the numerical evaluation of this equation, some typical values found in the literature are shown in Table 4.1 [28, 34, 55-61]

Nominal (DC) Tunneling Current	$I_0 = 1\,\text{nA}$
Nominal Tunneling Resistance	$R_0 = 100\,\text{M}\Omega$
Electric Field in the Tunnel Junction	$E = 10^9\,\text{V/m}$
Capacitance of the Tunnel Junction	$C = 1\,\text{aF}$
Applied (Bias) Voltage	$V_0 = 100\,\text{mV}$
Fermi Momentum	$p = \hbar k_F = 1.4 \times 10^{-24}\,\text{kgms}^{-1}$
Current Amplifier's Voltage Noise Spectra	$S_{V_I} = 1.4 \times 10^{-21}\,\text{V}^2\text{Hz}^{-1}$
Current Amplifier's Current Noise Spectra	$S_{I_I} = 3.2 \times 10^{-28}\,\text{A}^2\text{Hz}^{-1}$

Table 4.1: The typical values from literature for the terms related to the tunnel junction and succeeding amplifier are provided [28, 34, 55-61].

Additionally, for the parameters regarding the mechanical resonator, results of a recent experiment are adopted [40]

Temperature	$T = 30\,\text{mK}$
Dimensions of the Resonator	$l \times w \times t = 3\,\mu\text{m} \times 250\,\text{nm} \times 200\,\text{nm}$
Mass of the Resonator	$m = 2.84 \times 10^{-15}\,\text{kg}$
Resonance Frequency of the Resonator	$f_0 = \omega_0/2\pi = 116.7\,\text{MHz}$
Quality Factor of the Resonator	$Q = 1700$

Table 4.2: The experimentally observed values for a nano-mechanical resonator's mechanical properties are given [40].

When all the values given in Table 4.1 and Table 4.2 are inserted in Equation 4.13, the displacement sensitivity of the vacuum tunnel transducer is found to be approximately 500 fm, which is very sensitive but quite larger than the standard quantum limit of the given resonator that is around 5 fm. There are three main reasons for the noise in excess of hundred times the standard quantum limit:

1. The most dominant factor in the redundant fluctuations of the displacement is the thermal Brownian motion. In fact, if the noise contributions of the thermal fluctuations: $\sqrt{k_B T / m \omega_0 Q}$ and the back-action force: $\sqrt{S_f / 2m^2 \omega_0^2}$ are compared in Equation 4.13, it is found that the thermal fluctuation is 50 times larger than the fluctuations caused by back-action force. Therefore, thermal fluctuations are responsible for more than an order of magnitude excess noise in displacement detection. On the other hand, as discussed in Chapter 2, the sensitivity of a sensor is identified with the noise it adds to the apparent fluctuations (thermal fluctuations, zero-point motion) of the nano-resonator. In other words, while determining the sensitivity of a transducer, only the noises originating from the transducer should be included. Therefore, the noise spectra of thermal fluctuations should be subtracted from Equation 4.13.

2. In this model, there are two contributions to the back-action force; one from the momentum current fluctuations and the other from the fluctuating amount of charge on the capacitor. It has later been showed in another work [56] that the capacitive back action fluctuations can be ignored when the capacitance satisfies the following condition

$$C << \frac{m \omega_0^2 d^2}{V_0^2} .$$
(4.14)

Using the values given in Table 4.1 and Table 4.2 and taking the gap separation $d \approx 1 \, \text{nm}$, Equation 4.14 becomes

$$C << 1{,}5 \times 10^{-13} \, \text{F} .$$
(4.15)

The capacitances of tunnel junctions are reported [63] to be on the order of $10^{-17} - 10^{-18}$ F, which definitely satisfies the above condition and hence the contribution of the capacitive force to the back-action noise can be ignored safely.

3. The Equation 4.13 includes the voltage and current noises of the amplifier following the tunneling sensor. However, the main advantage of the tunneling transducer over the conventional transducers is that the shot noise of the tunnel junction dominates the noises of the trans-impedance amplifier and as a result the sensitivity of the sensor is limited by the sensor's shot noise but not by the succeeding amplifier and electronic circuit. Shortly, for the vacuum tunneling transducer the noise contributions of the amplifier S_{V_I} and S_{I_I} can be ignored. The validity of this simplification has been proved by Bocko et. al. using a two-port network model [58]. In this model, the tunneling transducer and the following current amplifier are considered as two cascaded two-port networks as shown in Figure 4.5.
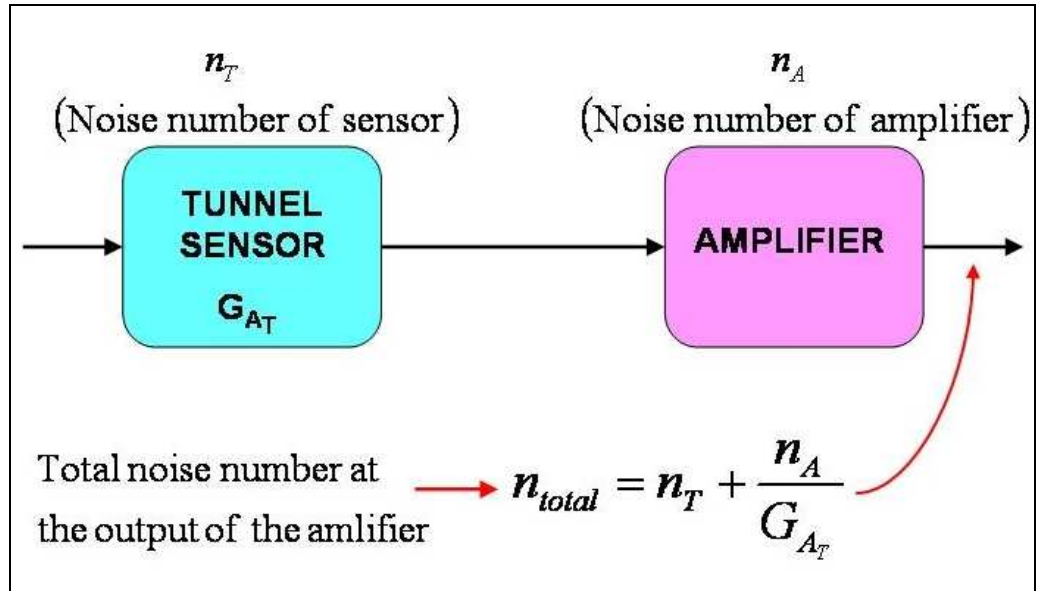

Figure 4.5: Cascaded two-port network model for the tunnel sensor and the following amplifier. The influence of the amplifier on the total noise number is diminished by the high gain of the tunnel sensor. The sensitivity of the tunnel sensor is independent of the following amplifier's noise.

The noise number of a device is defined as the number of mechanical quanta that will be deposited on the harmonic oscillator with the minimum detectable impulse force and given with the formula

$$n = \frac{k_B T_n}{\hbar \omega_0} , \tag{4.16}$$

where T_n is the noise temperature of the device and ω_0 is the resonance frequency of the mechanical oscillator. As mentioned in Chapter 2, the minimum noise added by an ideal linear amplifier will be half of the mechanical quanta [12, 13]. Therefore, assuming that the tunneling sensor is a quantum mechanically ideal amplifier, then the minimum noise number it can have is $n_T = 1/2$. Later , it will be show that this is actually true for the tunneling sensors. On the other hand, the noise temperature of a HEMT amplifier is around $1\,\text{K}$ which yields a noise number of $n_A \approx 180$. Additionally, the available power gain of the tunneling transducer on resonance is given by the equation [57]

$$G_{A_T} = \frac{4\kappa^2 I_0 V_0 Q}{m \omega_0^3} . \tag{4.17}$$

The available power gain of the tunneling transducer is found to be around 600 for the given parameters in Tables 4.1 and 4.2. Consequently the noise contribution from the amplifier is $n_A / G_{A_T} \approx 0.3$, which is smaller than the minimum noise number the tunneling sensor can have. Concisely, the noise of the tunneling transducer overwhelms the noise of the amplifier and hence one can ignore the noise terms related to the amplifier such as S_{V_I} and S_{I_I} in equation 4.13. Furthermore, recall that high power gain is one of the criteria required in Chapter 2 for a quantum ideal linear amplifier [13].

Overall, the three corrections mentioned above must be done in the original model. The thermal fluctuations, capacitive back-action force and the amplifier related noises should be excluded from Equation 4.13. As a result, only the shot noise which is the fluctuations in the tunnel current and the back-action due to the fluctuations in the imparted momentum on the resonator are left. First of all, the shot noise current power density is simply given by the equation [28]

$$S_{I_S} = 2eI_0. \qquad (4.18)$$

On the other hand, for the back-action force a more detailed treatment is necessary. There are many theoretical works regarding the back action force due to electron tunneling [23, 55-60]. The back-action force exerted on the resonator due to electron tunneling can be given as the total momentum transfer per unit time [56]

$$F_{BA} = p\frac{I}{e}, \qquad (4.19)$$

where, p is the momentum of a single electron and I is the tunnel current. Both of them fluctuates over a mean value such that

$$\begin{aligned} p &= p_0 + \Delta p \\ I &= I_0 + \Delta I \end{aligned}. \qquad (4.20)$$

If we ignore the second order term, the fluctuations in the back-action force becomes

$$\Delta F_{BA} = \frac{1}{e}\{p_0\Delta I + I_0\Delta p\}. \qquad (4.21)$$

The corresponding power spectral density of the back-action force is given by

$$S_{F_{BA}} = \left(\frac{p_0}{e}\right)^2 S_{i_S} + \left(\frac{I_0}{e}\right)^2 S_p, \qquad (4.22)$$

where $S_{i_s} = 2eI_0$ is the shot noise spectral density and S_p is the power spectra of the momentum fluctuations. The first term in Equation 4.21 is the back-action force fluctuations due to the fluctuations in the tunneling current, which is directly correlated to the shot noise. However, as pointed in Chapter 2, only the uncorrelated noises should be added while determining the fundamental limit of a sensor. That is to say, the part of the back-action force that results from the tunneling current fluctuations is already included in the shot noise. The second term in the back-action force equation represents the fluctuations due to the uncertainty in the momentum of a single electron that is totally uncorrelated with the shot noise and hence a fundamental limit. In brief, in order to determine the noise limit of the tunnel transducer we are interested in the tunnel current shot noise and the momentum uncertainty of a single tunneling electron that are totally uncorrelated.

The momentum dispersion of tunneling electrons is rigorously determined by Yurke and Kochanski with an entirely quantum mechanical approach [56]. They have calculated the variances in position and momentum for a rectangular barrier of width d where the resonator and the tip are made of same material with potential V and the rectangular barrier's potential is taken to be V_b. They found the uncertainties of the position and the momentum [57]

$$\Delta l = \frac{|D(k)|^2}{4\sqrt{n}kk_b^2(k^2 + k_b^2)\cosh(k_b d)}, \tag{4.23}$$

$$\Delta p = \frac{2\sqrt{n}\hbar kk_b^2(k^2 + k_b^2)\cosh(k_b d)}{|D(k)|^2}, \tag{4.24}$$

where $k = \sqrt{2m(E-V)}/\hbar$, $k_b = \sqrt{2m(V_b - E)}/\hbar$ and n is the number of electrons that tunnel through the barrier in the measurement time τ. Finally, the equation for $D(k)$ is given by [57]

$$D(k) = 2kk_b \cosh(k_b d) - i(k_b^2 - k^2)\sinh(k_b d). \tag{4.25}$$

From Equations 4.23 and 4.24, it is immediately seen that the position and the momentum uncertainties satisfy the equality of the uncertainty principle

$$\Delta l \Delta p = \hbar/2 \,. \tag{4.26}$$

This shows that the tunneling sensor is intrinsically a quantum-limited sensor. In this analysis Δl is calculated from the fluctuations in the number of particles passing through the tunnel barrier that is to say the variances in the tunnel current. Therefore, the product of two completely uncorrelated noise sources of tunneling sensor, shot noise and momentum back-action, satisfy the ideal noise condition of Heisenberg's Uncertainty Principle. This was one of the criteria described in Chapter 2 with Equation 2.51 that a displacement sensor must meet in order to be able to perform measurements at ultimate quantum limit.

The spectral density of momentum fluctuations can be calculated using the results of Yurke and Kochanski. In our case, the potential barrier is vacuum and thus the potential of the barrier V_b is very high compared to the potential of the electrodes, meaning $k_b \gg k$. Also, when V_b is the potential of the vacuum than k_b reduces to term κ

$$k_b = \frac{\sqrt{2m(V_b - E)}}{\hbar} = \frac{\sqrt{2m\phi}}{\hbar} = \kappa \,, \tag{4.27}$$

and it has been previously shown that for a typical tunnel junction $\kappa \times d \approx 10$ which is much larger than unity. Using the assumptions of $k_b \gg k$ and $\kappa d \gg 1$ in Equation 4.23, one gets

$$\Delta p \approx \sqrt{n}(\hbar\kappa) \,. \tag{4.28}$$

Using Equation 4.28 the power spectral density momentum uncertainty, S_p is calculated as [28]

$$S_p = \frac{e}{I_0}(\hbar\kappa)^2 . \tag{4.29}$$

If we insert the expressions for shot noise and momentum fluctuation spectral density in Equation 4.22, the noise power spectral density of fluctuating total back action force

$$S_{F_{BA}} = \left(\frac{p_0}{e}\right)^2 2eI_0 + (\hbar\kappa)^2 \frac{I_0}{e} . \tag{4.30}$$

Using all the corrections mentioned above we can recalculate the Equation 4.13 to determine the minimum displacement sensitivity of the tunnel sensor. Recall that, we will exclude the thermal fluctuations which corresponds to the first term in Equation 4.13 and will recalculate S_f and $S_{x_{apparent}}$. First of all, to find out the worst case for $S_{x_{apparent}}$, we will keep the purely additive current noise from the following amplifier S_{I_I}, despite the fact that the amplifier noise is mostly overwhelmed by the tunnel current shot noise as a result of its high power gain. Thus, the final expression of $S_{x_{apparent}}$ is

$$S_{x_{apparent}} = \frac{1}{4\kappa^2 I_0^2}\left(S_{I_I} + 2eI_0\right). \tag{4.31}$$

This equation gives us $S_{x_{apparent}} \approx 1.3\times10^{-30} \text{ m}^2\text{Hz}^{-1}$ for the given parameters in Table 4.1. Secondly, for the back-action force noise spectrum we will use the final expression given in Equation 4.30. The resulting back-action force for the same parameters is $S_{F_{BA}} \approx 2.5\times10^{-38} \text{ N}^2\text{Hz}^{-1}$. The minimum displacement sensitivity given in Equation 4.13 is modified accordingly

$$x_{min} = 2\left\{\sqrt{\frac{S_{F_{BA}}}{m^2\omega_0^2}} \times \sqrt{S_{x_{apperant}}}\right\}^{\frac{1}{2}} . \tag{4.32}$$

The equation above gives a displacement resolution of 18 fm, which is just 3.6 times the zero-point fluctuation, for the resonator $m = 2.84 \times 10^{-15} \, \text{kg}$ and $\omega_0 = 2\pi \times 116.7 \, \text{MHz}$ of the resonator. Recall that we consider the worst case, which includes the non-fundamental limits like the amplifier current noise and the average momentum of the tunneling electron that is assumed to be the Fermi momentum. If these non-fundamental limits are subtracted from the apparent displacement and back action force, the sensitivity would be just around two times the zero-point fluctuations.

To sum up, starting with a classical noise model for the tunneling sensor which includes all kinds of noises [55], we have subtracted the non-fundamental noises and employ a more rigorous expression for the back-action. Finally, we ended up with the fundamental sensitivity of a vacuum tunneling displacement sensor, which is turned out to be very close to the zero-point fluctuations of the resonator. The main advantage of the tunnel transducer to capacitive transducers like SET is the reduced back-action force.

4.3 Experimental Aspects of Vacuum Tunneling Displacement Sensor

Despite the fact that the theoretical analyses of vacuum tunneling transducer are very promising, it has not been experimentally realized yet due to serious engineering problems. First, the formation of the tunnel junction is problematic in NEMS. In STM, the most well known application of the quantum tunneling, the tunneling tip is approached to the surface of the material with a high-precision positioning mechanism consisting of piezoelectric tubes that control the height of the system and scan the tip over the surface. These piezoelectric tubes are connected to macroscopic electronic circuits and a feedback system that make STM a bulky instrument. This bulk structure of the STM reduces its mechanical resonance and hence the measurement speed. Furthermore, the mechanical vibrations of the STM reduce the stability of the tip position to pico-meter range, which is larger than the femto-meter range displacements to be measured. In short, STM mechanism is not applicable to NEMS and such a positioning mechanism cannot be used to place a metal tip near a nano-mechanical resonator. Besides, even with such a high-precision positioning mechanism, it would be very difficult to align the tip to the mid-point of the nano-mechanical resonator due to

its extremely small dimensions. Consequently, a stable metal tip and the mechanical resonator should be fused together in such a way that a vacuum tunnel junction is formed between them. The fabrication of the nano-beam and the metal tip in a compact form is the most difficult part of the vacuum tunneling displacement detection experiment. Remember that the sensitivity of the tunneling sensor is predominantly determined by the coupling strength between the resonator and the sensor, which indeed depends on the tunneling distance. For the highest sensitivity, there is an optimum gap distance and hence it is necessary to be able to fabricate tunnel junctions at predetermined widths. In the next chapter, which is the experimental part of the thesis, a method will be introduced to fabricate such tunnel junctions in a controlled-manner.

In addition to the fabrication of the mechanical beam and the vacuum tunnel sensor as a compact nano-system, there is another technical problem to be solved regarding the operation speed. The tunneling is intrinsically a quantum mechanical phenomenon which makes it very fast [64]. The intrinsic speed of quantum tunneling can be inferred from the number of tunneling electrons per unit time, I/e which entails an operation bandwidth of 1 GHz when the tunneling current is around 1 nA. However, this intrinsic high speed of quantum tunneling is dropped off to kHz range in experiments. This immense decrease in the measurement speed is due to large RC time constant as a result of the high impedance of the tunnel junction and the stray/parasitic capacitance present in the electrical wires, bonding pads etc. Typical impedance for a tunnel junction is around $10^8 \, \Omega$ and the parasitic capacitance is on the order of pico-Farad, which yields a bandwidth of $(2\pi RC)^{-1} \approx 1-10 \, \text{kHz}$.

The experimental bandwidth of a tunnel junction can be increased by using the "*reflectometry*" technique described in Chapter 3 [3]. In this technique, the high impedance of the tunnel junction is matched to the characteristic impedance of a high-frequency read-out circuit with an LC transformer to remove the effect of the parasitic capacitances. After its first demonstration in SET electrometer [3], it has extensively been used to increase the operation speed of other high-impedance sensors [65-68]. Recently, this technique has also been applied to STM to increase its ordinarily low bandwidth [69]. They have reported that they increased the measurement speed of the STM to 10 MHz, which is 100 times better than a conventional STM.

With these solutions to the fabrication and the measurement speed problems in mind, we propose a new type of displacement sensor based on the detection of tunneling current between a resonating nano-beam and a metal tip. Our heuristic model is shown in Figure 4.6. In our model, the suspended metal tip stands in close proximity to the mid-point of the doubly clamped beam so that there is a vacuum tunnel junction between them. As the beam vibrates, the width of the tunnel junction (gap distance) changes. Remember that, when a bias voltage is applied between the beam and the tip, a tunneling current starts to flow which exponentially depends on the gap distance. The motion of the beam can be derived from this current. At this point, the tunneling current should be detected very fast in order to be able to capture all the information regarding high-frequency vibrations.
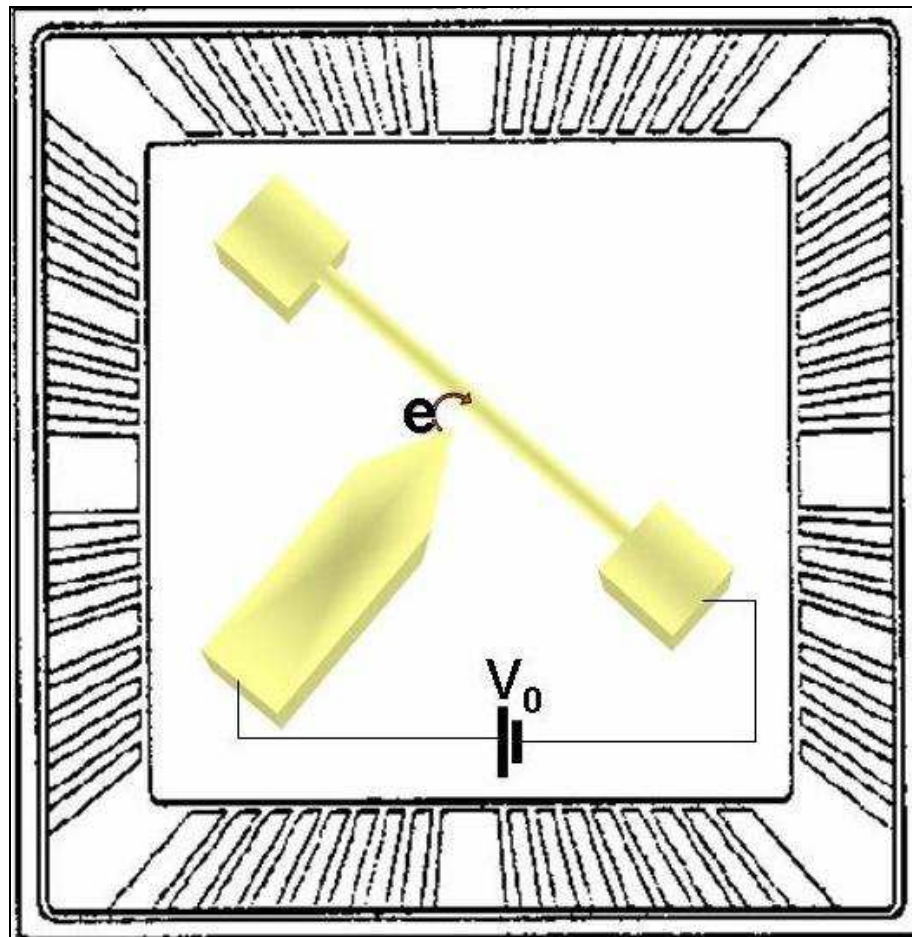

Figure 4.6: The simple model showing a vacuum tunneling displacement sensor. The metal tip is placed in the vicinity of the resonator's mid-point with a tunnel junction between them. When a bias voltage V_0 is applied across the junction, a tunneling current, which is very sensitive to the fluctuations in the tunneling gap, starts to flow. This current is detected with a high-frequency reflectometry as depicted in the next figure.

Therefore, a reflectometry is connected to the output of the tunneling sensor to realize the intrinsic wide bandwidth of the tunneling sensor. The basic idea of the read-out system is to use an LC tank circuit to match the sensor's impedance to a coaxial cable and detect the signal via the reflected voltage. The schematic of such a read-out system is given in Figure 4.7. The C_t and R_t represents the tunneling capacitance and the tunneling resistance of the vacuum junction respectively. The LC tank circuit not only matches the tunneling impedance and the coaxial cable but also determines the bandwidth of the operation and hence the speed of the sensor. During the measurement process, the tunneling resistance changes with the fluctuations in the tunneling gap and causes mismatch between the circuit and the coaxial cable. Therefore, some of the bias is reflected due to mismatch and the changes in the tunneling resistance can be deduced from these reflected voltages.
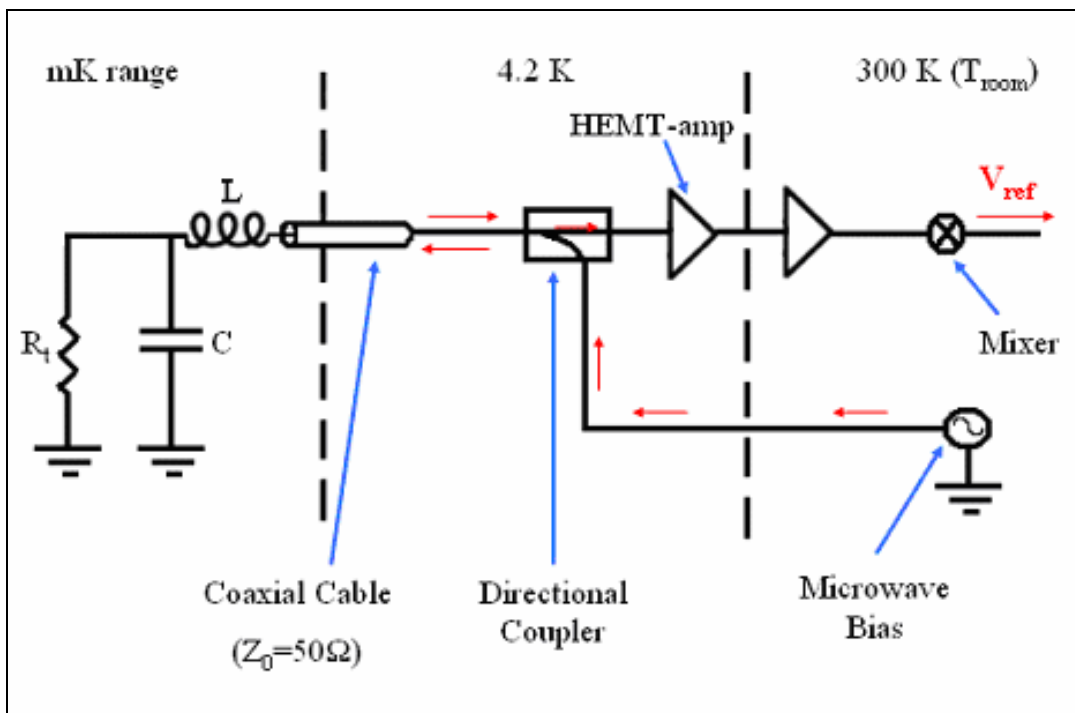

Figure 4.7: The high-frequency read-out is depicted.

CHAPTER 5

FABRICATION OF VACUUM TUNNEL JUNCTIONS

As discussed in the previous chapter, the main problem with the application of vacuum tunneling displacement sensor is the controlled fabrication of the vacuum tunnel junction between the doubly clamped beam and the metal tip. In this thesis, we propose a new fabrication method and experimental set-up for the realization of built-in vacuum tunnel junction in nano-systems. As defined before, a vacuum tunnel junction is approximately a nanometer wide gap between two suspended conducting tips. Vacuum tunnel junctions are modeled as high impedance (10^8 Ω) resistors whose resistance exponentially depends on the tunneling gap. In addition to STM and tunneling displacement sensor, vacuum tunnel junctions have other crucial applications in nano and molecular electronics [70-73]. Therefore, a method that enables highly controlled and high yield vacuum tunnel junction fabrication is very significant. Especially for our application, the value of the nominal gap is very important since it affects very crucial parameters such as coupling strength, gain and back action of the sensor all of which ultimately determines the sensitivity of the sensor. Therefore, a method that can fabricate tunnel junctions at a predetermined resistance with high yield is desired. In this chapter, first, present fabrication methods in literature will be discussed with their drawbacks. Then our fabrication method and the experimental setup will be elaborated with all the process steps and apparatus details. Finally, the results of the experiment will be presented.

5.1 Present Vacuum Tunnel Junction Fabrication Techniques

In addition to a prospective vacuum tunneling displacement sensor, tunnel junctions are widely used to connect nano systems and molecular devices to macroscopic electronic circuits [70-73]. Accordingly, many different fabrication techniques have been developed and implemented to fabricate tunnel junctions. Most prominent methods are the mechanical breaking [74-77] and electromigration [78-81]. In mechanically controlled break junction technique, a controlled force is applied to a nanowire by piezoelectric materials to break it into two electrodes [74]. It is possible to obtain tunable gaps with this particular method. However, a bulk and delicate piezoelectric breaking system is necessary to form and maintain the junction, which is not compatible with the nano system we proposed.   In electromigration method, electrodes with nano separations are formed by passing current though a nanowire [78]. While a large electric current density passes though a nanowire, the electrons transfer some of their momentum to the atoms in the wire. If the mobility of the atoms is sufficiently high, then the atoms start to migrate in a certain direction. The movement of the atoms shrinks the nanowire and at some point, the wire breaks and two electrodes with a junction are formed [79]. The main problem with electromigration is that the break of the nanowire occurs very sudden and hence it is very difficult to control the process. Recall that for the application of vacuum tunneling displacement sensor, a method that secures a built-in tunnel junction at a predetermined tunnel resistance is required.   Neither mechanically controlled breaking (not built-in) nor the electromigration (random tunnel resistances) satisfy this demand.   In the following section, we develop a junction fabrication technique that fulfills this requirement.

5.2 Vacuum Tunnel Junction Fabrication Method / Experimental Setup

In this thesis, we propose and implement a fabrication method for the realization of a vacuum tunnel junction between two suspended metal tips. The sought-after vacuum tunnel junction structure is shown in Figure 5.1. In this method, first, the metal tips, which are separated by 100 nm, are patterned on Silicon/Silicon Dioxide (Si/SiO$_2$) wafer using Electron Beam Lithography (EBL). Then the larger metal structures that couple the nano-tips to macroscopic wires are designed with Optical Lithography (OL). The metallization is done with thermal coating of Chromium/Gold (Cr/Au). Afterwards, the SiO$_2$ under the gold tips is etched with Hydrofluoric Acid (HF) to acquire the suspended structure. In the final and most peculiar step, the vacuum tunnel junction is realized with a second gold evaporation, which shrinks the gap between the tips in a controlled manner until a tunnel junction is formed between them. The details of each process step are given as follows.
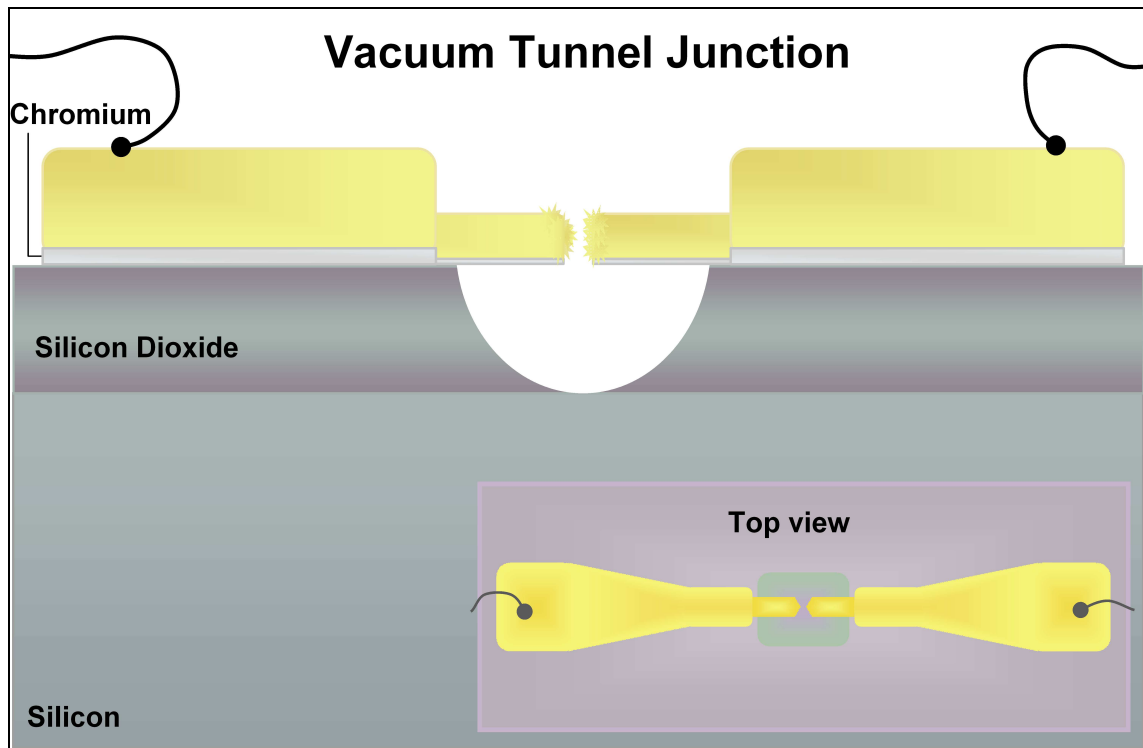

Figure 5.1: The side view and the top view of vacuum tunnel junction between two gold suspended tips are depicted. The small gold tips are patterned by EBL and the larger ones with OL. The SiO$_2$ under the tips is isotropically etched with an HF solution and the lithographically determine gap between the tips is shrunk down to a tunnel junction by a controlled gold evaporation.

5.2.1 Cleaving and Cleaning

A commercially available Si/SiO$_2$ wafer, 1 µm thick oxide is thermally grown on Si (100) surface, is used in this process. In the very beginning of the process, the wafer is cleaved into small pieces and cleaned according to following recipe:

1)   Hold in acetone in ultrasonic cleaner for 2 minutes
2)   Dip in 3 step acetone
3)   Dip in 3 step IPA
4)   Dry with nitrogen gun
5)   DEHYDRATION BAKE: Hold on hot plate at 120° for 2 minutes

5.2.2 EBL Markers

The next step after cleaning is the formation of EBL markers that provide a reference frame for the alignment of extremely small e-beam patterns to the other larger patterns of the device. The EBL markers shown in Figure 5.2, are built on wafer using liftoff process.
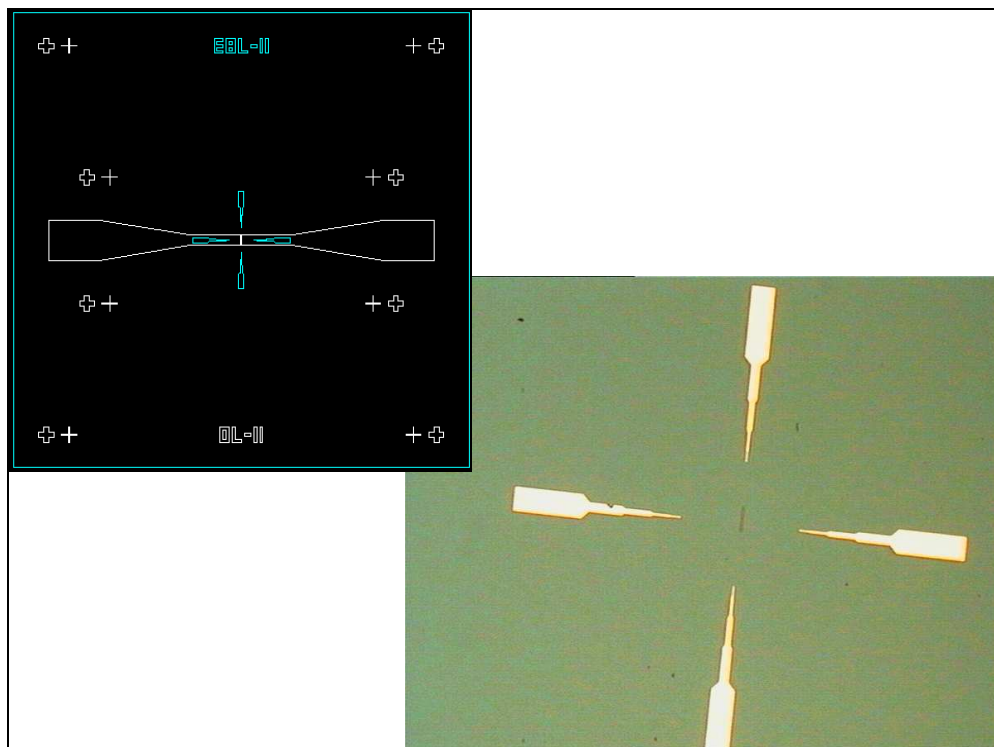

Figure 5.2: The AutoCAD drawing (blue lines) and the optical microscope image of the EBL Markers are shown.

In optical lithography, image reversal process of photoresist AZ5214E is preferred because negative resist profile is demanded for lift-off process. The recipe for AZ5214E image reversal optical lithography and succeeding metallization is given as following:

1) SPIN COATING: Spin the photoresist at 1200 rpm for 2 seconds and at 6000 rpm for 40 seconds.

2) PREBAKE: Hold photoresist coated sample on hot plate at 110° for 1 minute.

3) MASK EXPOSURE: Expose the photoresist through the mask using a mask aligner with a lamp power of 6 mW/cm^2 for 10 seconds. The important parameter in this step is the total exposure energy that is 60 mJ/cm^2. If the power of the lamp is different, the exposure time should be arranged such that the total energy remains the same.

4) POSTBAKE: Hold the sample on hot plate at 120° for 2 minutes. The value of the bake temperature is crucial for the overall process and after some trial and error experiments its optimum value is found to be 120°.

5) FLOOD EXPOSURE: Expose the photoresist without any mask using a mask aligner with a lamp power of 6 mW/cm^2 for 30 seconds. Like the previous exposure step, the crucial parameter is the total exposure energy which is 180 mJ/cm^2 and when the power of the lamp changes, the exposure time should be adjusted accordingly.

6) DEVELOPMENT: Develop the sample in the developer AZ726MIF for 70 seconds and then rinse with DI water. The development time is very important since it determines the profile of the photoresist. For a successful liftoff process, after the development the photoresist should have a negative or at least perpendicular profile. Different development times ranging from 40 to 100 seconds have been tried and it is found that 70 seconds development time gives the optimum profile.

7)   METALLIZATION: The patterned sample is coated first with 100Å Cr and then 1500Å Au using thermal evaporation. As the final step, after thermal deposition the sample is left in acetone for one hour to remove the photoresist and leave the metal EBL markers on the wafer.

In metallization step, Cr is used as an adhesive layer to adhere the Au structures to the SiO_2 surface because the adhesion between the Au and SiO_2 is very poor and another metal in between is needed to stick them together. The choice of Cr is not arbitrary since the adhesive layer should be resistant to the coming after steps such as HF etching. For instance titanium, very widely used metal for adhesion, cannot be used in this process because HF etches titanium.

5.2.3 Gold Tips

In this method, two facing metal tips that are as close to each other as possible should be fabricated using standard silicon technology. The resolution of the optical lithography is limited by diffraction and is typically around a few μm. On the other hand, more advance techniques like EBL can easily sustain resolutions around 100 nm. In this process two metal tips separated by a 100 nm, are patterned using EBL. Recall that a typical vacuum tunnel junction gap is around 1nm and as a matter of fact, in the final step, the 100 nm-distance between the tips will be shrunk with a second evaporation until a tunnel junction is formed. The EBL Pattern shown in Figure 5.3 is designed in AutoCAD and transferred to the sample using the EBL system at Bilkent University. The steps of EBL and metallization processes are given below.
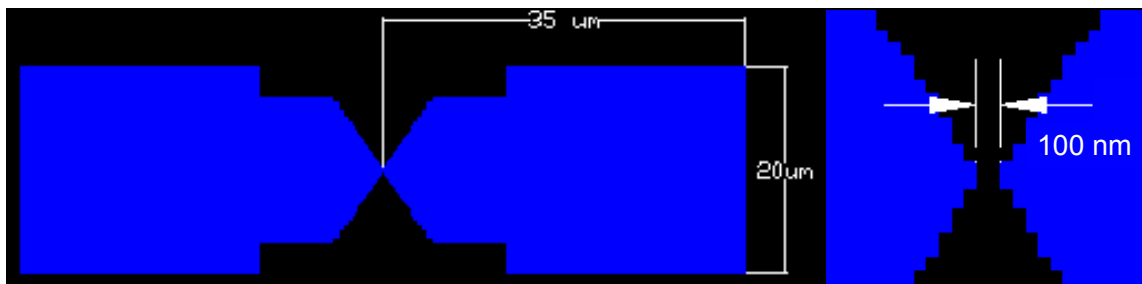

Figure 5.3: The EBL patterns drawn in AutoCAD

1) PMMA COATING: Spin coat Polymethylmethacrylate (PMMA), the resist used in EBL, at 1000 rpm for 3 seconds and at 4000 rpm for 50 seconds that corresponds to a resist thickness of 145 nm.

2) OVEN: Hold the PMMA coated sample in the oven at 160° C for 1 hour.

3) E-BEAM WRITE: The sample is placed in Scanning Electron Microscope (SEM) and the patterns are drawn on PMMA by the e-beam system with an exposure dosage of 260 $\mu C/cm^2$. At this step, the dosage of the e-beam is important to avoid both over- and under-exposure. Different dosages between 180 $\mu C/cm^2$ and 500 $\mu C/cm^2$ are tested and it is found out that the optimum dosage is 260 $\mu C/cm^2$ as shown in Figure 5.4.
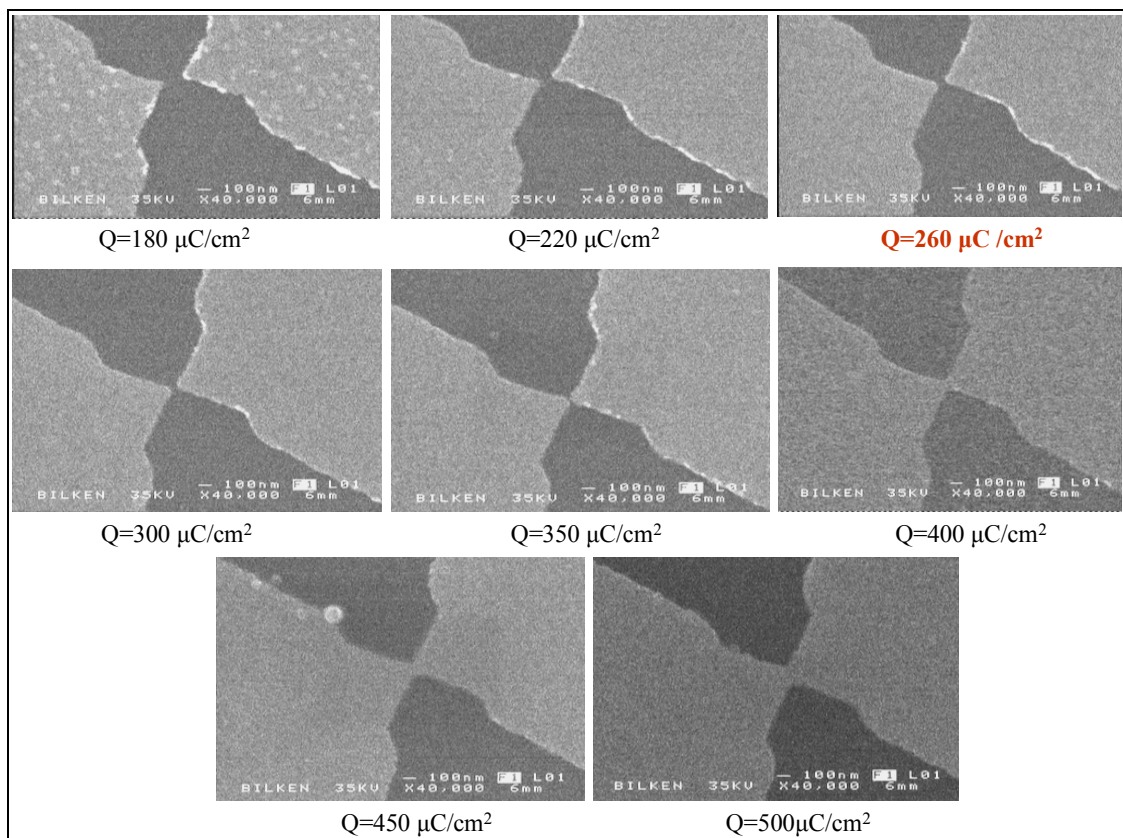

Figure 5.4: The EBL pattern is tested for 8 different dosages. After the metallization, the best result is obtained with the dosage Q=260 $\mu C/cm^2$.

4) DEVELOPMENT: After e-beam write, the sample is developed in 1:3 MIK-IPA for 60 seconds and then dip in IPA for another 60 seconds.

5) METALLIZATION: The patterned sample is coated first with 50 Å Cr and then 450Å Au using thermal evaporation and left in acetone for one hour to remove the photoresist. The SEM and optical microscopy images of the final EBL structure after metallization is given in Figure 5.5.
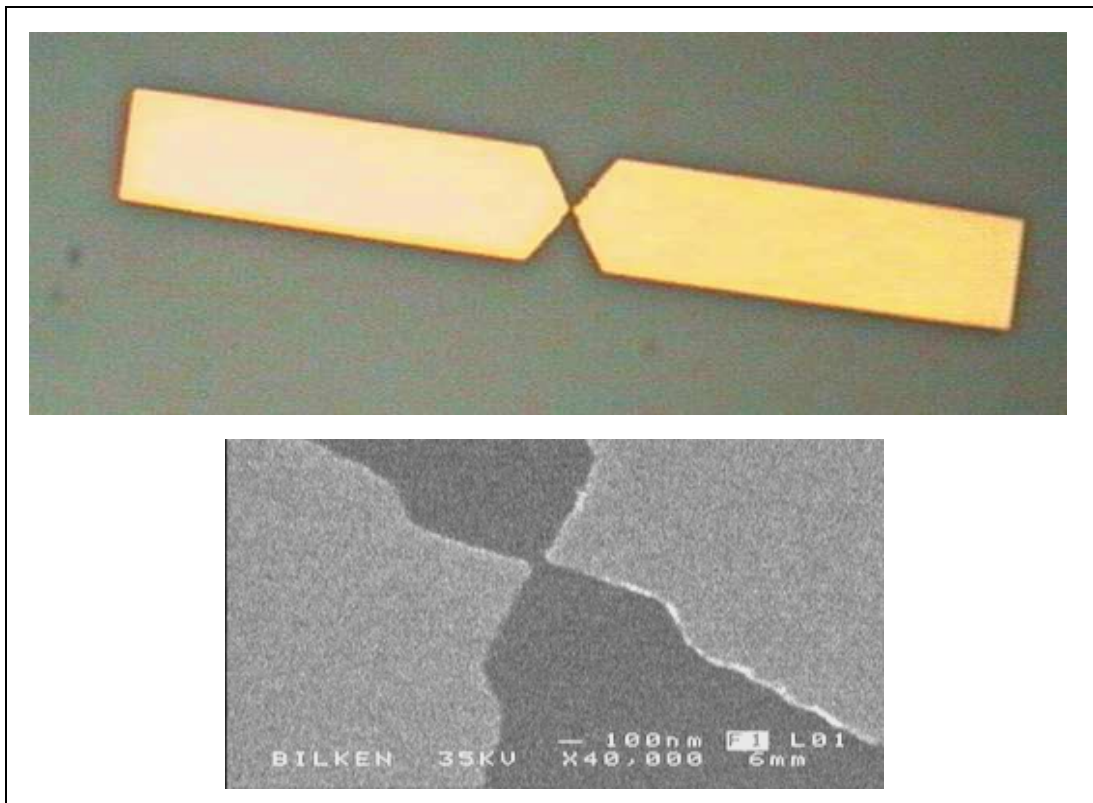

Figure 5.5. The optical microscope (top) and SEM (bottom) images of the EBL pattern after metallization are given. The distance between the metal tips is approximately 100 nm as desired and there is no apparent liftoff problem.

5.2.4 Contact Pads

Contact pads couple the extremely small e-beam patterns to the macroscopic electrical wires. The contact pads are fabricated with optical lithography and metal coating. The AutoCAD drawing of contact pads is shown in Figure 5.6. The pattern is aligned with the previously fabricated EBL structures using the EBL Markers. The liftoff process is exactly same with the process described for the EBL Markers in section 5.2.2.
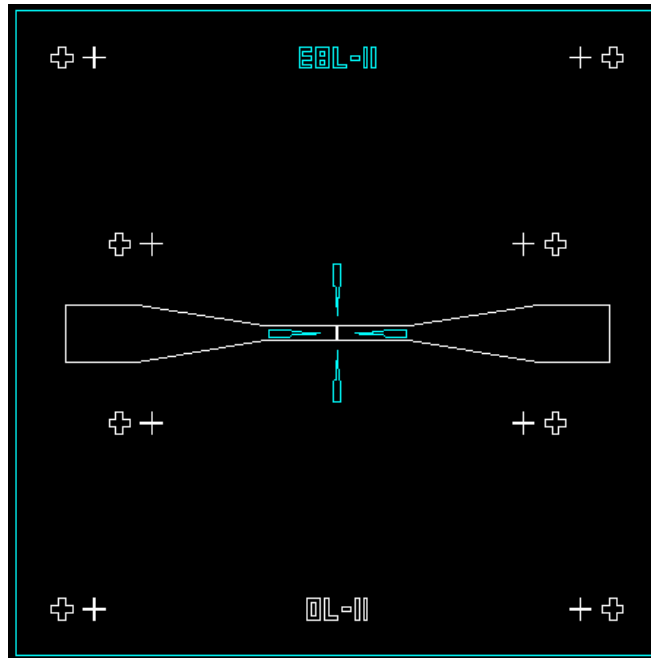
Figure 5.6: The AutoCAD drawing of the Contact Pads that are shown with white lines.

5.2.5 Evaporation Mask

As mentioned before, the initial gap between the gold tips patterned by EBL will later be shrunk with a second thermal evaporation. During this second evaporation, the area except the gold tips should be protected against the gold deposition to avoid any possible short contact. In accordance, an evaporation mask made of AZ5214E is designed which covers the structures other than the wire bonding areas and gold tips as shown in Figure 5.7.
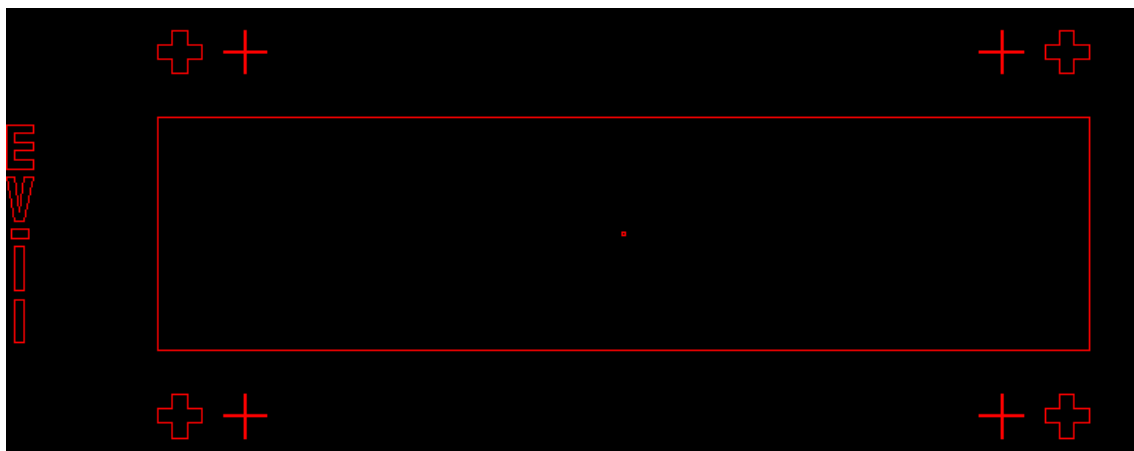

Figure 5.7: The AutoCAD drawing of Evaporation Mask.

The Evaporation Mask is patterned by positive optical lithography of AZ5214E. The recipe of the process is given as following:

1)   SPIN COATING: Spin the photoresist AZ5214E at 1200 rpm for 2 seconds and at 6000 rpm for 40 seconds.

2)   PREBAKE: Hold photoresist coated sample on hot plate at 110° C for 1 minute.

3)   MASK EXPOSURE: Expose the photoresist through the mask at 6 mW/cm^2 for 40 seconds.

4)   DEVELOPMENT: Develop the sample in the developer AZ726MIF for 70 seconds and then rinse with DI water and dry with nitrogen.
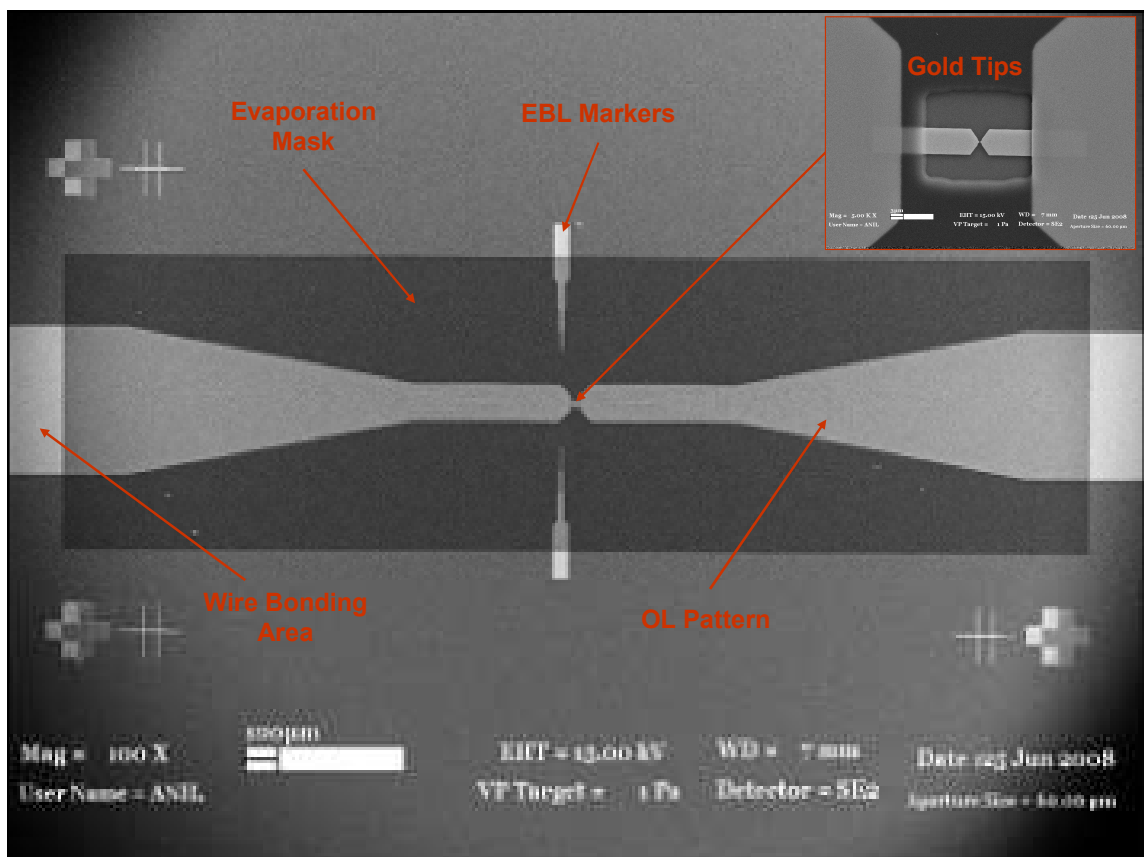

Figure 5.8: The SEM image of the structure after the evaporation mask step before the chemical etching is given.

5.2.6   HF Etching

The metal tips should be suspended and therefore the oxide under the tips is etched using isotropic chemical etching with HF. Different concentrations have been tried and it is found that in 1:1 HF:DI Water solution, the 1 µm-thick thermally grown oxide is totally etched in 7 minutes. The SEM images of the gold tips after HF etching are given in Figure 5.9.
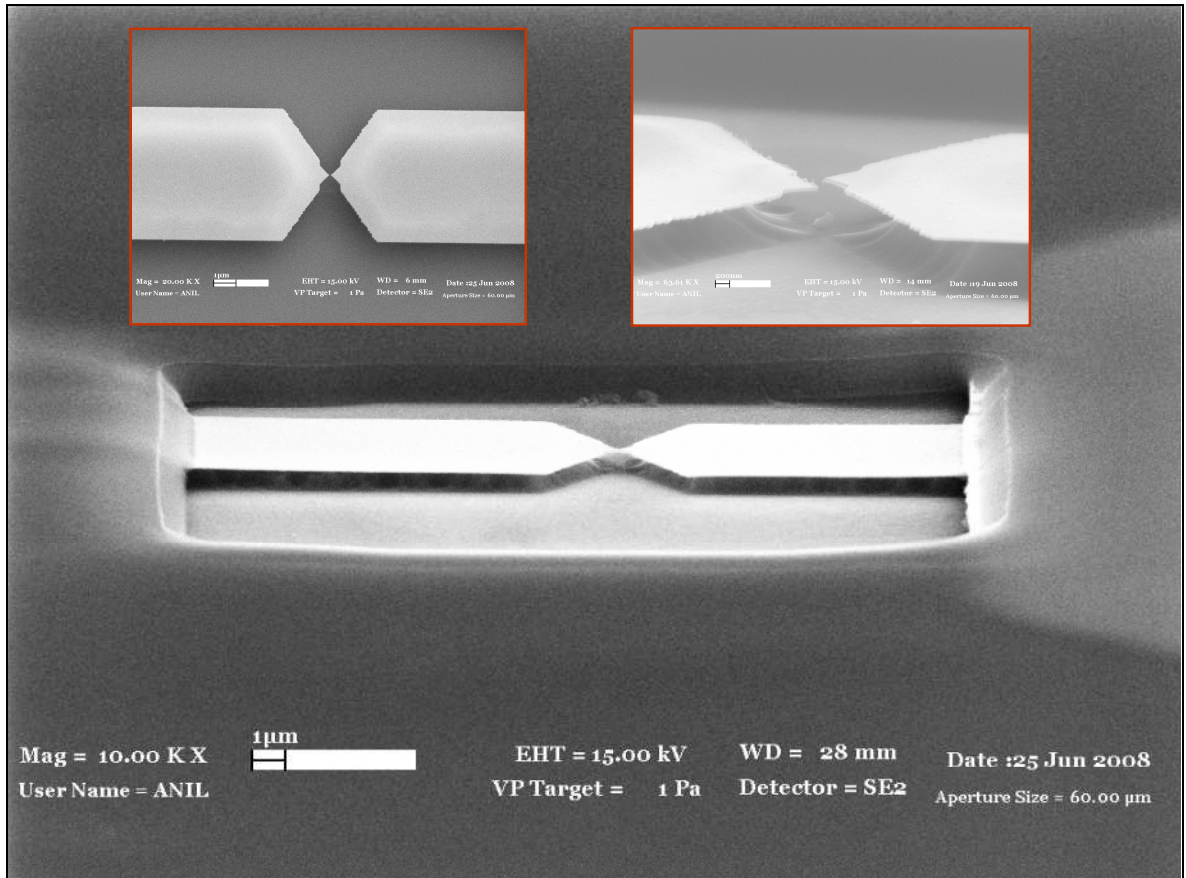

Figure 5.9: The SEM images of a sample after HF etching. The small images show the top-view and the side-view of the tips at larger magnifications.

5.2.6   Wire Bonding

Before the second evaporation, there is one final step, which is wire bonding. After etching, the samples are placed in the chip carriers and the electrical connection is made between the sample and the chip carrier by wire bonding. When the samples are connected to the chip carriers, they are ready for the second thermal evaporation, which is indeed our main experiment that enables controlled formation of vacuum tunnel junctions.

5.2.7 Controlled Thermal Evaporation

The controlled thermal evaporation is the most crucial step that makes our fabrication method innovative. This step essentially depends on the controlled shrinkage of the lithographically determined gap between the gold tips until a tunnel junction is formed between them. In order to determine precisely, when the gap fills into a tunnel junction, in-situ monitoring of the current across the junction is desired during the thermal evaporation. When the monitored current equals to the predetermined current, a control system halts the evaporation source instantly to prevent any further shrinkage in the gap and leave it in the tunneling regime. This method has great control over the fabrication process and it assures building tunnel junctions at predetermined tunnel resistance and gap distance. The main idea of this step is illustrated in Figure 5.10.
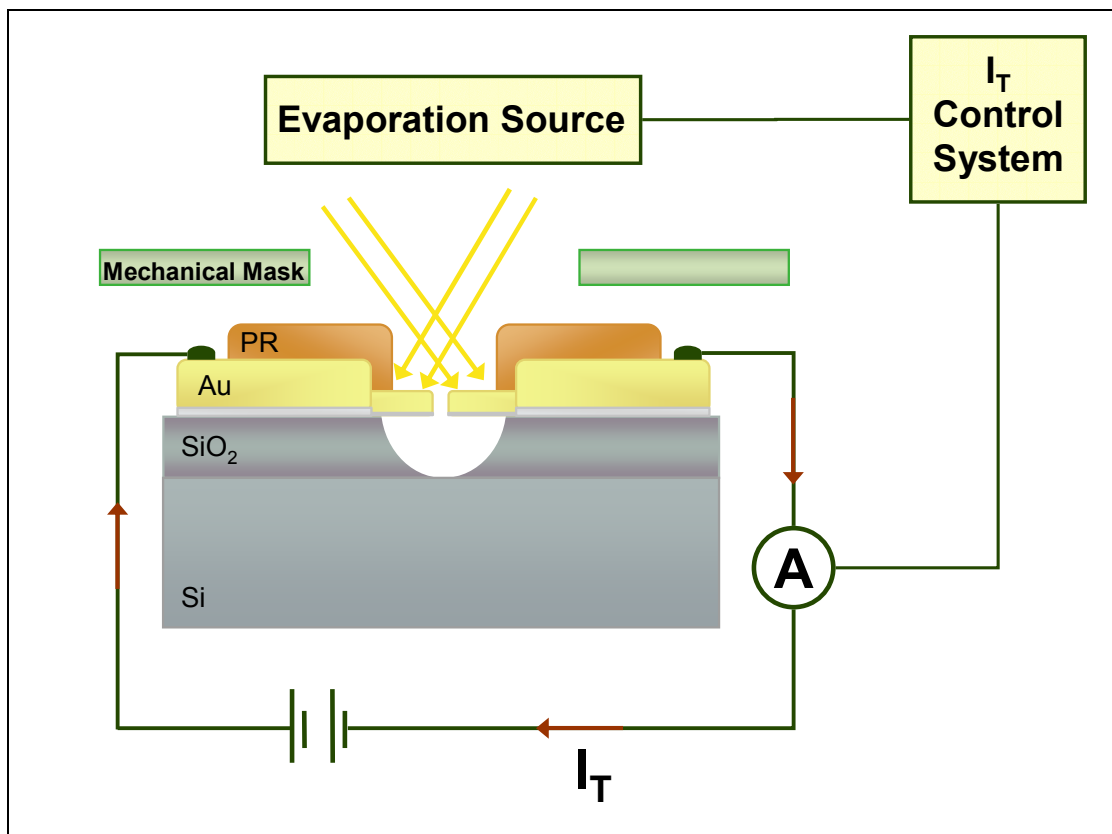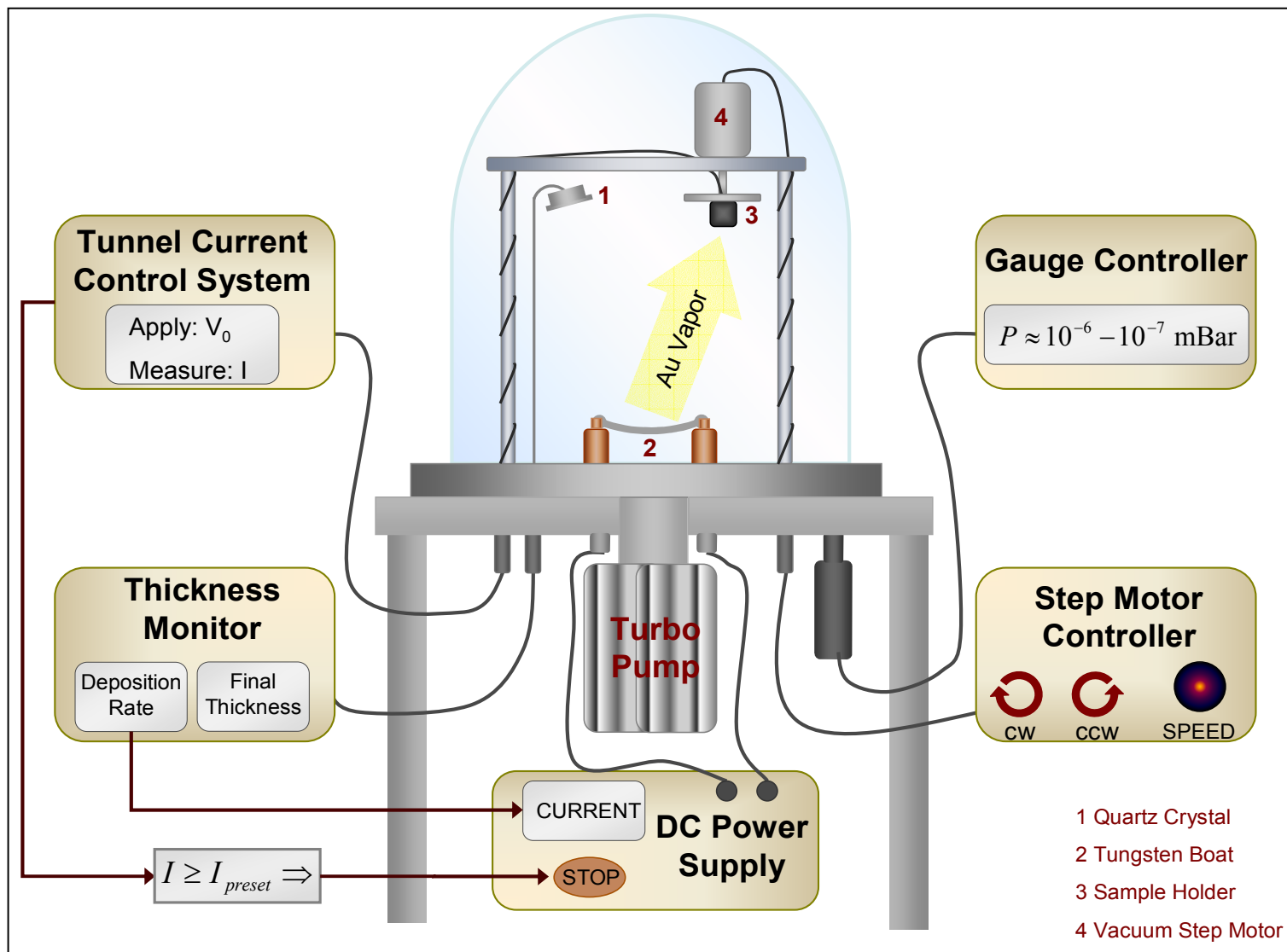

Figure 5.10: This figure illustrates the basic experimental setup for the controlled fabrication of vacuum tunnel junctions. The gap between the golden tips patterned by EBL is filled with directional gold evaporation and meanwhile the current between the tips is continuously measured under constant bias. When a current equal to predetermined tunneling current is detected, the evaporation is halted immediately leaving the junction in the tunneling regime.

When the process steps in the clean room are completed, the sample is placed in the chip carrier and the electrical interconnections are established between the sample and the chip carrier. Before thermal evaporation, a mechanical mask is placed on the chip carrier to protect the wire bonding area from gold vapor. Now the sample is ready for the thermal evaporation experiment. For this experiment, we have designed and constructed a special high vacuum thermal evaporation system. The system is illustrated in Figure 5.11 on page 72. This home-made system enables directional evaporation and in-situ conduction detection. The details of the experiment and the system is as follows.

DIRECTIONAL & ROTATIONAL EVAPORATION: The chip carrier covered with the mechanical mask, is placed in the sample holder of the evaporator and the system is pumped down to pressures on the order of 10^{-6}-10^{-7} mBar. There is an angle between the evaporation source, which is solid gold on a tungsten boat, and the sample to provide directional evaporation. Additionally, the stage of the sample holder is rotatable through a vacuum step motor. Both the direction (clockwise, counterclockwise or alternating) and the speed of the rotation is controlled with an electronic system designed by ourselves. The directional-rotational evaporation is desired to promote lateral growth rather than vertical growth.

DEPOSITION RATE AND THICKNESS MONITOR / CONTROL: The solid gold on the tungsten boat evaporates when a sufficiently high DC current passes though the tungsten boat. Under high vacuum condition, the mean free path of the gold vapor atoms become large enough that the atoms can reach to the substrate like an arrow without any collisions. The rate of the deposition depends on the amount of the current. In our setup, the high current is supplied by Agilent DC power supply that can produce current up to 165A. During evaporation, the deposition rate and the total thickness are both monitored and controlled with a thickness monitor / controller, Inficon XTC2. Inficon XTC2 monitors the deposition rate and the thickness through a quartz crystal in the chamber. A quartz crystal's resonance frequency shifts with the additional mass of deposited gold. Thickness monitor calculates the deposition rate and total thickness of the thin film from the shift in the resonance frequency. In addition to monitoring, XTC2 can communicate with the power supply and tune the deposition rate by controlling the output current of the power supply. This feature is important for our

Figure 5.11: The illustration of thermal evaporation system

Tunnel Current Control System

Apply: V_0

Measure: I

Thickness Monitor

Deposition Rate

Final Thickness

$I \geq I_{preset} \Rightarrow$

Au Vapor

4

1

3

2

Turbo Pump

CURRENT

DC Power Supply

STOP

Gauge Controller

$P \approx 10^{-6} - 10^{-7}$ mBar

Step Motor Controller

CW   CCW   SPEED

1 Quartz Crystal

2 Tungsten Boat

3 Sample Holder

4 Vacuum Step Motor

experiment because we want to cease the evaporation as soon as possible when a tunneling current is detected. Therefore, lower deposition rates, maximum of 1 Å/s, are demanded to have sufficient control over this stop process.

IN-SITU CONDUCTANCE MEASUREMENT: The most important feature of our home-made evaporation system is the in-situ electrical measurement of the sample during deposition. The sample in the vacuum chamber is electrically connected to a semiconductor parameter analyzer, Agilent 4156C, via a BNC feed through. During evaporation, Agilent 4156C applies a constant voltage to the sample and measures the current simultaneously. We control the parameter analyzer with a LabView program on PC. This LabView program sets the output voltage of the parameter analyzer and then reads the current data. It continuously compares the measured current to the predetermined tunneling current value, which is set by us as a threshold value in the beginning of the process. Originally, the gap between the tips is wide and there is no current other than the femto-Amper range random noises. As the deposition proceeds, the gap becomes narrower and narrower and at some point, it enters the tunneling regime that causes a very sharp increase in the measured current. When the measured current reaches the threshold value, the PC immediately terminates the evaporation by halting the power supply. At the end of this process, a vacuum tunnel junction is formed at a predetermined resistance. The typical values we practice are a bias voltage of 100 mV and a tunneling current of 1 nA, which forms a tunnel junction with a resistance of 10^8 Ω. The values of the tunneling resistance and hence the tunneling gap can easily be tuned by simply changing either the bias voltage or the threshold current. This method offers great control over the process and increases the fabrication yield.

The system has some other features that are not mentioned above since they are not directly related or critical for our experiment. For instance, the evaporation system has indeed three different evaporation sources each preserved for different materials and the choice of the source is done with a high current switch between the tungsten boats and the power supply. There is also a water cooling system that cools down the quartz crystal to avoid thermal shifts in the frequency and thus to measure the deposition rate and final thickness more accurately. Last but not least, the pressure of the system is measured throughout the process with an ion gauge.
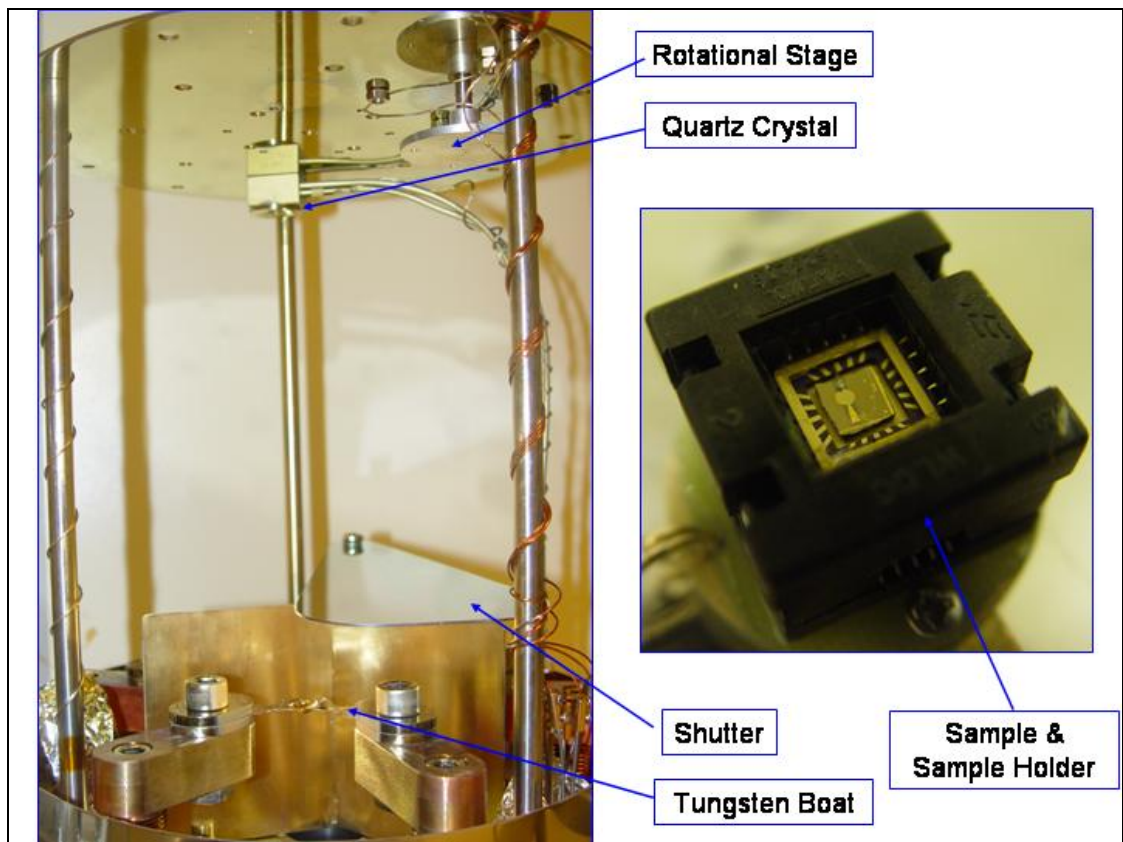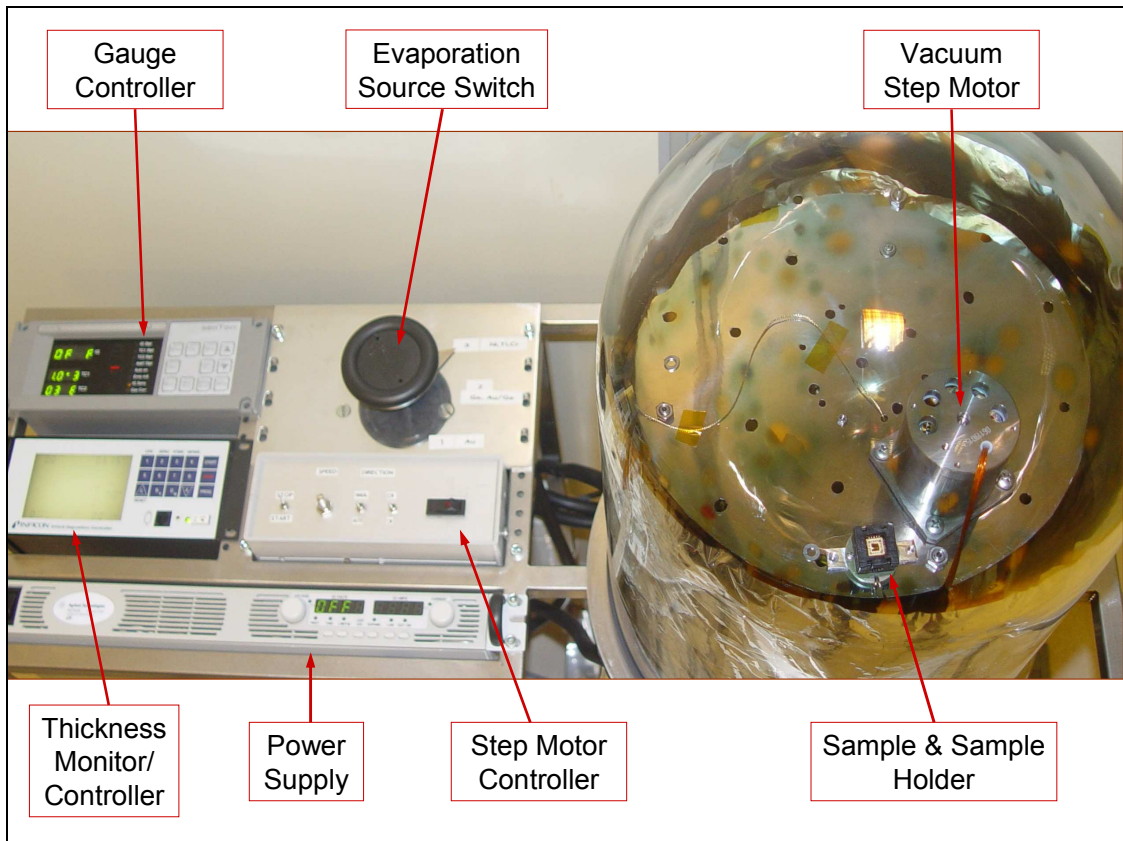
Figure 5.12: The real pictures of the home-made evaporation system are given.

5.3 Results and Discussion

During this thesis work, we have fabricated two sets of samples in the clean room of Bilkent University. In the first set, there was a lift-off problem with the EBL patterns. There were three surviving samples after all the fabrication processes. However, in all of them, the metal between the tips did not tear off, which causes the metal tips contact each other as shown in Figure 5.13.
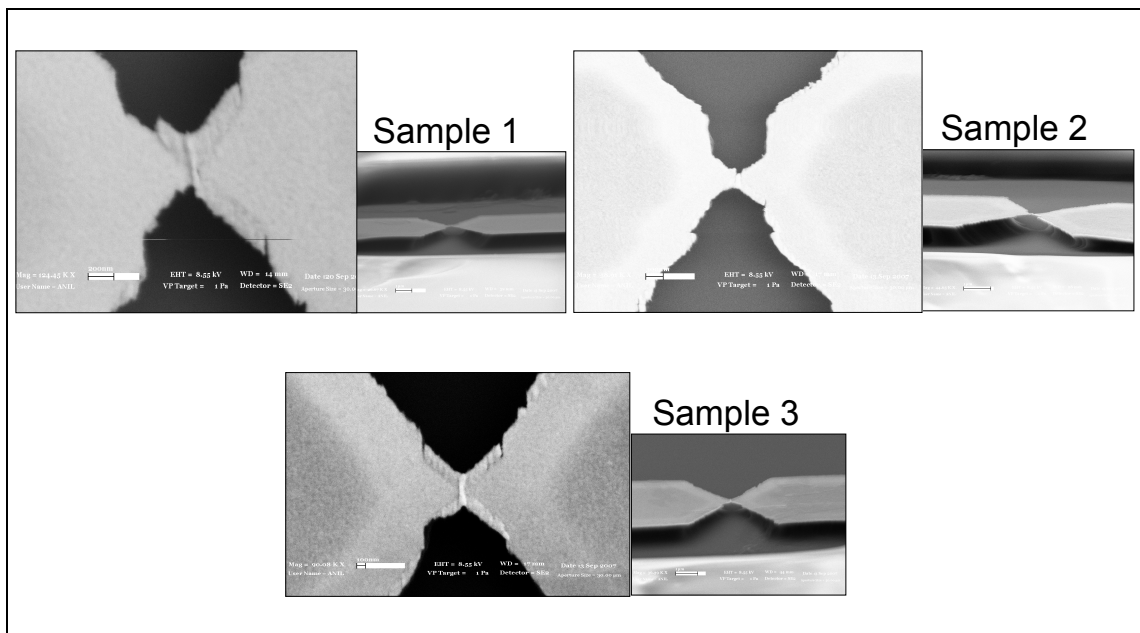

Figure 5.13: The SEM images of the set of three samples fabricated in Bilkent University Clean Room. The only problem of the process is with the EBL lift-off.

We have thought of breaking these contacts using electromigration and then implement the controlled thermal evaporation, yet; meanwhile the contacts are self-burnt probably due to static electricity. The SEM images of the samples with gaps after electrostatic burning are given in Figure 5.14. In samples 1 and 2, even though the shapes of the tips are heavily distorted, the gap distance between them is manageable with thermal evaporation. The width of the gap in Sample 1 is around 100 nm and less than 300 nm in Sample 2. On the other hand, Sample 3 is totally ruined by the static electric. We continued the thermal evaporation experiment with Sample 1 and 2.
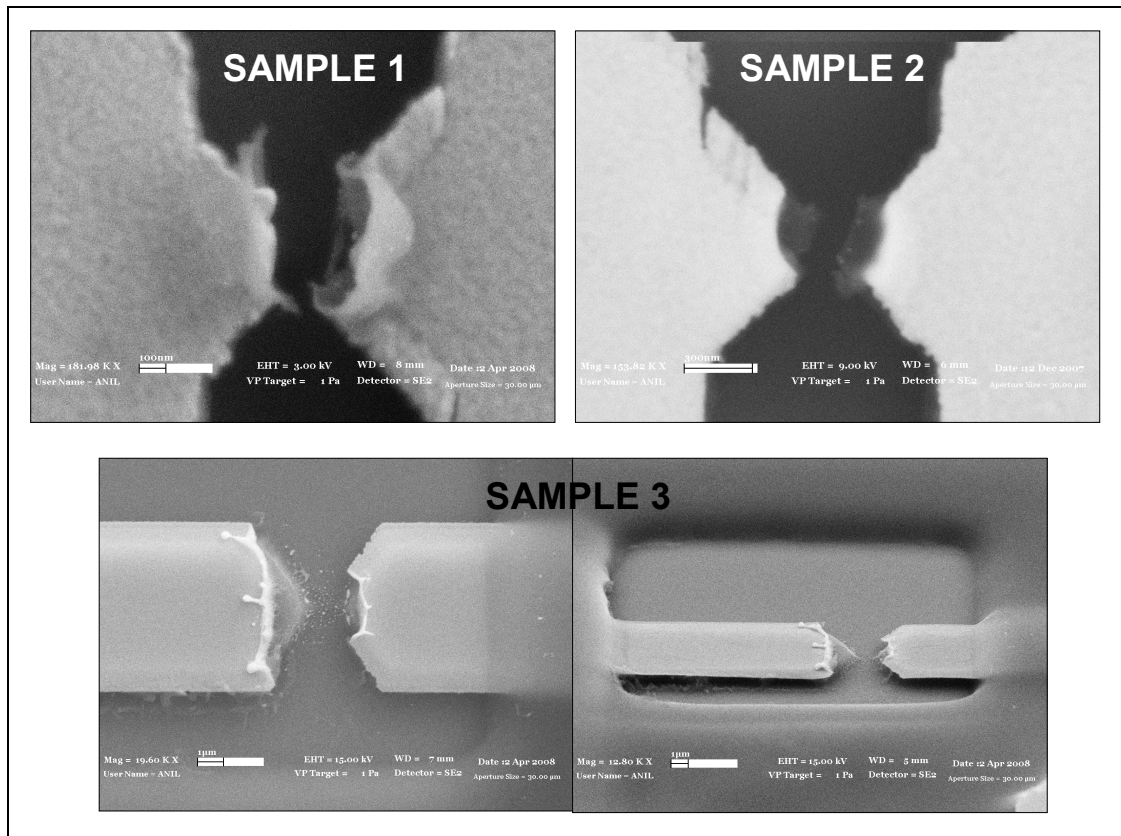
Figure 5.14: SEM images of the three samples after their contact points are self-burnt due to static electric.

SAMPLE 1: Sample 1 was the most promising sample after electrostatic incident with a gap of 100 nm, which is the initially intended value of EBL pattern. In Sample 1, the main problem is the shape of the gold tips, because such an arbitrary, distorted shape makes it impossible to guess the growth mechanism. Therefore, we performed the evaporation step by step to reconnoiter the growth mechanism and keep the process under control. The SEM images of the sample after each evaporation step are shown in Figure 5.15 along with the current versus process time curve obtained during whole evaporation given in Figure 5.15. In the third evaporation, the process halted with the detection of the tunneling current. The SEM images show that the gap is filled the evaporated gold atoms in the desired direction. According to thickness monitor, a total thickness of 300 nm gold is deposited at the end of the evaporation.
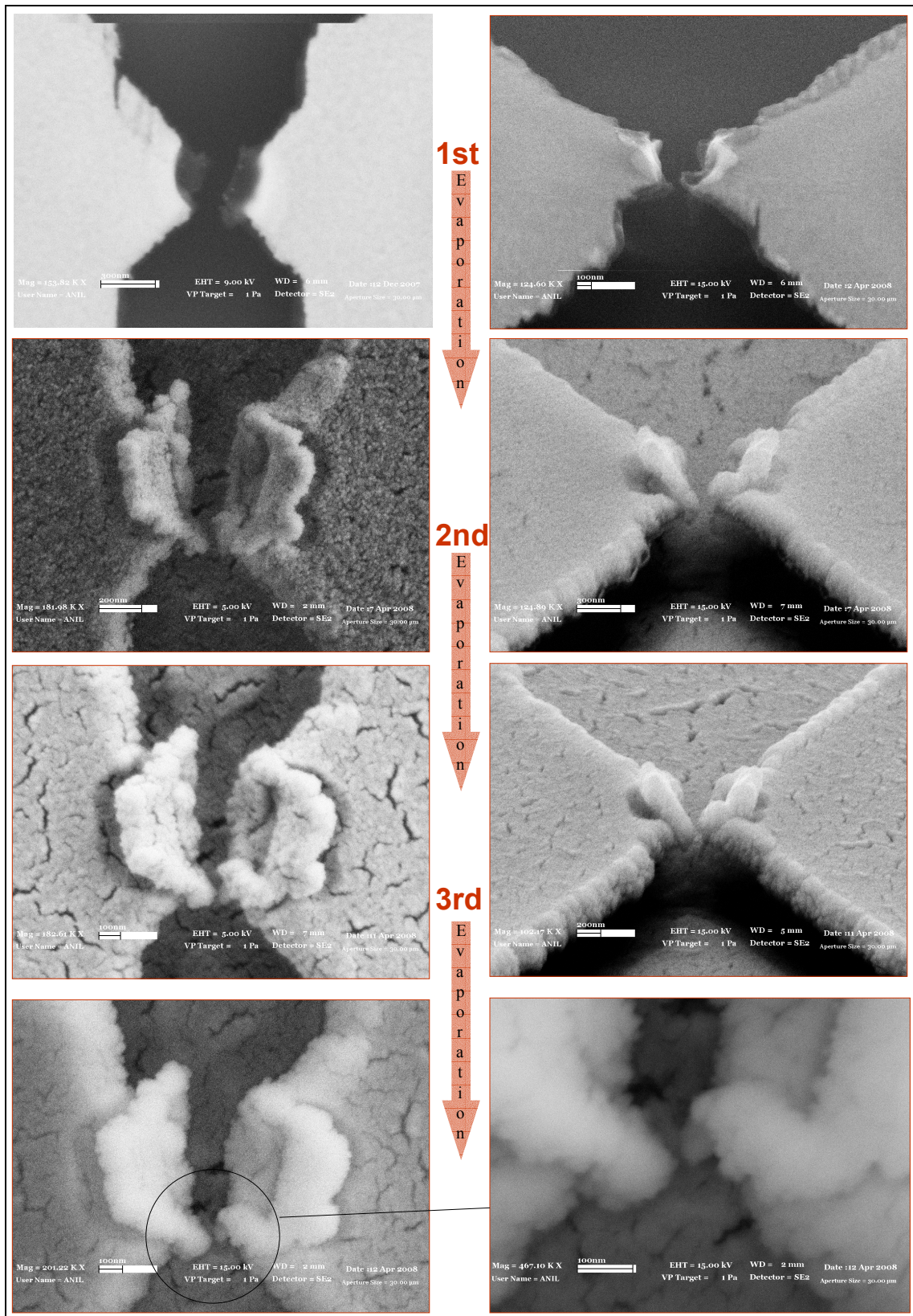
Figure 5.15: The SEM images of Sample 1 after each evaporation step are given. Images on the left are the top view and images on the right are the tilted view of the sample. It is obvious that the gap shrinks after each step. The third, and the last, evaporation is halted automatically when the tunneling current is detected.
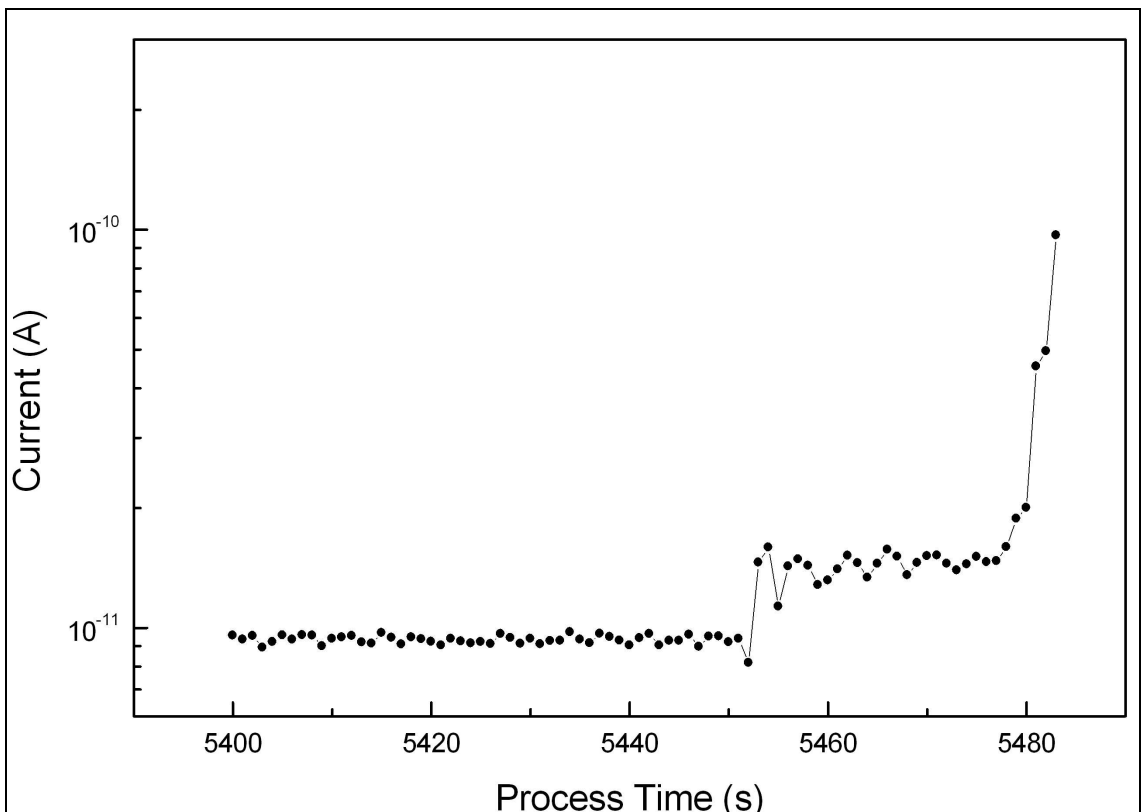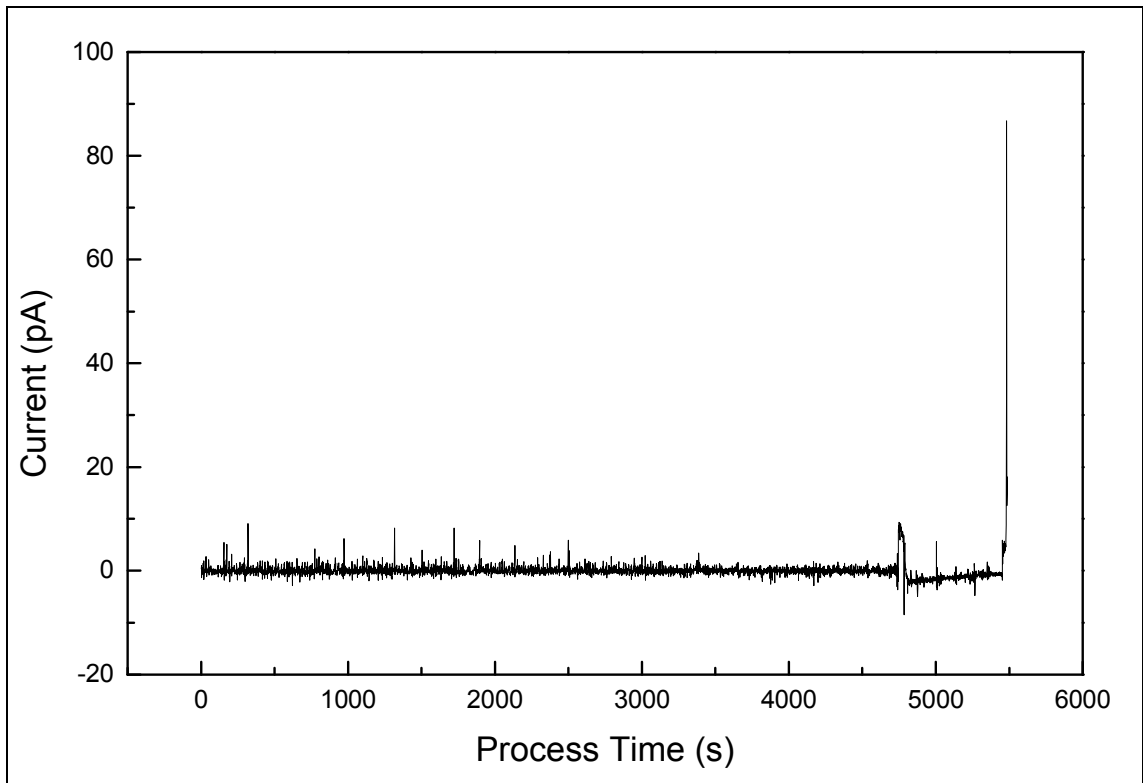
Figure 5.16: The current through the gap is plotted in the first graph against the whole process time and the detailed data points of the sudden rise towards the end of the process are given in the second graph. When the sudden increase in the end is detected by the computer, the evaporation process halted immediately.

SAMPLE 2:   Same process is repeated for Sample 2. The evaporation is performed step by step and the sample is examined in SEM after each step. At the end of the second evaporation, the originally 300 nm wide gap had been reduced to 80 nm. Unfortunately, after the third evaporation it is observed that Sample 2 is ruined as shown in Figure 5.17, before detecting any tunneling current. The reason of this distortion is most probably resulted from the different thermal coefficients of the gold and chromium. During the evaporation, the sample heats up and, hence expands. When the evaporation ended, the chamber cools down to room temperature and this time the metals contract. The gold and the chromium do not contract in equal amounts, which cause a stress on the sample. We guess that the gold layer is curled up because of this stress. This result shows us that the evaporation should be done in more and shorter steps to prevent the overheating of the sample.
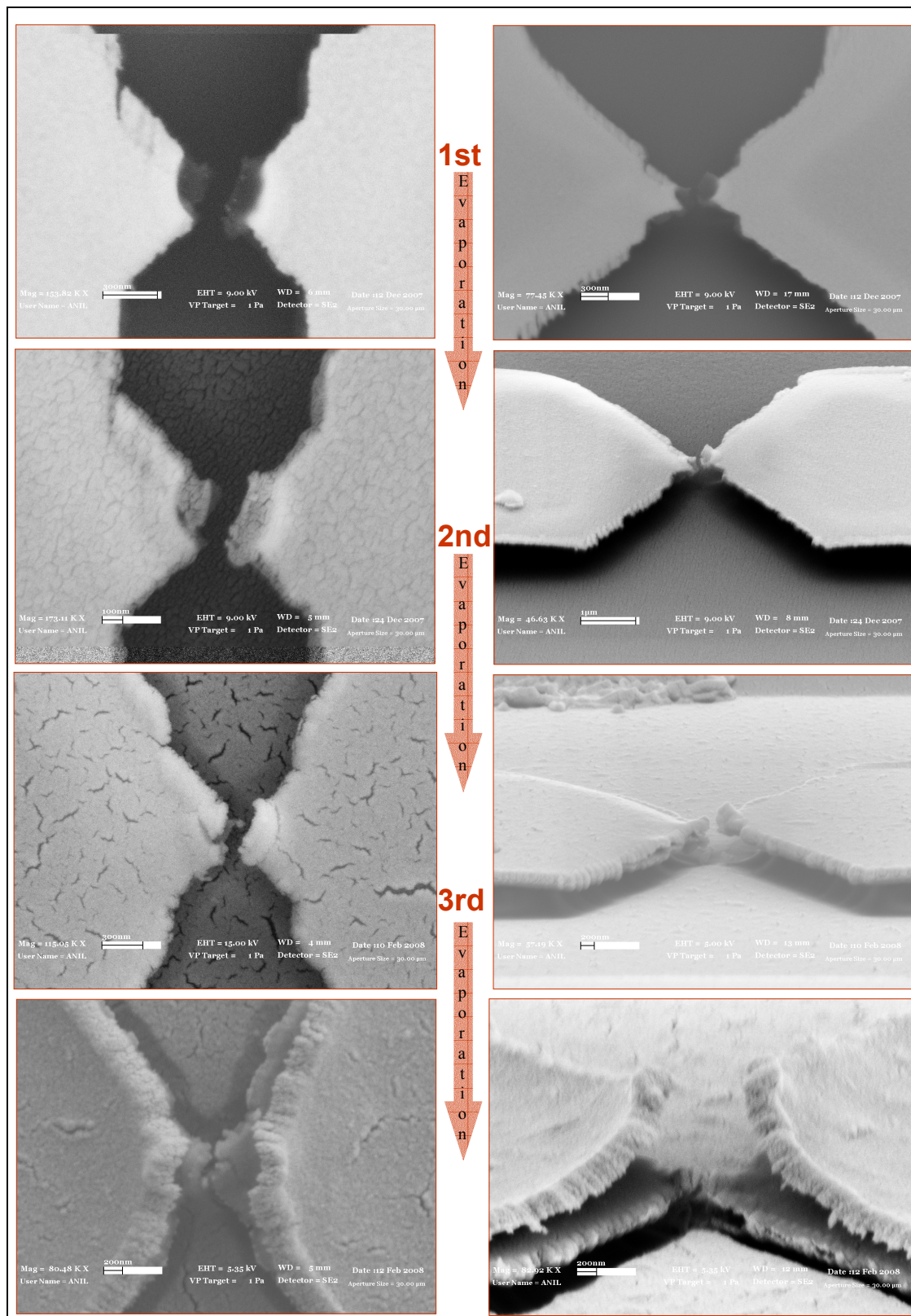
Figure 5.17: The SEM images of Sample 2 after each evaporation step are given. Images on the left are the top view and images on the right are the tilted view of the sample. We managed to shrink the originally 300 nm wide gap down to 80 nm at the end of the 2nd evaporation. However, the gold layer has been curled up and the sample has been ruined after the 3rd evaporation.

In order to verify the results we obtained with Sample 1, we fabricated another set of samples again in the Bilkent University's clean room. In this set of samples, the lift-off problem in the EBL patterns has been solved as you can see in Figure 5.18. On the other hand, this time we faced another problem regarding the HF etching process. In many samples, most of the oxide under the EBL structures was etched and thus the structures fell down as shown with the SEM images in Figure 5.19.
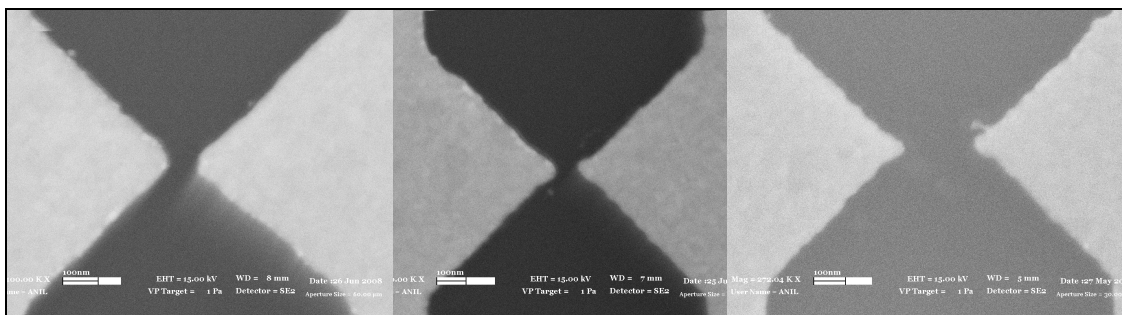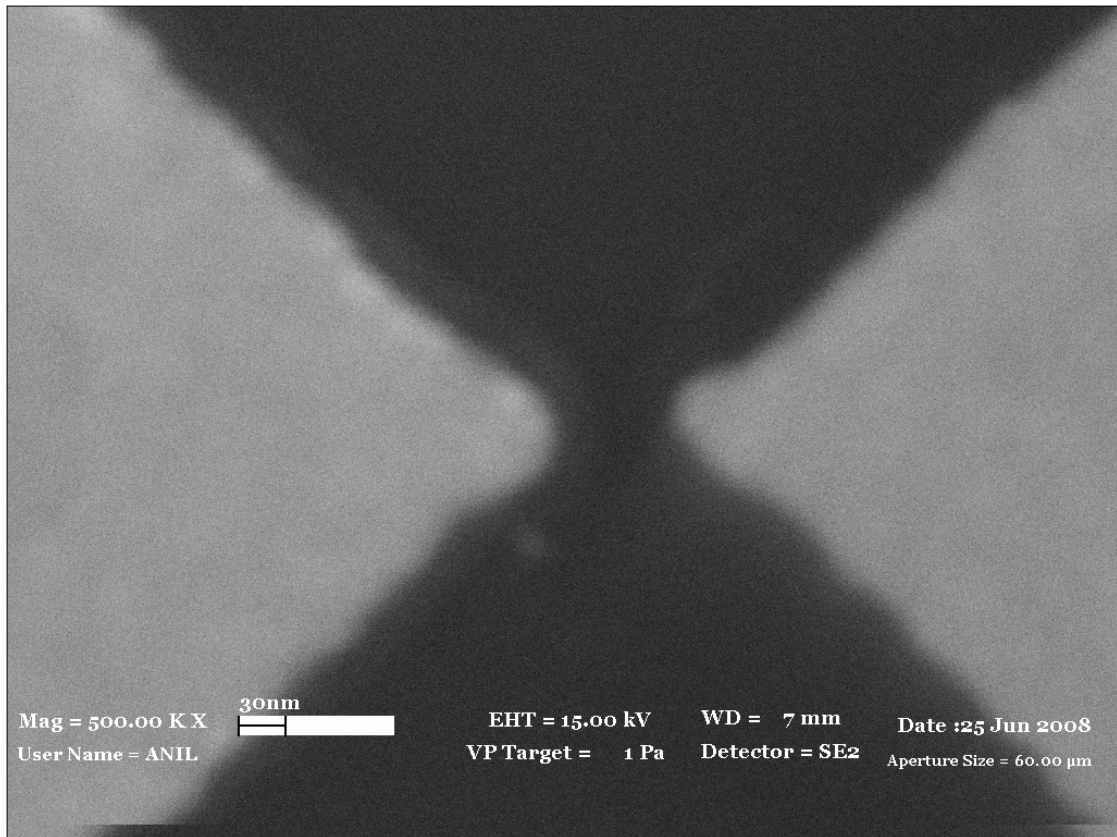

Figure 5.18: High magnification SEM images of the gaps patterned by EBL. In the second set of the sampled the lift-off problem have been solved and gap distances smaller than 50 nm have lithographically been achieved.
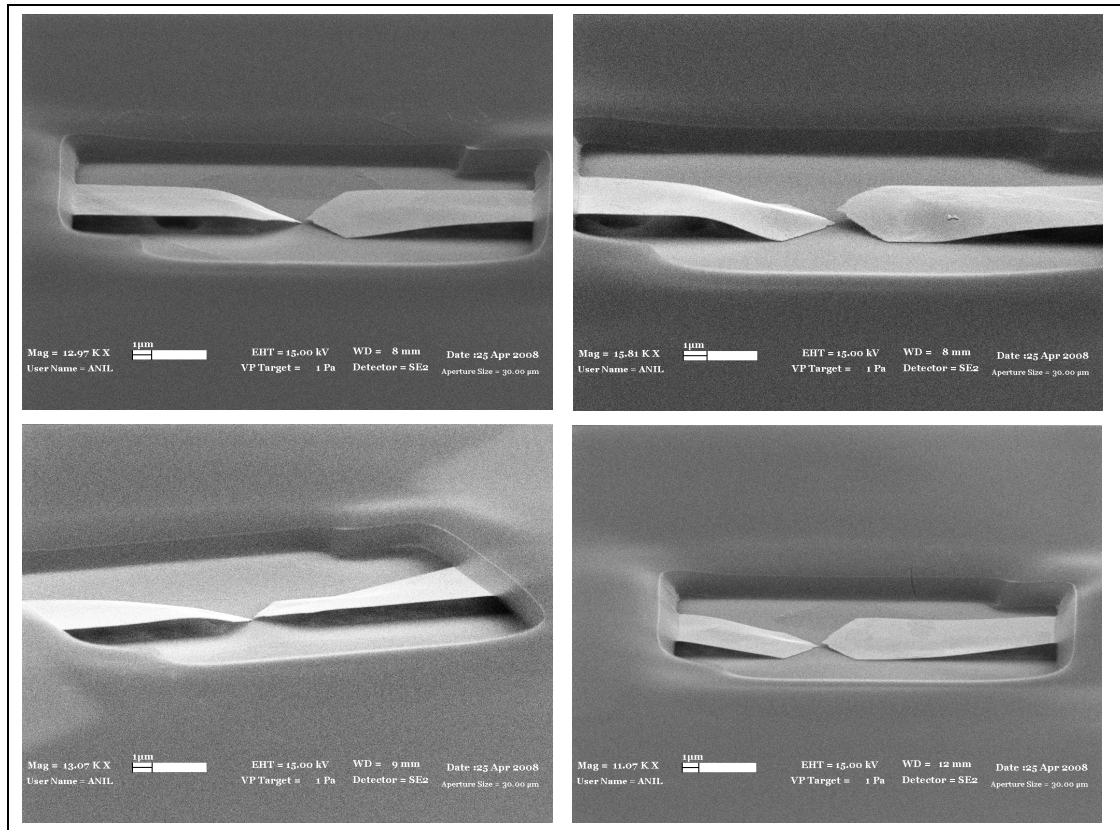
Figure 5.19: The SEM images of the samples with HF etching problem. Since most of the oxide under the tips has been etched, the metal structures fell down after etching.

These images indicate an over-etching problem at first sight. However, the HF concentration and etching time testes several times on blank SiO_2, and proved that this can not be an over-etch problem. The only explanation left is that the metal structures were not attached on the SiO_2 surface properly and as a result, the HF solution could easily penetrate between the metal structures and the wafer surface and etched the oxide under. This adhesion problem also revealed itself during wire bonding, because the gold contact pads easily detached from the surface.

Due to this etching problem, we could not obtain any suspended tips and could not repeat the controlled thermal evaporation experiment. Most of the problems we confronted were device fabrication related despite the fact that we have optimized each step (EBL patterns, HF Etching etc.) very carefully. The problem is that the metal structures could not resist the HF for such long etching times. Therefore, we have decided to try the process on a different wafer for which the etching time is shorter. We have repeated the same process on a PECVD grown oxide. For this wafer, the etching time of 1 μm oxide is approximately 20 seconds. The metal structures could resist the

HF for this short etching time and therefore we could obtain the suspended structures as shown in figure 5.20. Unfortunately, we did not have time to test these structures in the evaporation experiments. Yet, we guess that the very small (≈30 nm) gaps will easily be shrunk down to tunneling junctions.
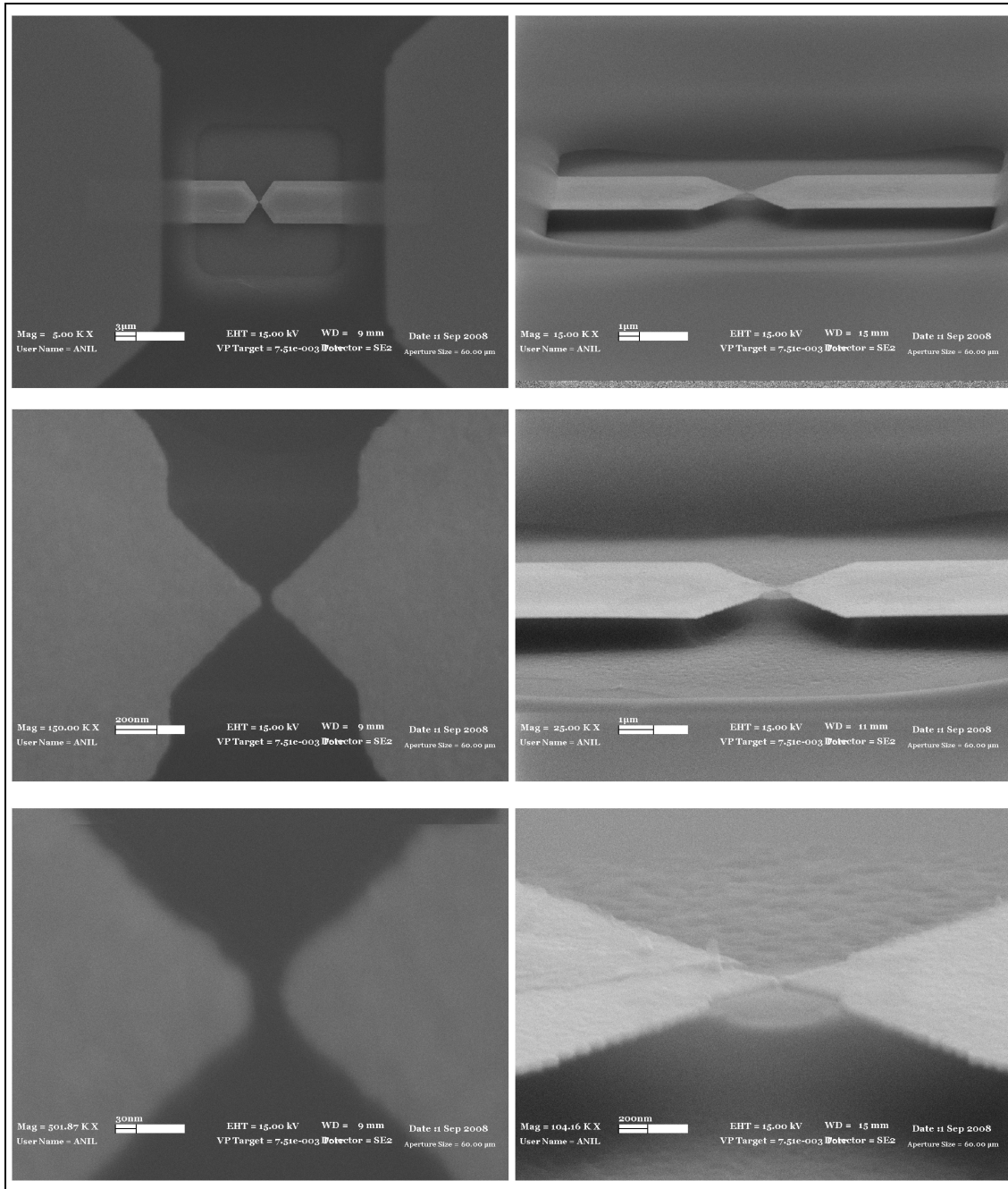

Figure 5.20: The SEM images of the samples patterned on PECVD grown oxide. The gold structures have survived the 20 second etching time and we managed to obtain the suspended tips with approximately 30 nm separations between the tips.

CHAPTER 6

CONCLUSION AND FUTURE WORK

In this thesis, a new displacement sensor towards detecting motion at ultimate quantum limit was proposed. After the introduction, in the second chapter, the quantum mechanical limit, which is the ultimate limit to the fluctuations of a resonator, was calculated and discussed. The mechanical and electrical properties of a quantum-ideal displacement sensor were given using a fully-quantum mechanical approach. Then, in the third chapter, NEMS, the most suitable systems for the quantum-limited position detection experiements, were described. The importance of the mechanical features of the resonator and their relevancy to quantum measurements were given. In the same chapter, some present displacement sensors were discussed focusing on the fact that none of them has detected quantum mechanical features of a nanomechanical resonator. The weaknesses of these sensor and the reasons that prevent them reaching quantum limit were identified. In the fourth chapter, a new displacement sensor based on the detection of the tunneling current between a vibrating nanoresonator and a metal tip was proposed. The noise and sensitivity calculations were carried out for this sensor and it has been showed that theoretically, it is capable of reaching the quantum limit. In the same chapter, the problems regarding the experimental realization of such a sensor were explained and some solutions were suggested. In the fifth and the last chapter, a new methodology was developed and tested for the fabrication of vacuum tunnel junctions. The very early results of the experiment indicated that the controlled thermal evaporation system is working properly. We have finally also managed to solve the problems of device fabrication by switching from thermally grown oxide to PECVD grown. The controlled fabrication of tunnel junction has its own importance in nanoelectronics and molecular electronics. Besides, this fabrication method can be

adapted to a resonator-sensor systems and the theoretically outstanding vacuum tunneling sensor can be realized and tested experimentally. Of course, the fabrication of the beam-tip system will be much challenging than the tunnel junction fabrication and the materials and the processes should be chosen accordingly. If this system measures displacement at the ultimate quantum limit as expected by theory, then it will be capable of detecting the zero-point fluctuations of a macroscopic nanomechanical resonator. Such an observation will have a huge impact in fundamental physics. It will help physicist to answer the questions of "Why quantum mechanical phenomena are not observed in macroscopic world; how and under what conditions the transition between the classical mechanics and quantum mechanics occurs". Even if it does not reach the quantum limit, the realization of a sensitive and fast displacement sensor built in a nanomechanical resonator is still worthy in itself.

BIBLIOGRAPHY

[1] C. M. Caves, K. S. Thorne, R.W. P. Drever, V. D. Sandberg, and M. Zimmerman. "On the Measurement of a Weak Classical Force Coupled to a Quantum-Mechanical Oscillator. I. Issues of Principle", *Reviews of Modern Physics* **52** (1980), 341-392.

[2] Y. T. Yang, C. Callegari, X. L. Feng, K. L. Ekinci, and M. L. Roukes. "Zeptogram-Scale Nanomechanical Mass Sensing", *Nano Letters* **6** (2006), 583 -586.

[3] R. J. Schoelkopf, P. Wahlgren, A. A. Kozhevnikov, P. Delsing, and D. E. Prober. "The Radio-Frequency Single-Electron Transistor (RF-SET): A Fast and Ultrasensitive Electrometer", *Science* **280** (1998), 1238-1242.

[4] R. Knobel and A. N. Cleland. "Piezoelectric displacement sensing with a single-electron transistor", *Applied Physics Letters* **81** (2002), 2258-2260.

[5] A. Choe. "Researchers Race to Put the Quantum Into Mechanics", *Science* **299** (2003), 36-37.

[6] K. C. Schwab and M. L. Roukes. "Putting Mechanics into Quantum Mechanics", *Physics Today* (2005), 36-42.

[7] Kittel, C. and H. Kroemer, *Thermal Physics*. 2nd ed. New York: Freeman, 1980.

[8] V. B. Braginsky and F. Y. Khalili, edited by Kip S. Thorne, *Quantum Measurement*. Cambridge: Cambridge University Press, 1992.

[9] X. M. H. Huang, C.A. Zorman, M. Mehregany, and M.L. Roukes. "Nanodevice Motion at Microwave Frequencies", *Nature* **421** (2003), 496.

[10] W. Heisenberg. "Ueber den anschaulichen Inhalt der quantentheoretischen Kinematik und Mechanik", *Zeitschrift für Physik* **43** (1927), 172-198.

[11] J. J. Sakurai. *Modern Quantum Mechanics*. Revised ed. New York: Addison-Wesley, 1994.

[12] C. M. Caves. "Quantum Limit on Noise in Linear Amplifiers", *Physical Review D Particles and Fields* **26** (1982), 1817-1839.

[13] A. A. Clerk. "Quantum Limited Position Detection and Amplification: A linear response perspective", *Physical Review B* **70** (2005), 245306 1-9.

[14] A. A. Clerk and S. M. Girvin. "Shot Noise of a Tunnel Junction Displacement Detector", *Physical Review B* **70** (2004), 121303 1-4.

[15] A. A. Clerk. "A Quantum Noise Approach to Quantum NEMS", *CALTECH NEMS Summer School Lecture Notes* (2007, July).

[16] A. N. Cleland. *Foundations of Nanomechanics*. Berlin: Springer, 2003.

[17] S.C. Kou and X. S. Xie. "Generalized Langevin Equation with Fractional Gaussian Noise: Subdiffusion within a Single Protein Molecule", *Physical Review Letters* **93** (2004), 180603 1-4.

[18] B. Skalar. *Digital communications : fundamentals and applications*. 2nd ed. N. J.: Prentice Hall, 2001.

[19] R. Kubo. "The fluctuation-dissipation Theorem", *Reports on Progress in Physics* **29** (1966), 255-284.

[20] A. O. Caldeira and A. J. Leggett. "Influence of Dissipation on Quantum Tunneling in Macroscopic Systems", *Physical Review Letters* **46** (1981), 211-214.

[21] R. J. Schoelkopf, A. A. Clerk, S. M. Girvin, K. W. Lehnert, and M. H. Devoret. *Quantum Noise in Mesoscopic Physics* chapter *Qubits as Spectrometers of Quantum Noise*. Kluwer, 2003.

[22] L. V. Hove. "Correlations in Space and Time and Born Approximation Scattering in Systems of Interacting Particles", *Physical Review Letters* **95**, (1954), 249 − 262.

[23] D. Mozyrsky and I. Martin. "Quantum-Classical Transition Induced by Electrical Measurement", *Physical Review Letters* **89** (2002), 018301 1-4.

[24] A.D. Armour, M.P. Blencowe, and Y. Zhang. "Classical dynamics of a nano-mechanical resonator coupled to a single-electron transistor", *Physical Review B* 69 (2004), 125313 1-15.

[25] D. Mozyrsky, I. Martin, and M. B. Hastings. "Quantum-Limited Sensitivity of Single-Electron-Transistor-Based Displacement Detectors", *Physical Review Letters* **92** (2004), 018303 1-4.

[26] P. B. Allen. "Linear Response Theory and Kubo Formulas", *Troisieme Cycle de Physique en Suisse Romande, Transport in Solids, Lausanne* **1965**.

[27] J. I. Busch-Vishniac. *Electromechanical Sensors and Actuators*. 1st ed., Berlin: Springer, 1998.

[28] K. L. Ekinci. "Electromechanical Transducers at the Nanoscale: Actuation and Sensing of Motion in Nanoelectromechanical Systems (NEMS)", *Small* **1** (2005), 786-797.

[29] S. M. Carr and M. N. Wybourne. "Elastic instability of nanomechanical beams", *Applied Physics Letters* **82** (2003), 709-711.

[30] M. Roukes. "NEMS: nanoelectromechanical systems", *CALTECH NEMS Summer School Lecture Notes* (2007, July).

[31] L.D. Landau and E.M. Lifshitz. *Theory of Elasticity*. 3rd English ed., New York: Butterworth-Heinemann, 1986.

[32] Material Property Data Matweb. Available online: http://www.matweb.com/

[33] R. G. Jackson. *Novel sensors and sensing*. Bristol : Institute of Physics Publishing, 2004.

[34] K.L. Ekinci and M. L. Roukes. "Nanoelectromechanical systems", *Review of Scientific Instruments* **76** (2005), 061101 1-12.

[35] L. Sekaric, J. M. Parpia, H. G. Craighead, T. Feygelson, B. H. Houston and J. E. Butler. "Nanomechanical resonant structures in nanocrystalline diamond", *Applied Physics Letter* **81** (2002), 4455-4457.

[36] L. L. Chu, Y. B. Gianchandani, and L. Que. "Measurements of Material Properties Using Differential Capacitive Strain Sensors", *Journal of Microelectromechanical Systems* 11 (202), 489 –498.

[37] S. Akamine, T. R. Albrecht, J. M. Zdeblick, and C. F. Quate. "A Planar Process for Microfabrication of a Scanning Tunneling Microscope", *Sensors and Actuators A* **23** (1990), 964-970.

[38] R. Schoelkopf. "Amplifying quantum signal with the signal-electron transistor", *Nature* **406** (2000), 1039-1046.

[39] M.P. Blencowe. "Nanoelectromechanical Systems", *Contemporary Physics* **46** (2005), 249-264.

[40] R. G. Knobel and A. N. Cleland. "Nanometer-scale displacement sensing using a single electron transistor", *Nature* **424** (2003), 291-293.

[41] R. J. Schoelkopf, P. Wahlgren, A. A. Kozhevnikov, P. Delsing,and D. E. Prober. "The Radio-Frequency Single-Electron Transistor (RF-SET): A Fast and Ultrasensitive Electrometer", *Science* **280** (1998), 1238-1242.

[42] M. D. LaHaye, O. Buu, B. Camarota, and K. C. Schwab. "Approaching the Quantum Limit of a Nanomechanical Resonator", *Science* **304** (2004), 74-77.

[43] J.S. Aldridge, R. Knobel, D.R. Schmidt, C.S. Yung, and A.N. Cleland. "Nanoelectronic and nanomechanical systems", *SPIE Proceedings* **11** (2001).

[44] T. Kouh, D. Karabacak, D. H. Kim, and K. L. Ekinci. "Diffraction effects in optical interferometric displacement detection in nanoelectromechanical systems", *Applied Physics Letters* **86** (2005), 013106 1-3.

[45] C. Meyer, O. Sqalli, H. Lorenz, and K. Karrai. "Freely suspended nanostructure with no substrate beneath: fabrication and optical imaging", *, 4th Nanotechnology IEEE Conference* (2004), 435-437.

[46] D. Karabacak, T. Kouh, and K. L. Ekinci. "Analysis of optical interferometric displacement detection in nanoelectromechanical systems", *Journal of Applied Physics* **98** (2005), 124309 1-9.

[47] K. L. Ekinci. "Nanomechanical Displacement Transduction and the RF-STM", *CALTECH NEMS Summer School Lecture Notes* (2007, July).

[48] D. Karabacak, T. Kouh, C. C. Huang, and K. L. Ekinci. "Optical knife-edge technique for nanomechanical displacement detection", *Applied Physics Letters* **88** (2006), 193122 1-3.

[49] D. M. Karabacak, K. L. Ekinci, C. How Gan, G. J. Gbur, M. S. Unlu, S. B. Ippolito, B. B. Goldberg, and P. S. Carney. "Diffraction of evanescent waves and nanomechanical displacement detection", *Optics Letters* **32** (2007), 1881-1883.

[50] R. Eisberg and R. Resnick. *Quantum Physics of Atoms, Molecules, Solids, Nuclei, and Particles.* 2nd ed., New York : Wiley, 1985.

[51] J. G. Simmons. "Generalized Formula for the Electric Tunnel Effect between Similar Electrodes Separated by a Thin Insulating Film", *Journal of Applied Physics* **34** (1963), 1793-1803.

[52] P. A. Anderson. "Work Function of Gold", *Physical Review* **115** (1959), 553-554.

[53] G. Binnig and H. Rohrer. "Scanning Tunneling Microscopy", *Surface Science* **152** (1985), 17-26.

[54] M. Niksch and G. Binnig. "Proposal for a novel gravitational-wave sensor", *Journal of Vacuum Science and Technology A* **6** (1987), 470-471.

[55] M. F. Bocko, K. A. Stephenson, and R. H. Koch. "Vacuum Tunneling Probe: A Nonreciprocal, Reduced-Back-Action Transducer", *Physical Review Letters* **61** (1988), 726-729.

[56] K. A. Stephenson, M. F. Bocko, and R. H. Koch. "Reduced-noise nonreciprocal transducer based upon vacuum tunneling", *Physical Review A* **40** (1989), 6615-6625.

[57] B. Yurke and G. P. Kochanski. "Momentum noise in vacuum tunneling transducers", *Physical Review B* **41** (1990), 8184-8194.

[58] M. F. Bocko. "The scanning tunneling microscope as a high-gain, low-noise displacement sensor", *Review of Scientific Instruments* **61** (1990), 3763-3768.

[59] F. Bordoni, M. Karim, M. F. Bocko, and T. Mengxi. "Proposed room-temperature detector for gravitational radiation from galactic sources", *Physical Review D* **42** (1990), 2952-2955.

[60] M. F. Bocko and R. Onofrio. "On the measurement of a weak classical force coupled to a harmonic oscillator: experimental progress", *Reviews of Modern Physics* **68** (1996), 755-799.

[61] C. Presilla, R. Onofrio, and M. F. Bocko. "Uncertainty-principle noise in vacuum-tunneling transducers", *Physical Review B* **45** (1992), 3735-3743.

[62] G. E. Uhlenbeck and L. S. Ornstein. "On the Theory of the Brownian Motion", *Physical Review* **36** (1930), 823-841.

[63] P. J. M. van Bentum, H. van Kempen, L. E. C. van de Leemput, and P. A. A. Teunissen. "Single-Electron Tunneling Observed with Point-Contact Tunnel Junctions", *Physical Review Letters* **60** (1988), 369 – 372.

[64] G. Jr. Nunes, and M. R. Freeman. "Picosecond Resolution in Scanning Tunneling Microscopy", *Science* **262** (1993), 1029-1032.

[65] N. E. Flowers-Jacobs, D. R. Schmidt, and K.W. Lehnert. "Intrinsic Noise Properties of Atomic Point Contact Displacement Detectors", *Physical Review Letters* **98** (2007), 096804 1-4.

[66] D. J. Reilly, C. M. Marcus, M. P. Hanson and A. C. Gossard. "Fast single-charge sensing with a rf quantum point contact", *Applied Physics Letters* **91** (2007), 162101 1-3.

[67] L. J. Swenson, D. R. Schmidt, J. S. Aldridge, D. K. Wood, and A. N. Cleland. "Mixing with the radio frequency single-electron transistor", *Applied Physics Letters* **83** (2005), 173112 1-3.

[68] T. M. Buehler, D. J. Reilly, R. P. Starrett, N. A. Court, A. R. Hamilton, A. S. Dzurak, and R. G. Clark. "Development and operation of the twin radio frequency single electron transistor for cross-correlated charge detection", *Journal of Applied Physics* **96** (2004), 4508-4513.

[69] U. Kemiktarak, T. Ndukum, K. C. Schwab, and K. L. Ekinci. "Radio-frequency scanning tunnelling microscopy", Nature 450 (2007), 85-89.

[70] H. Park, J. Park, A. K. L. Lim, E. H. Anderson, A. P. Alivisatos, and P. L. McEuen. "Nanomechanical oscillations in a single-C60 transistor", *Nature* **407** (2000), 57-60.

[71] L. H. Yu1, Z. K. Keane, J. W. Ciszek, L. Cheng, M. P. Stewart, J. M. Tour, and D. Natelson. "Inelastic Electron Tunneling via Molecular Vibrations in Single-Molecule Transistors", *Physical Review Letters* **93** (2004), 266802 1-4.

[72] M.A. Reed, C. Zhou, C.J. Muller, T.P. Burgin, and J.M. Tour, "Conductance of a molecular junction," *Science* **278** (1997), 252-254.

[73] C. Z. Li, A. Bogozi, W. Huang, and N. J. Tao. "Fabrication of stable metallic nanowires with quantized conductance", *Nanotechnology* **10** (1999), 221–223.

[74] J. M. van Ruitenbeek, A. Alvarez, I. Pineyro, C. Grahmann, P. Joyez, M. H. Devoret, D. Esteve, and C. Urbina. "Adjustable nanofabricated atomic size contacts", *Review of Scientific Instruments* **67** (1996), 108-111.

[75] C. J. Muller, J. M. Krans, T. N. Todorov, and M. A. Reed. "Quantization effects in the conductance of metallic contacts at room temperature", *Physical Review B* **53** (1996), 1022-1025.

[76] N. J. Tao. "Electron transport in molecular junctions", *Nature Nanotechnology* **1** (2006), 173-181.

[77] J. J. Parks, A. R. Champagne, G. R. Hutchison, S. Flores-Torres, H. D. Abruña, and D. C. Ralph. "Tuning the Kondo Effect with a Mechanically Controllable Break Junction", Physical Review Letters **99** (2007), 026601 1-4.

[78] H. B. Heersche, G. Lientschnig, K. O'Neill, H. S. J. van der Zant, and H. W. Zandbergen. "In situ imaging of electromigration-induced nanogap formation by transmission electron microscopy", *Applied Physics Letters* **91** (2007), 072107 1-3.

[79] Z. M. Wu, M. Steinacher, R. Huber, M. Calame, S. J. van der Molen, and C. Schönenberger. "Feedback controlled electromigration in four-terminal nanojunctions", *Applied Physics Letters* **91** (2007), 053118 1-3.

[80] D. R. Strachan, D. E. Smith, D. E. Johnston, T.-H. Park, M. J. Therien, D. A. Bonnell, and A. T. Johnson. "Controlled fabrication of nanogaps in ambient environment for molecular electronics", *Applied Physics Letters* **86** (2005), 043109 1-3.

[81] G. Esen and M. S. Fuhrer. "Temperature control of electromigration to form gold nanogap junctions", *Applied Physics Letters* **87** (2005), 263101 1-3.